UiT

THE ARCTIC UNIVERSITY OF NORWAY

FACULTY OF SCIENCE AND TECHNOLOGY

A shallow gas flat spot anomaly in the Bjørnøyrenna Fault Complex in the Barents Sea: processing and interpretation of P-Cable 3D seismic data

—

Adrian Lium-Wickler

Master thesis in GEO-3900

May 2015

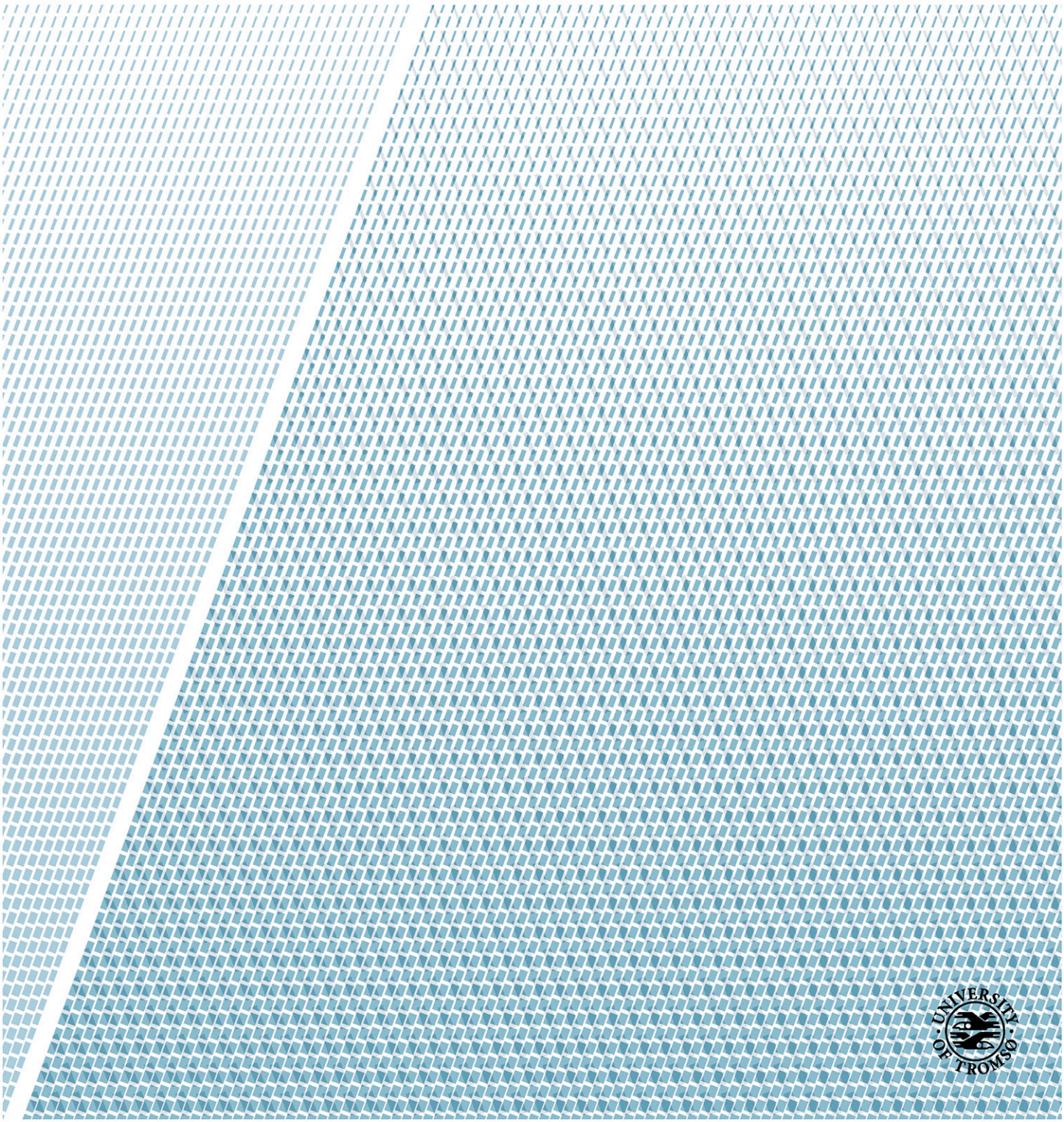

Abstract

This thesis analyzed P-Cable high-resolution 3D seismic data from the Bear Island Fault Complex in the southwestern Barents Sea acquired during a Helmer Hanssen cruise in 2012. Hence, the thesis is divided into two parts: the first part of the thesis focuses on the steps taken during the processing of the raw seismic data from the Lundin 2012 Area-A survey located at the Bear Island Trough Fault Complex. The processing includes assigning geometry to the seismic data, correcting the source-receiver offset, and then assembling a cube from the seismic lines through CDP Binning. After creating the 3D cube, the signal to noise ratio is improved through filtering procedures. For this project, the Ormsby filtering was used to remove noise from the seismic signal. Ghost signals were removed trough a DeGhosting process. Import of tidal data was done to attenuate some of the noise created by variations in water depth. Normal move out and stacking was done before migrating the data. After migration, the data was exported to Petrel for the interpretations.

The second part of the thesis focuses on the interpretation of the processed 3D seismic data with emphasis on hydrocarbon indicators, shallow gas accumulations, and potential migration pathways. The stratigraphy of the area was correlated through well 7219/9-1. This was done by tracing stratigraphical boundaries across several 2D lines before connecting with the dataset. Within the dataset, I observe the Top Hekkingen Formation up to the Torsk Formation. The top of the Torsk Formation is cut by the Upper Regional Unconformity (URU), which is overlain by glacigenic sediments. Large-scale normal faults interpreted as half-gradens, with small-scale faults within the blocks, are seen in the eastern part of the dataset. On the seabed, we see features such as iceberg ploughmarks and pockmarks. Pockmarks mainly occur within the ploughmarks and are located above flat spots seen at the URU in seismic cross section. Most of the gas accumulations are observed at the URU with the overlaying Neogene sediments acting as a seal for further gas migration. A flat spot was also observed within the Jurassic sediments. Evidence of fluid migration through faults and permeable layers are seen as areas with acoustic masking. The vertical fluid migration seems to terminate at the observed gas accumulations at the URU. A few examples of gas migration to the seabed are observed through pipes with associated pockmarks. This might be due to overpressure created beneath the URU seal.

Acknowledgements

Firstly, I would like to thank my advisor Stefan Büenz for giving me such an interesting project, and his assistance along the way, especially at the end. A big thanks to my co-advisor Andreia Plaza Faverola for teaching me how to process seismic data, a much more difficult and interesting process then I had expected. An additional thanks to Sandra Hurter for taking the time to help me solve processing problems along the way.

The last few years have been the toughest, but also the most rewarding in my life. I would like to thank all the people in both Tromsø and the USA who have made these years so special for me. Thanks to Anders Edvardsen, Andrè Jensen, and Espen Bergø for all the help, motivation, and coffee throughout the last year, I wouldn't have changed my office, even if I could.

A special thanks to my family who always support me and were never more than a phone call away. My dad for proof reading my paper, my mom for her constant support, and my brothers for distracting me from just working. A special thanks to Stine for her love and support, and all the food, it wouldn't have been the same without you.

Thanks to my friends for all the fun times, lunches, and discussions both scientific and otherwise. Thanks to Renate Bredesen for her understanding, and flexible scheduling, during the last year.

And to anyone I may have forgotten, thanks, now it's on to the next big thing!

Adrian Lium-Wickler

Tromsø, May 2015

Table of Contents

1 Introduction

The goals of this master thesis are two-fold. The first is to process and migrate 3D seismic data. The data used for the thesis is P-Cable 3D seismic data acquired in the Bear Island Trough Fault Complex with R/V Helmer Hanssen during a survey in 2012. After the processing is completed, the thesis will move on to the second section, which includes interpretation and analysis of the 3D seismic data. The main goal here is to better understand the controlling mechanisms for the occurrence and development of shallow gas accumulations. By interpreting a classic flat spot anomaly and other hydrocarbon indicators such as pockmarks, acoustic masking, and bright spots, and their relationship to the structural development in the area, the controlling mechanisms may be better understood.

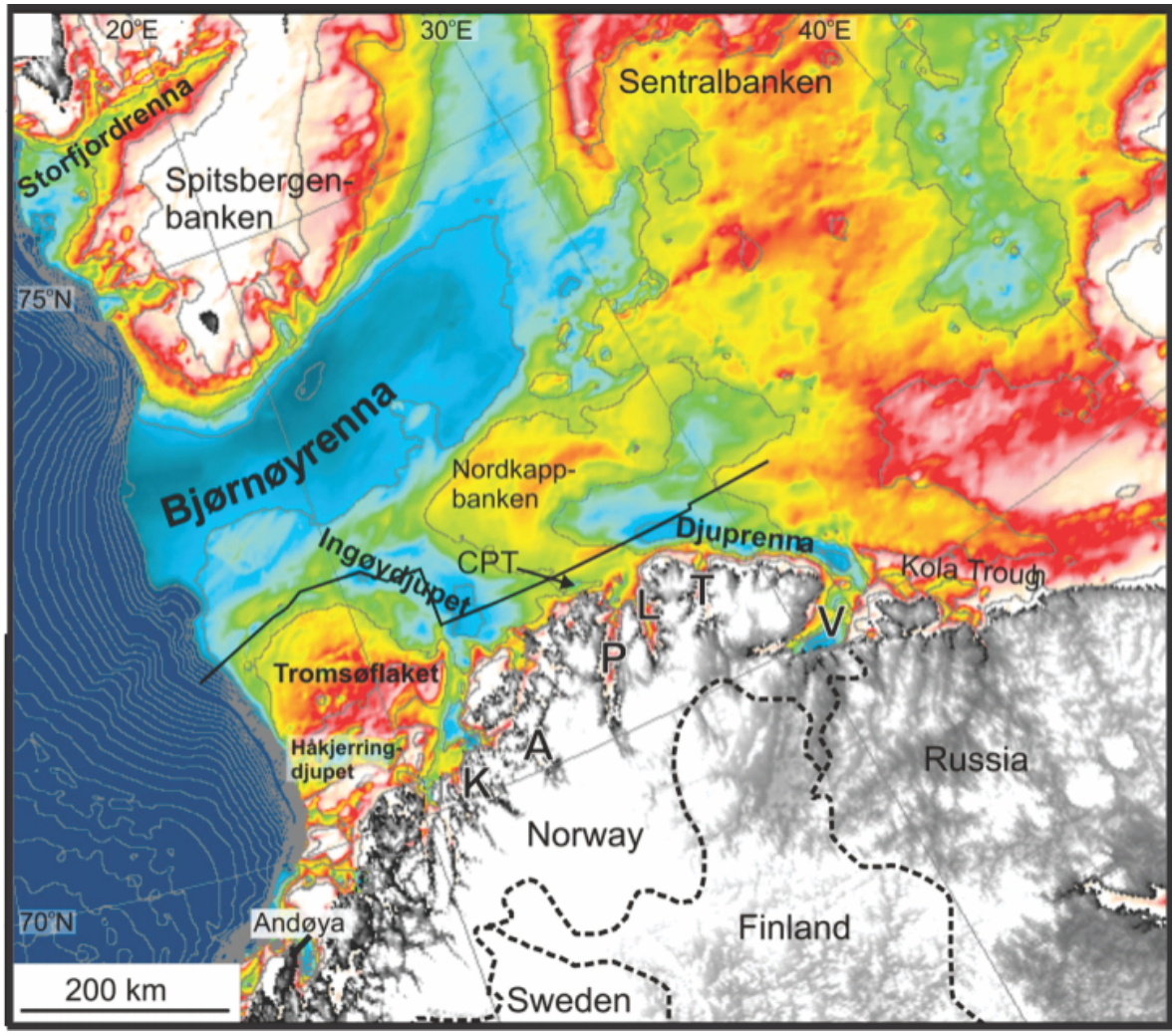

Figure 1.Bathymetry map of the southwestern Barents Sea. From Windsborrow, 2009.

1.1 Geology

The Barents Sea (Figure 1) is located off the northern coast of Norway and Russia and extends up to the Arctic Ocean, covering one of the widest continental shelves in the world. It extends from the Greenland Sea in the West to Novaya Zemlya in the East covering a total area of 1.3 million km^2 (Dore, 1995).

Geophysical investigations began in the 1970s with drilling for hydrocarbons starting in the early 1980s with several commercial finds since (Dore, 1995). The Barents Sea consists of basin areas divided by fault complexes and highs, a result of both continental collision and separation during its creation (Figure 2). The first major collision event occurred approximately 400 Ma (Dore, 1995) when the Laurentian plate and Baltic plate collided during the closure of the Iapetus Ocean.

During the Late Paleozoic and Mesozoic, extensional movement dominated the Barents Sea. These events led to the major rift basins and structural highs across the Barents Sea. During the Late Paleozoic and Mesozoic and continuing up until the present day marine sedimentation has been the dominant deposition, however the marine deposition has been affected by climate change as the Barents Sea area has drifted northwards. This led to carbonate deposition during Devonian, Carboniferous and Permian times, and clastic deposition from the Triassic onwards (Dore, 1995).

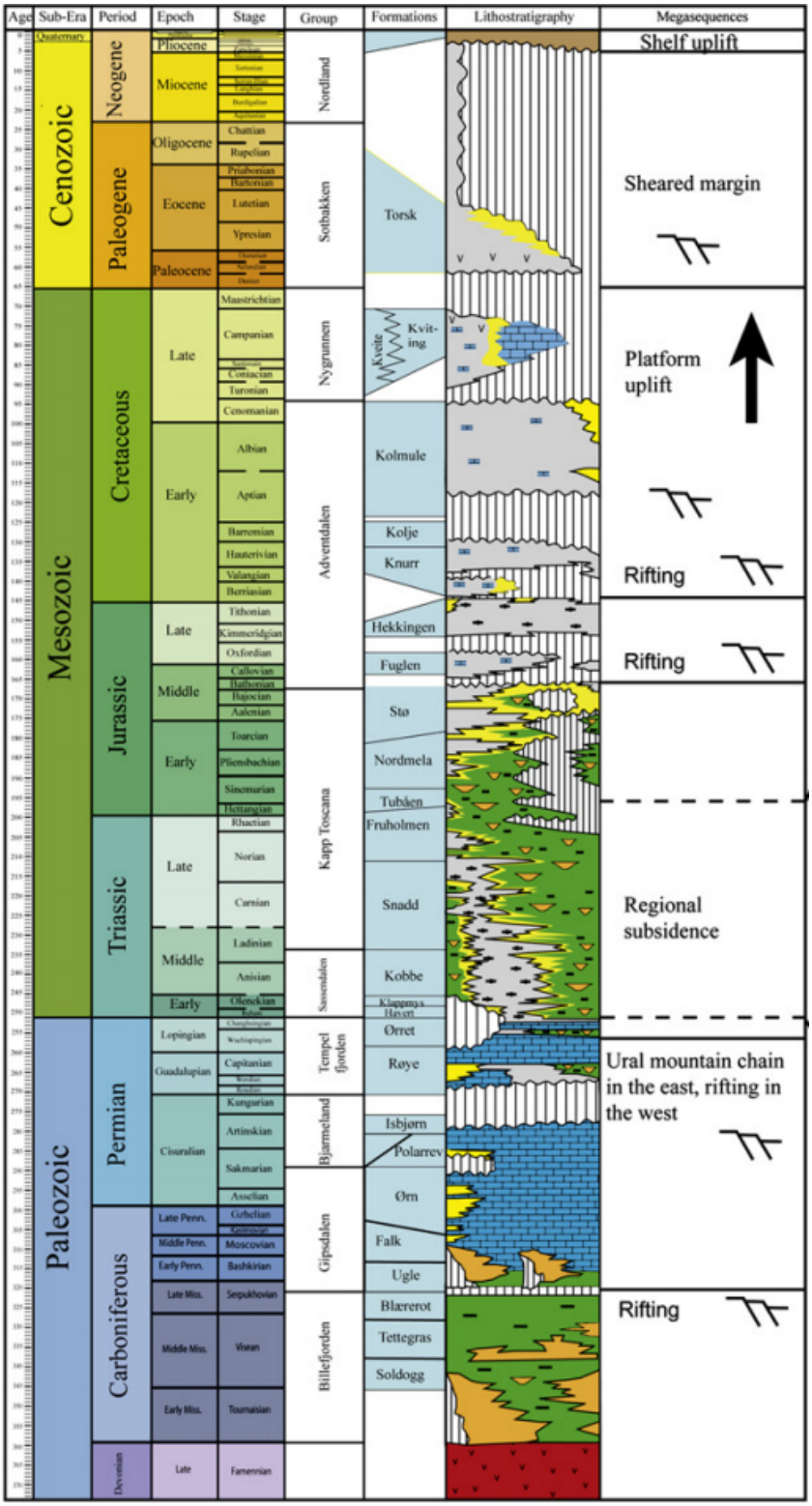

Figure 2. Stratigraphic column of the Western Barents Sea. Modified from Glørstad-Clark, 2010.

The Barents Sea floor is cut by series of troughs. The largest one being the Bear Island Trough (Bjørnøyrenna) to the North of where the survey area is located. The trough extends 750 km from Sentralbanken in the East to the shelf edge in the West (Winsborrow, 2009;

Vorren et al. 1998). The water depth in the trough range between 300 to 500 meters (Andreassen, 2009). Even though several surveys in search of commercially lucrative hydrocarbon reserves have been completed, this has yet to be found. This is believed to be due to erosion of up to 500-2000 meters of rock and sediments during the Cenozoic uplift (Dore, 1996). The uplift resulted in expansion of gas, tilting of potential reservoirs, and leakage of hydrocarbons. The Bear Island Trough mouth fan contains up to 3-4 kilometers of Plio-Pleistocene sediments. These sediments were delivered by major ice streams through the Bear Island Trough during the last glacial maximum (Andreassen et al. 2008).

The NE-SW trending Bear Island Trough fault complex, seen in this survey, defines the transitional zone between the Loppa High Platform to the southeast and the Cretaceous basin to the northwest (Gabrielsen, 1997).

The Cenozoic is characterized by uplift and erosion on the Barents shelf. This is important because uplift degrades the hydrocarbon productivity by narrowing the prospecting depth window (Reemst, 1994).

The most significant seismic reflector on the continental shelf is the Upper Regional Unconformity (URU), which separates the underlying bedrock and the overlying glacial deposits (Adreassen et al, 2008). Above the URU we find a glacigenic sequence of varying thickness which has been documented by several core and drill samples (Andreassen et al, 2008). This represents the erosional base of several continental shelf glaciations, the sediments then being deposited at the trough mouth fans beyond the shelf edge.

1.1.1 Source rock

A source rock is a sedimentary unit capable of generating hydrocarbons that migrate into a reservoir. To achieve a high enough percentage of organic matter (kerogen) preserved within the sediment, the depositional environment must be such that it inhibits oxidation. As time passes the burial depth increases, which in turn increases the temperature and pressure leading to the formation of kerogen (Dore, 1995; Selley, 2008). Oil is formed first, at lower temperatures, followed by the formation of gas at a higher temperature and greater burial depth (Figure 3).

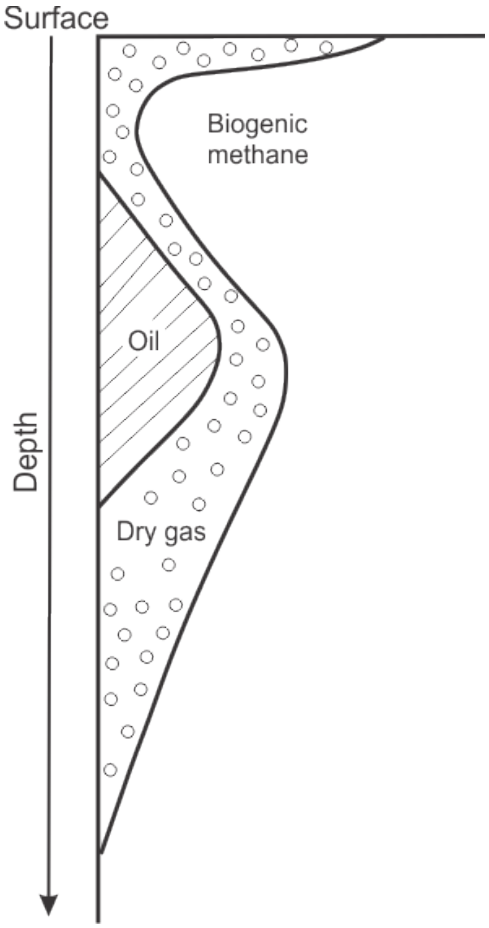

Figure 3. Correlation between hydrocarbon generation, and depth/temperature. Modified from Selley, 2008.

Several potential source horizons are present in the Barents Sea, though the Late Jurassic horizon, which consists of dark, organic rich shale, is considered to have the best quality. This formation is known as the Hekkingen Formation within the Barents Sea (Dore, 1995). Despite being widespread in the southern Barents Sea, the Hekkingen Formation shale has not reached its full generation potential because of its lack of maturity. The formation is regionally present but may be eroded on structural highs, although it is believed to be oil to gas mature in the Hammerfest basin and on the eastern rim of the Bear Island Trough Fault Complex (Thiessen, 2013). Further west it is too deeply buried, and further east it is too shallow (Dore, 1995). No oil shows have been found in the Bear Island Trough, indicating the source may have passed the oil mature window and become gas mature.

Figure 4 shows an overview map of the potential source rocks within the Barents Sea (Ohm et al, 2008). The Upper Jurassic Hekkingen Formation shale represents the best source rock for the dataset, followed by the Triassic formations.

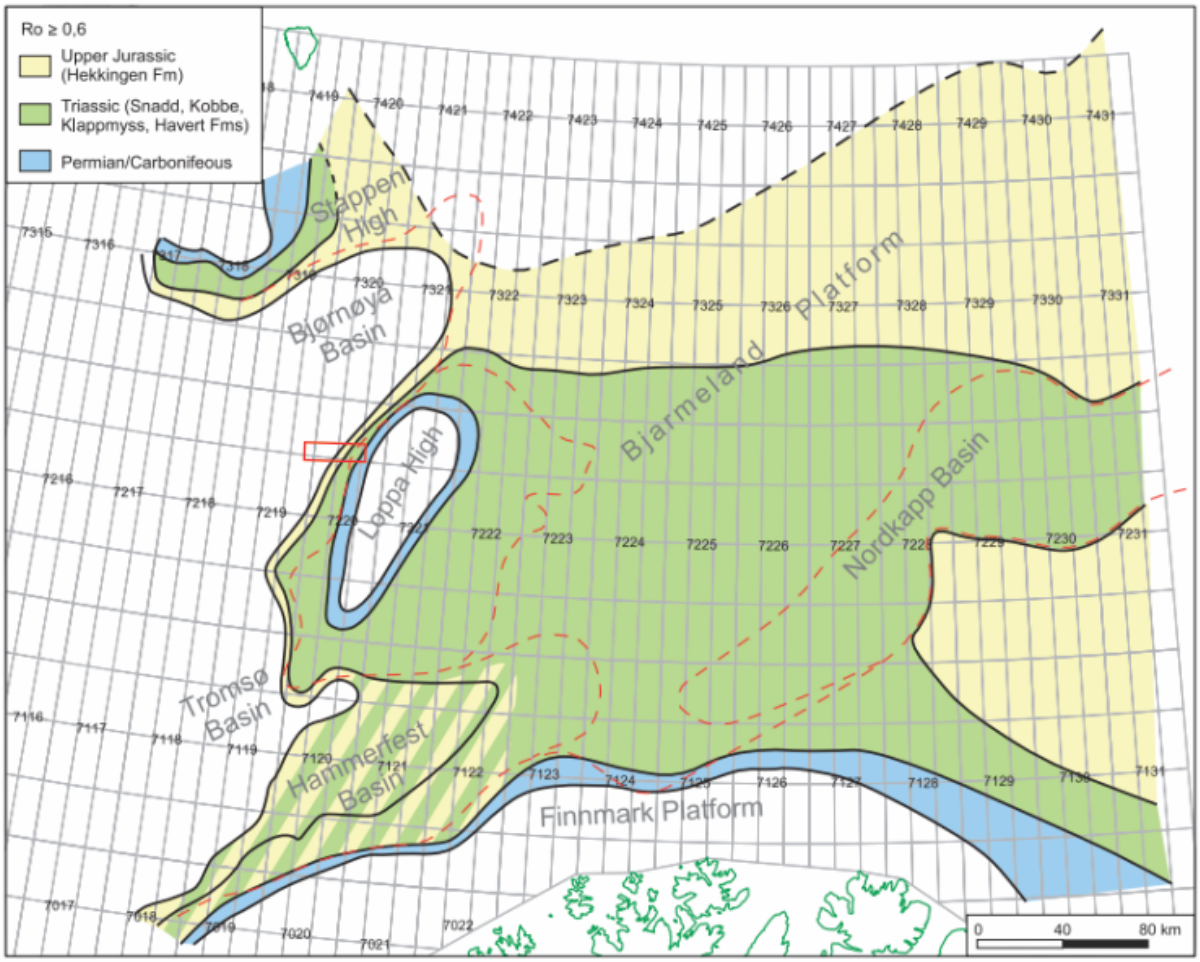

Figure 4. Tentative maturity map suggesting where Permian, Triassic, and Jurassic strata are oil mature, given that such are present in source quality. Red square shows rough location of the area that contains the dataset. Modified from Ohm et al, 2008.

1.1.2 Sonic velocity

The seismic velocity is important because it may aid in recognizing different lithologies, facies and fluids. For this thesis, the velocity-depth trends by Storvoll et al. (2005) are used. These velocity-depth trends are based on the data from 13 wells located within the Barents Sea (Figure 5). Figure 6 shows the sonic velocity measurements from the wells at their present depth and the estimated trend line based on published data.

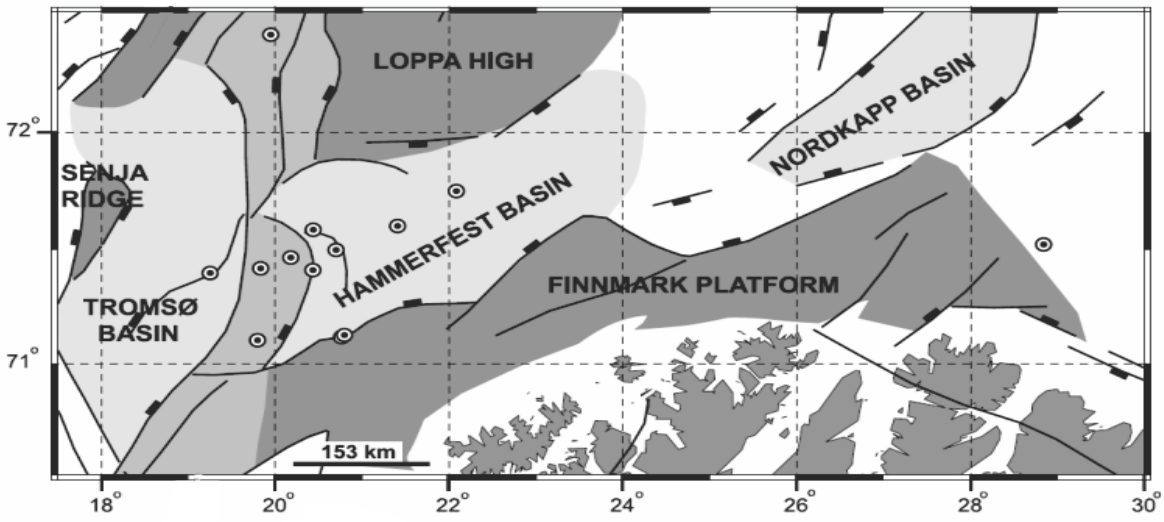

Figure 5. Locations of wells (dotted circles) used for the sonic velocity measurements in Figure 5. Modified from Storvoll et al. 2005.

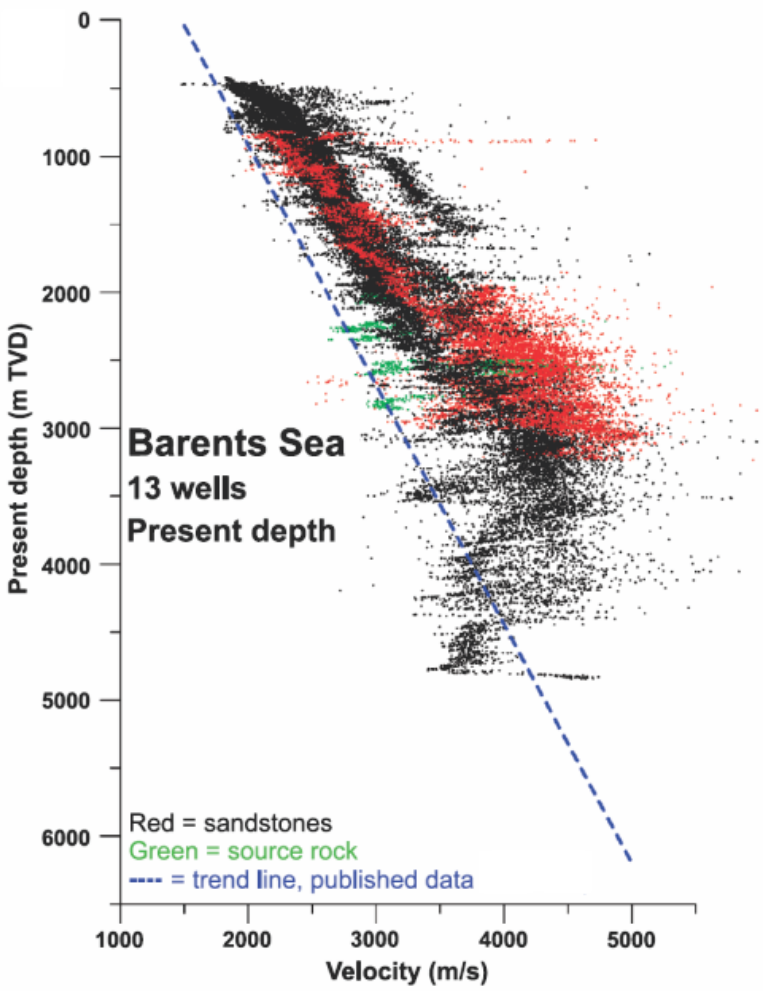

Figure 6. Sonic velocity measurements at present depth (every 0.5 – 0.7 m with depth) from 13 wells in the Barents Sea area (Figure 5). Sands are shown as red, shale in black and the Hekkingen formation, which is organic rich, in green. The estimated trend line based on the published data. Modified from Storvoll et al. 2005.

1.2 Fluid migration indicators

Pore spaces between sediments contain fluids, usually water, but also hydrocarbons. Hydrocarbons migrate into the reservoir rock at depth and some time after burial. Several observations point to this fact, such as oil and gas collecting at the highest point of permeable rocks. This implies upward and lateral migration of the hydrocarbons. Oil and gas are often found in pores and fractures that must have been created after lithification of the rock. This indicates migration after the burial and fracturing of the reservoir rock (Selley, 1998). The effect of pressure and temperature is important for the migration of the hydrocarbons, but eventually they all tend to migrate up since their density is lower than the

surrounding rock (Guzzetta, 1987). Hydrocarbons are transported as a separate phase that is primarily driven by their buoyancy relative to water (Bjørlykke, 2010).

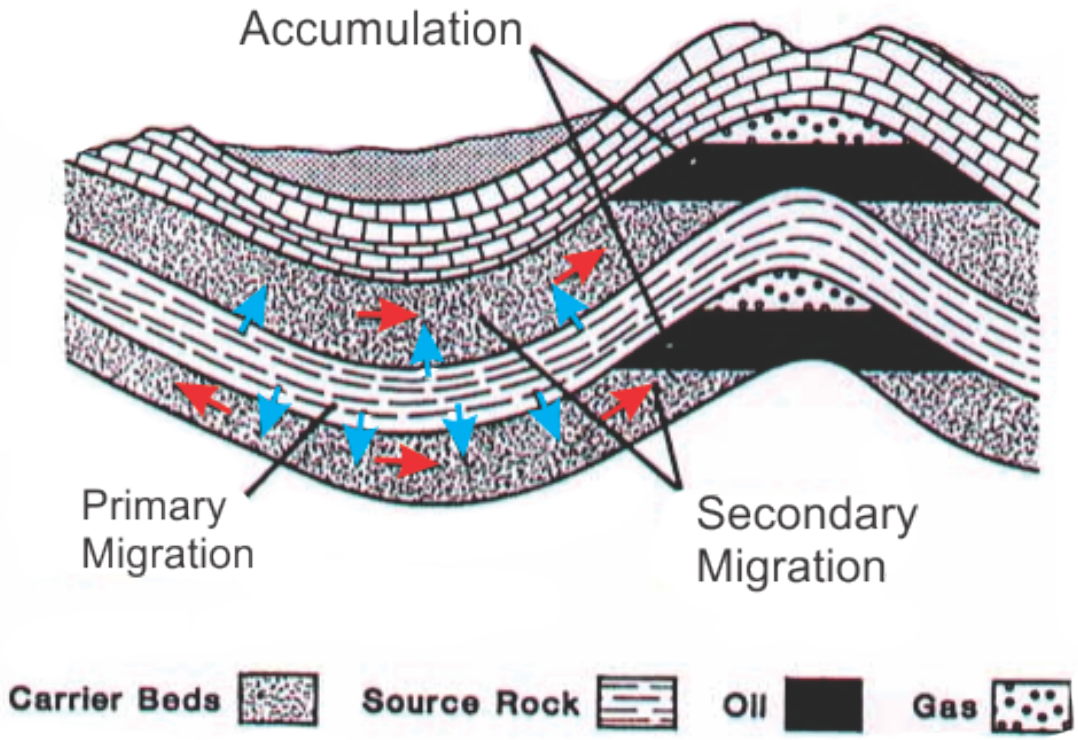

Figure 7. Figure illustrating the migration of hydrocarbons. Primary migration from source rock into a carrier bed followed by secondary migration within the permeable unit. The figure also illustrates a typical structural trap where hydrocarbons are trapped below a less permeable unit. Modified from Tissot and Welt (1984).

There are two main types of hydrocarbon migration, which are shown in Figure 7. Primary migration is hydrocarbons leaving the source rock (clay or shale) into a more permeable layer. When kerogen matures much of its solid matter is broken down, and transformed into fluid oil and gas. This process increases the volume of the fluids in the pore spaces compared to the original solid phase volume (Bjørlykke, 2010). Though the total volume expansion is not necessarily large, it will still lead to overpressure within the source rock since it is creating a change in void pressure compared to the solid kerogen. This contributes to the migration of hydrocarbons out of the source rock.

Secondary migration is the movement of the hydrocarbons from the source rock through a carrier bed into a reservoir (Selley, 1998). This migration is driven by buoyancy due to the

difference in density of the fluids. The hydrocarbons will continue to migrate upwards until they reach sediments whose pores are small enough to hold the pressure created by the hydrocarbon column. Secondary migration requires a continuous pathway with high petroleum saturation creating a series of micro-traps where the petroleum is trapped in small and large scale dead ends (Bjørlykke, 2010). Faults may also effect the migration of fluids, acting as both barriers and pathways for fluids. Other features such as salt diapirs or unconformities create cap rocks for hydrocarbons. If no seal exists, the hydrocarbons will migrate up into the ocean. Since gas, oil, and water have different densities, a stratification related to their density will occur within the reservoir rock, with gas above the oil/water.

1.2.1 Seismic indications of hydrocarbons

The presence of hydrocarbons can be seen in seismic data in a number of different ways. Reflections are a result of change in the acoustic impedance, which is the product of the wave velocity and the density of the layer, resulting in reflections for changes in sedimentation conditions, lithology changes and variations in pore content (Geokompendium, 2009; Veeken, 2007). Fluid contacts within sediment bodies especially gas-water contacts will create individual reflections. This is because the presence of gas in a seismic section will cause an amplitude change (Veeken, 2007). If the pore spaces of a sediment contain gas instead of water, it will cause a noticeable reduction in the velocity of the P-wave. Even small amounts of gas in the sediments will cause a reduction in the P-wave velocity. Oil shows are much less distinct in the seismic data, as the velocity of the P-wave through oil is almost identical to water.

The Bottom Simulating Reflector (BSR) corresponds to the base of the gas hydrate stability zone as a result of an acoustic impedance contrast between hydrate-bearing sediments and free gas in sediments below (Bünz and Mienert, 2004). The name Bottom Simulating Reflector refers to the phase reversals tendency to follow the seafloor, as it is a result of temperature and pressure, therefor cutting stratigraphic horizons. The lack of a BSR does not exclude the presence of hydrates because it primarily is caused by free gas reflections (Bünz and Mienert, 2004).

Changes in velocity and impedance can be seen in several different ways; common types include amplitude anomalies, flat spots, polarity reversals, velocity effects, bright spots, dim spots, and other effects (Geokompendium, 2009). The most relevant indicators for this thesis are explained further in the next sections.

1.2.2 Amplitude anomalies

Amplitude anomalies can be divided into two groups, high amplitudes termed bright spots, and low amplitudes termed dim spots. A bright spot will arise in unlithified and relatively high-porosity sediments causing a negative change in acoustic impedance (Andreassen et al., 2007). Since this is a negative change, it will show as phase-reversed compared to positive reflections, showing as a trough on a seismic wiggle display (Figure 8).

Dim spots are reflections with anomalously low amplitudes and arise for instance, where less porous sediments are overlain by shale. A dim spot is in essence the revere of a bright spot, where a positive reflector reverses polarity for a local area (Selley, 1998). The dim spot may indicate increased porosity by showing an acoustically slower section, which in turn is an important indicator for improved reservoir chances. An example of a dim spot in a seismic section can be seen in Figure 9.

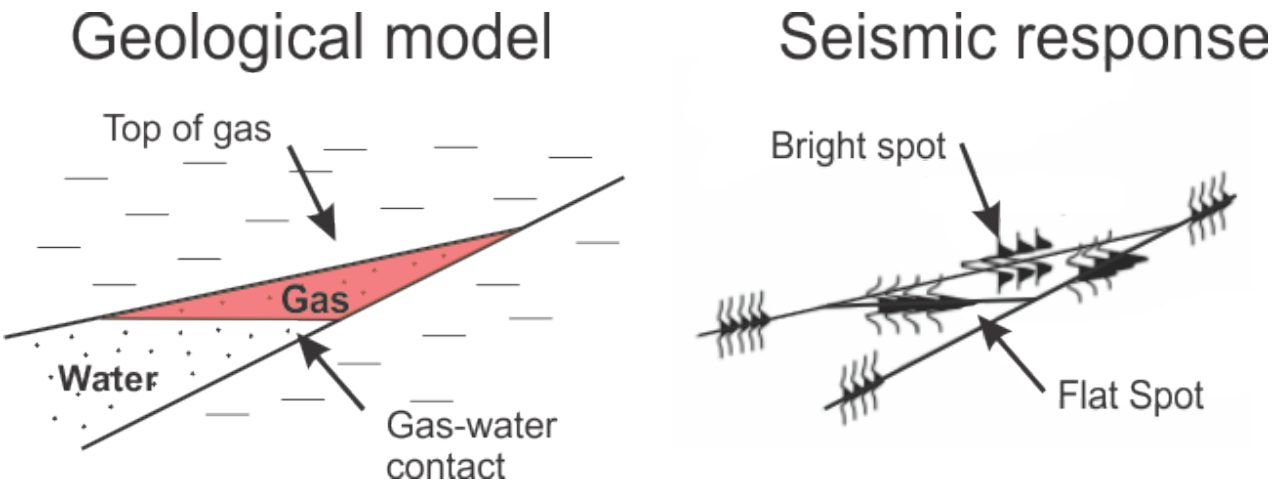

Figure 8. Figure illustrates a vertical section of a gas-bearing fan, showing both the geological model and the seismic response as a wiggle display. The figure highlights indications of bright spots and flat spots, and where they occur. Modified from Andreassen et al., 2007.

1.2.3 Flat spot

If the gas column is sufficiently thick, it will create an acoustic-impedance contrast at the boundary between gas and oil, or gas and water. This reflection is referred to as a flat spot, or a horizontal bright spot (Mussett, 2000). An example of a flat spot can be seen in Figure 8, and in a seismic section in Figure 9. Normally the result of acoustically slow gas-saturated sand above faster water-saturated sand creates the rapid increase in velocity needed to produce a flat spot (Selley, 1998). With the use of 3D seismic data, flat spots may be well imaged, even if the gas column is too thin to create a reflection on vertical seismic. A flat spot is a very good indicator for the gas/water contact because of the distinct flatness of the reflector and because it should be discordant with adjacent reflections, as we can see in Figure 9. Flat spots are found only down to about 2.5 kilometers because the velocity effect of gas is less noticeable below this depth and the contrast from the gas is reduced (Andreassen et al., 2007).

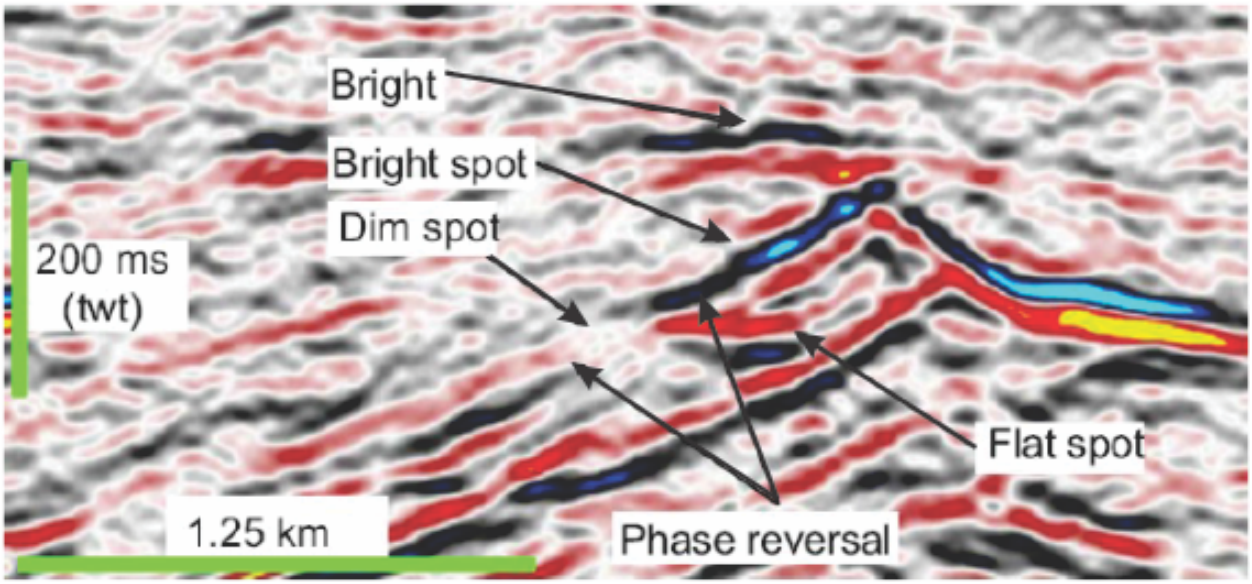

Figure 9. Image showing a seismic cross section containing examples of hydrocarbon indicators. Bright spots, dim spots and flats spots indicate hydrocarbons in the seismic section. Modified from Løseth et al. 2008.

1.2.4 Velocity effects

For thick gas columns, a pull-down effect may be observed on reflectors below the gas presence. This is usually observed below bright spots and flat spots. The effect makes reflectors appear further down then they actually are. The opposite effect can also be observed, where there is an increase in velocity, called pull-ups (Schlumberger, 2015).

1.2.5 Acoustic masking

Acoustic masking refers to low frequency shadows, areas that have distorted amplitudes and phases. These areas can be interpreted as gas chimneys, amplitude shadows or pipes. Gas chimneys are vertical zones of disturbance and may represent previous and present migration of gas through the sediments since the gas absorbs and scatters the acoustic energy (Heggland, 1998). Amplitude shadows are created when higher amplitudes cause a weakening of the deeper reflectors.

1.2.6 Pockmarks

Pockmarks are depressions on the seabed or paleo-seabed created by fluid flow. These depressions are often indications of hydrocarbon migration from underlying reservoirs, though other fluids may create them as well (Pau, 2014). Their size varies from 1 meter to hundreds of meters in width and up to 45 meters in depth.

2 Methods and material

In this chapter, the theory behind the collecting of seismic data, and an in depth look at how the P-cable seismic system used for collecting the data for this thesis works is presented.

2.1 2D and high resolution 3D seismic surveying

Seismic surveying is the most important method of geophysical prospecting. The seismic principle is based on artificial acoustic waves that create vibrations through the ground. If we consider a source of acoustic energy as a point, three types of waves emanate from this point. Surface waves move along the surface and are of limited use in seismic prospecting. The two other types of waves are known as body waves, P and S waves (Selley, 1998). In a marine environment, pulses of seismic energy are shot towards the seabed. Only body waves are used in marine exploration; P-waves (primary, pressure waves) and S-waves (secondary, shear waves) (Geokompendium, 2009). For this thesis, only the P-waves are considered, since S-waves do not travel through water, though they do occur in marine surveying when using receivers placed on the ocean floor. The seismic waves are used to create a picture of the subsurface structures and geological features. Two types of seismic surveying are common today, 2D and 3D. 2D seismic is a simpler and relatively inexpensive exploration method, while 3D seismic is a much more complex and accurate method. The 3D seismic method differs from the 2D method in a couple of important aspects. In general 3D seismic gives a much higher resolution. This is because the grid spacing (of inlines) is reduced from about a kilometer, which is typical for 2D seismic, to 25 m or less giving us a much higher horizontal resolution. The second advantage the 3D seismic has over 2D is the ability to collapse the Fresnel Zone (Chapter 2.1.2), and by doing so allowing complex geological structures to be imaged accurately (Geokompendium, 2009).

2.1.1 Reflection seismic

Seismic reflection techniques are essentially based on the same principles as echo or depth sounding, except the interest not only lies in the seafloor but also the layers below. Using artificial created sound waves, we can map geological structures by observing the arrival time of the reflected waves (Geokompendium, 2009).

Reflections are created by objects or interfaces that have a sufficient density-velocity contrast. These contrasts are the acoustic impedance contrast (Z) of a reflector,

$$Z = \text{Density} \times \text{Velocity}$$

The seismic reflectors are usually created by bedding planes, unconformities or artifacts.

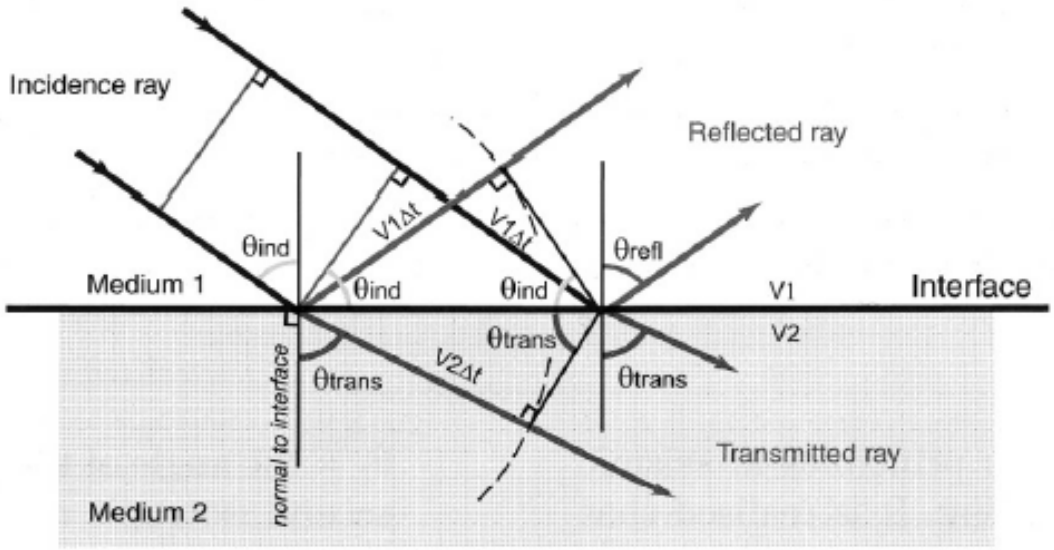

Figure 10. Figure showing how the seismic wave is reflected back into the first layer, and transmitted into the second layer following Snell's Law. From Geokompendium 2009; Veeken, 2007.

The energy reflected back into the first layer and the energy transmitted on to the second layer following Snell's law (Figure 10). Snell's law shows that a reflection is created at the critical angle of incidence (Geokompendium, 2009):

$$\frac{\sin\theta_{inc}}{V_1} = \frac{\sin\theta_{trans}}{V_2} = \frac{\sin\theta_{refl}}{V_1}$$

The ideal output of a seismic survey would be an acoustic impedance contrast indicating the changes between the geological boundaries, but since this is not achievable, the recorded seismic data can be seen as a superposition of the earth's reflectivity sequence.

2.1.2 Seismic resolution

The resolution of the seismic is important because it allows for more detailed mapping of features and potential prospects. The resolution is measured vertically and horizontally. The vertical resolution is a measure of how large an object has to be in order to be seen on the seismic section. The vertical resolution is calculated by λ/4, where λ is the wavelength, which means a layer will be seen if its thickness is more than ¼ of the wavelength (Rafaelsen, 2014). The wavelength is a function of the frequency (f) and the velocity (v):

$$\lambda = \frac{v}{f}$$

The resolution will also be poorer with increasing depth due to a decrease in the frequency as the velocity and wavelength increases. The velocity increases since the rocks are more compacted with depth.

The sound wave admitted from the source moves in three dimensions spreading over a larger area the further away from the source it travels. The horizontal resolution is calculated from the Fresnel zone (Figure 11), which is the part of a reflector, which the seismic signal covers at a certain depth. On an unmigrated seismic section the horizontal resolution is determined by the size of the Fresnel zone which is given by the equation (Geokompendium, 2009):

$$rf = \frac{V}{2}\left(\frac{t}{f}\right)^{\frac{1}{2}}$$

Where, rf = radius of the Fresnel zone, V = average velocity, t = two-way travel time in seconds, f = dominant frequency in hertz.

From the equation, we see how the Fresnel zone radius increases (horizontal resolution decreases) with depth, increased velocity, and lower frequency.

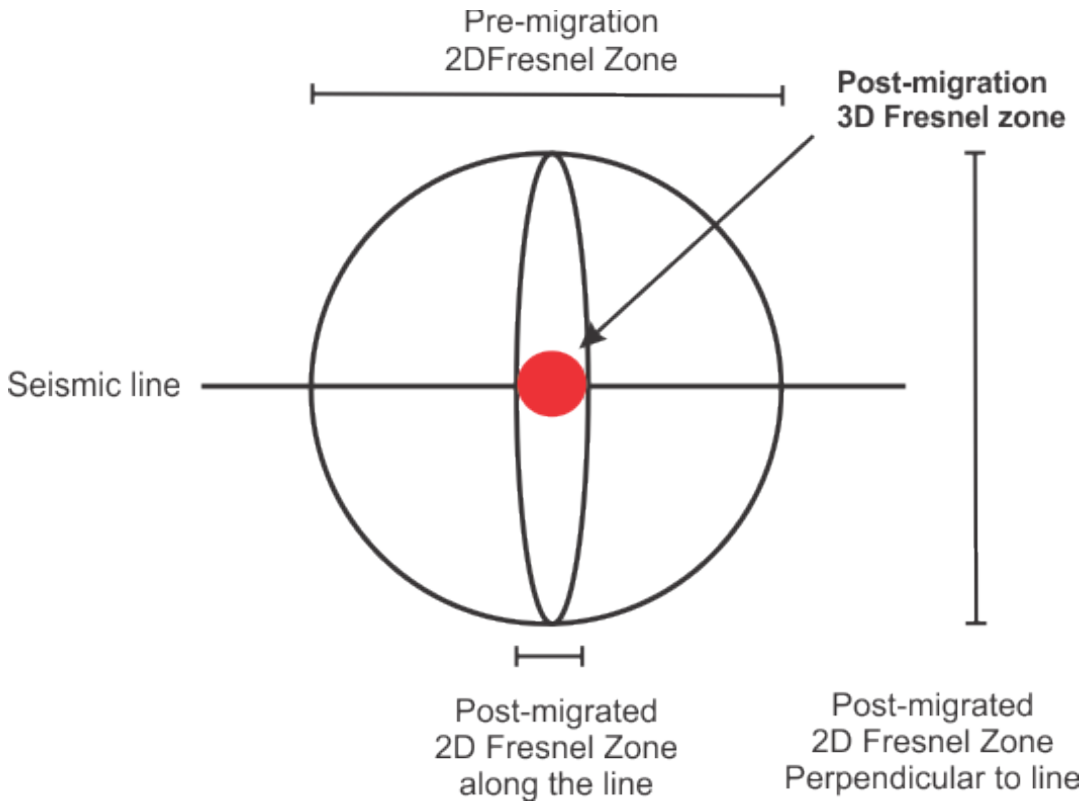

Figure 11. Illustration of the Fresnel zone for 2D and 3D seismic data before and after migration. Modified from Rafaelsen, 2014.

2.1.3 Marine surveying

The basics of acquiring seismic data offshore are very similar to onshore, but simpler, faster, and hence cheaper. To produce the seismic signal in the marine environment an air gun is used to release air into the water creating an acoustic wave. The data quality will usually also be better than onshore seismic because of fewer sources of noise. Usually a number of energy pulses are released from several air guns to create sufficient energy to generate a signal. Depending on the velocity interval the signal may penetrate more than 5 km into the subsurface (Selley, 1998). The reflected signal is recorded with hydrophones towed behind the ship. GPS equipment is used to accurately position the shot-point and the receivers. The basic layout of a marine survey is shown in Figure 12.

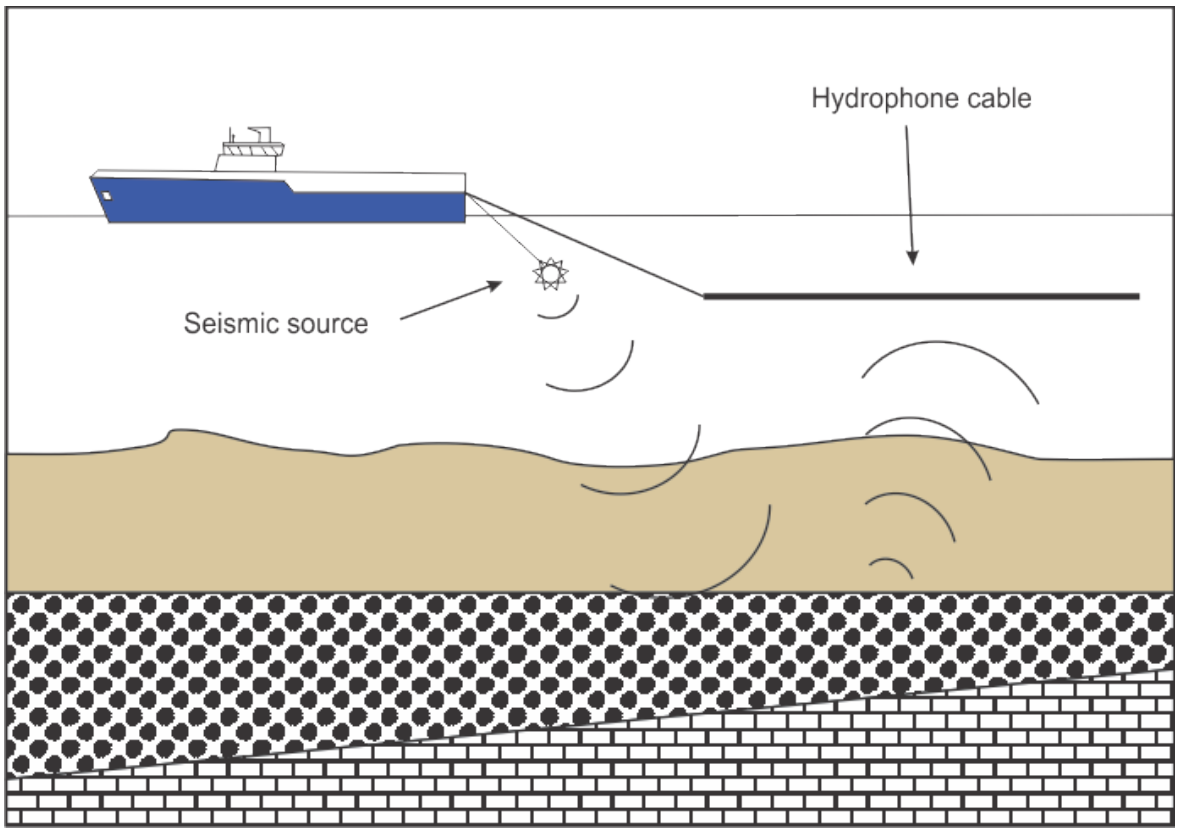

Figure 12. Basic concept of marine surveying, showing how the seismic signal is shot out of the source, reflected off reflectors, and received by the hydrophones. Modified from Geokompendium, 2009.

2.2 Material

2.2.1 Seismic streamer (P-Cable)

Traditional 3D seismic uses closely spaced 2D lines to create a 3D data volume. In contrast, the P-cable system creates a full 3D data set using parallel streamers with high-resolution sources (Petersen et al, 2010) (Figure 13).

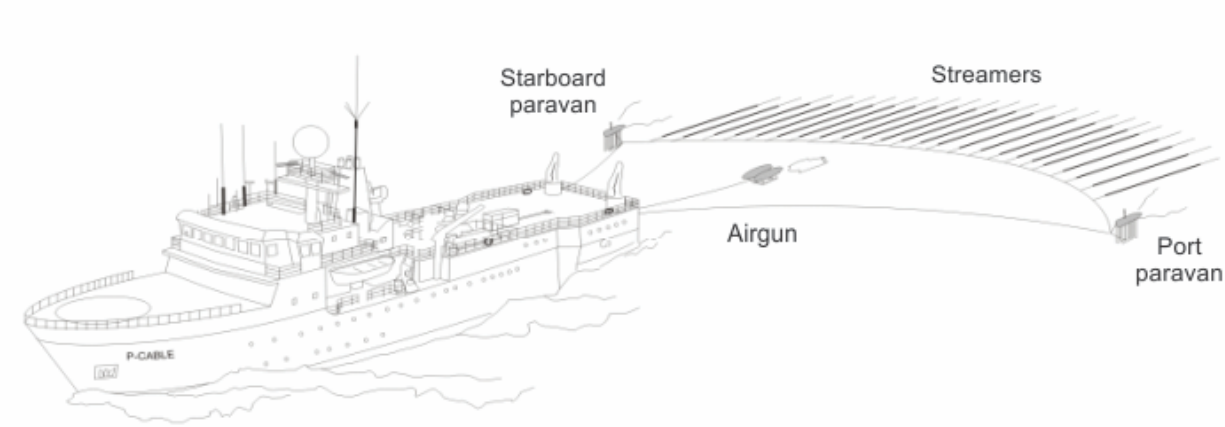

Figure 13. P-cable ship setup. Modified from Pettersen et al., 2010.

The P-cable system differs from conventional 3D systems by having a cable towed perpendicular (cross cable) to the ship's direction on which the steamers are attached (Department of Geology, 2011). The cross cable is controlled by two paravanes towed behind the ship. For the survey a total of 14 streamers were connected to the cross-cable, each streamer is only 25 meters long, much shorter than the several kilometers used in a conventional 3D seismic system. In addition, there is a 6 meter drop-lead connecting the streamers to the cross line. The main advantage of using shorter streamers is that smaller vessels, such as R/V Helmer Hanssen, are capable of towing them. The disadvantage of shorter streamers is that imaging is mostly limited to the first seafloor multiple. The distance between the streamers is about 12.5 meters (Figure 14).

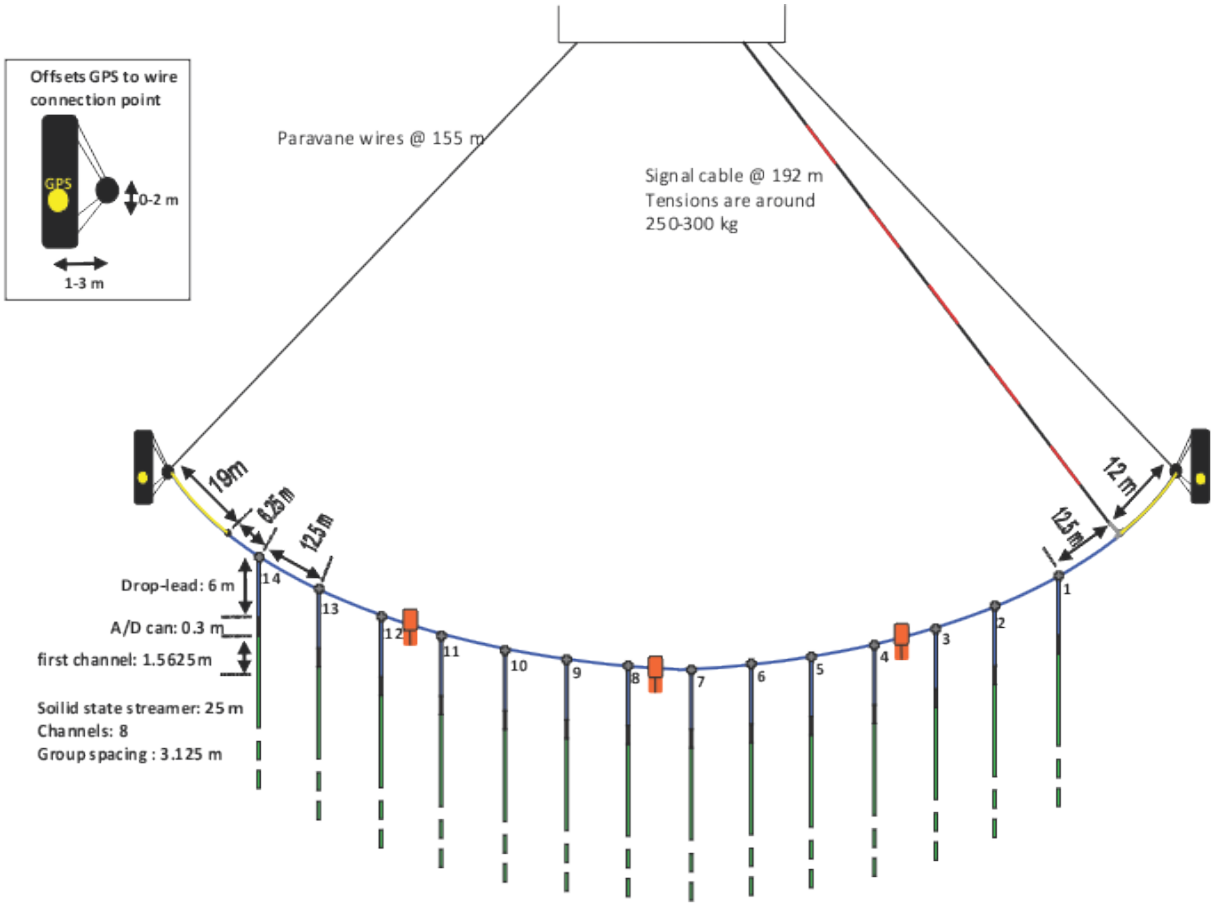

Figure 14. Survey configuration showing the cross cable and the streamers attached to it. From survey ship log.

2.2.2 Seismic Source (GI-gun)

Different seismic sources are used for different surveys because of their different operating frequency ranges. The higher frequencies provide higher resolution, but limited penetration. Lower frequencies have a better penetration, but lower resolution (USGS, 2014).

For this survey, a GI gun (Generator Injector air gun) was used. This uses a technique where a secondary air pulse is injected into the primary air pulse at a short time delay (Geokompendium 2009). This increases the internal pressure of the bubble and prevents its collapse, which in turn dampens the generation of bubble pulse. Figure 15 gives an overview of how this is achieved.

The generator (G) fires an air bubble creating the primary pulse as the bubble expands (Figure 15 A). When the bubble approaches its maximum size the injector (I) is fired, injecting air into the existing bubble (Figure 15 B). This second volume of air increases the

internal volume of the bubble and prevents a violent collapse. The secondary pressure pulse is as a result reduced and re-shaped (Figure 15 C) (GI Gun Manual, 2009).

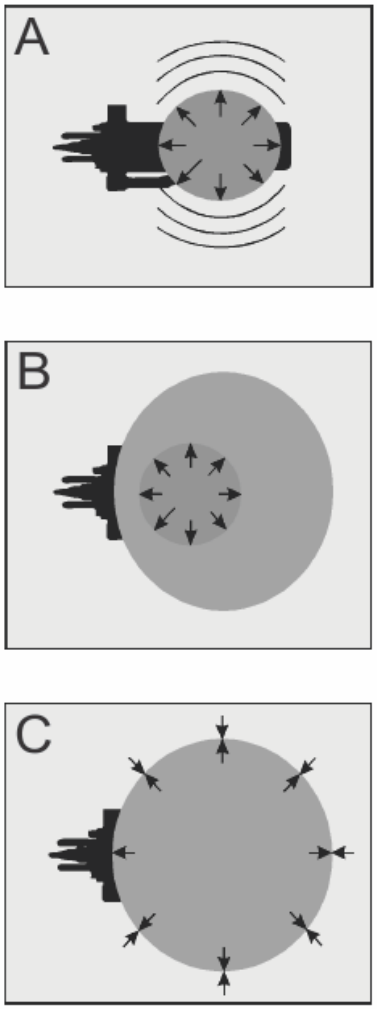

Figure 15. GI-gun firing process. A) The primary bubble being released from the G chamber. B) The injector bubble fired from the I chamber. C) The resulting reshaped bubble. Modified from GI gun manual.

On R/V Helmer Hanssen two GI air guns are used, with variable chamber volumes of either 105 in^3 or 45 in^3. The air gun is towed behind the vessel at a depth of approximately 4 m and a distance of approximately 60 m. For the survey one air gun with a chamber size of 45/45 in^3 was shot at an interval of 4 seconds. By using only one air gun the source energy is lower, however, it was important to have a high as possible shot density.

Both the paravanes and the GI gun are fitted with GPS to position them in relationship to each other, and also within the survey. Accurately positioning the streamers and gun is necessary to calculate the CDP for the receivers.

2.2.3 Interpretation software

The interpretations made of the seismic data were done using the seismic simulation software Petrel. Petrel is used to visualize data, create surfaces, make grids, create geometrical models, and plot data (Petrel, 2011). For this thesis 2D seismic lines were created from the 3D cube, surfaces were created, and several attribute maps and cubes were created in Petrel. All figures created in Petrel are accompanied by the necessary information to understand scales and orientation of the data.

2.3 Survey data

The seismic data from the survey was collected at the Bear Island Trough Fault Complex in the southwestern Barents Sea seen in Figure 16. The dataset is consists of 150 Inlines and 2310 Crosslines (Figure 17).

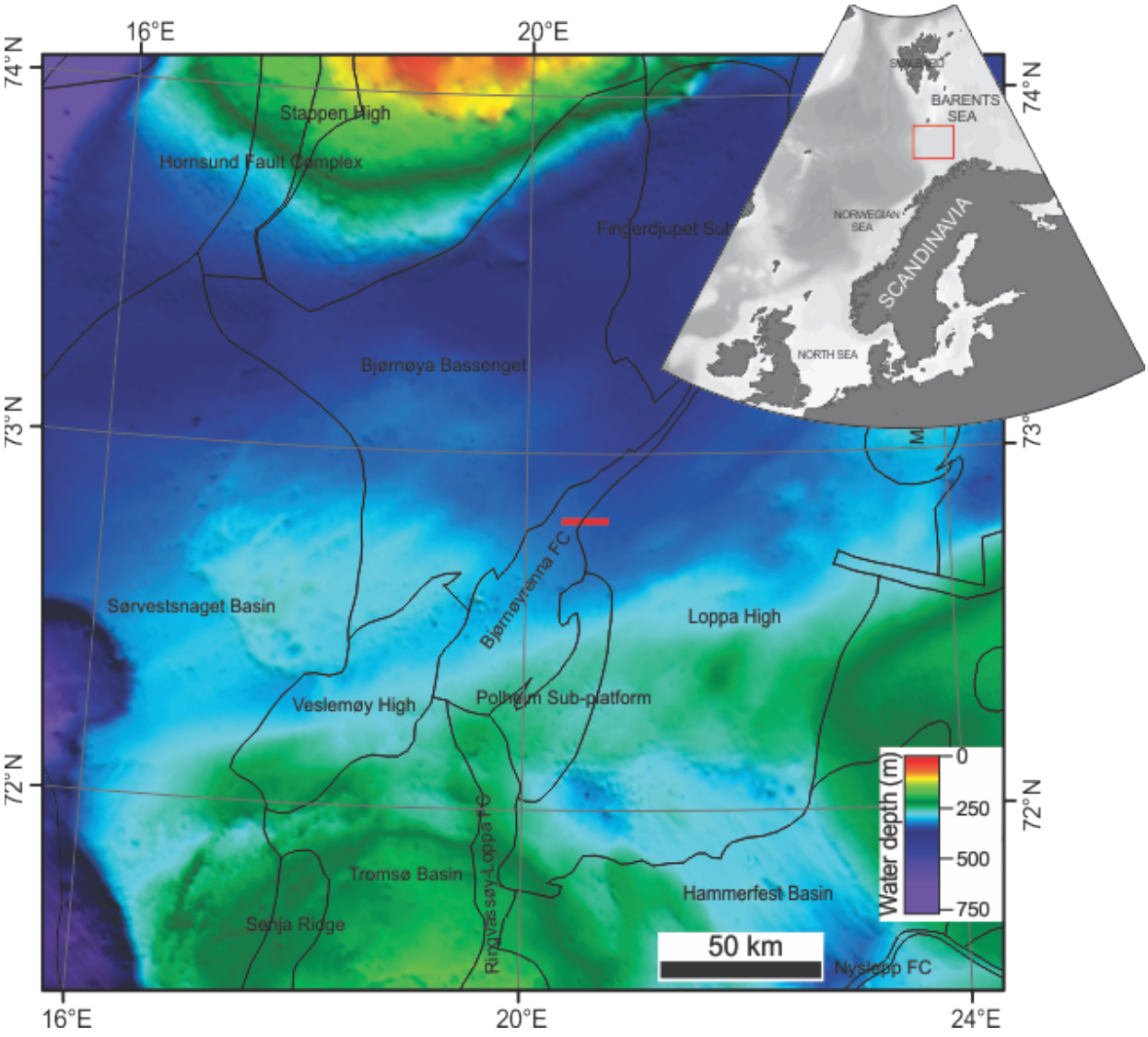

Figure 16. Map showing the location of the dataset within the southwestern Barents Sea. Survey area seen as red rectangle in the Bjørnøyrenna Fault Complex. Figure 17 shows the dataset with inlines and crosslines. Modified from Vadakkepuliyambatta.

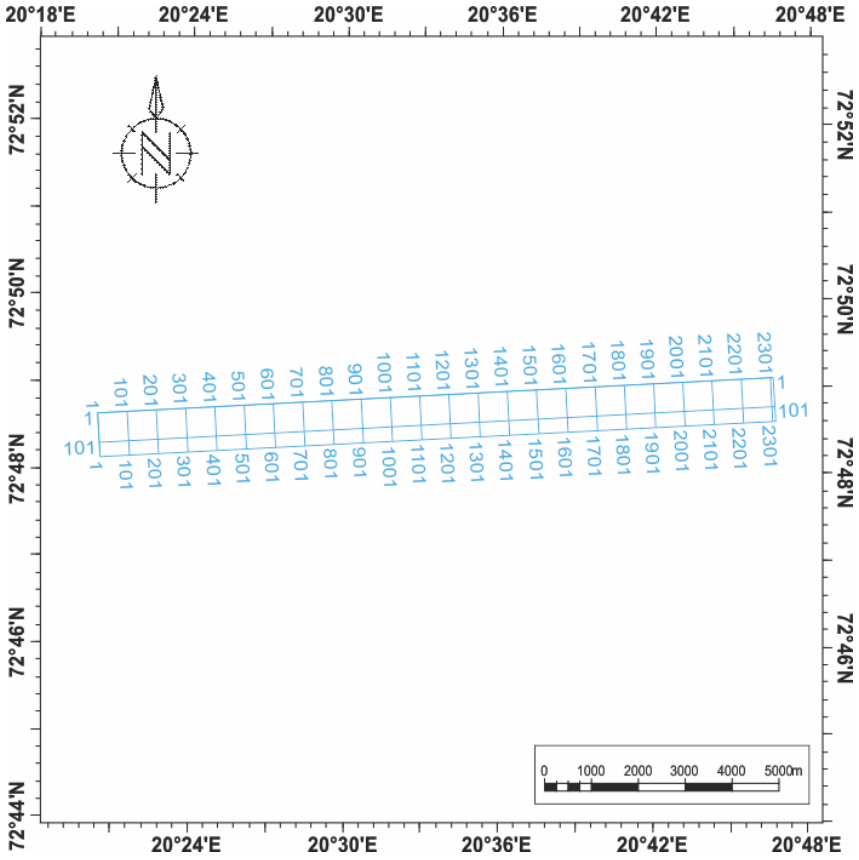

Figure 17. Close up overview map showing location of the 3D seismic cube with its Inlines and Crosslines.

The dominant frequency for the dataset from the seafloor and down to 1000 ms two-way-time (TWT) show three peaks at 55 Hz, 70 Hz, and 80 Hz. At 60 % amplitude the spectrum is between 40 and 110 Hz (Figure 19). The frequency spectrum was collected from the area marked in Figure 18 within the seismic cross section of Inline 100.

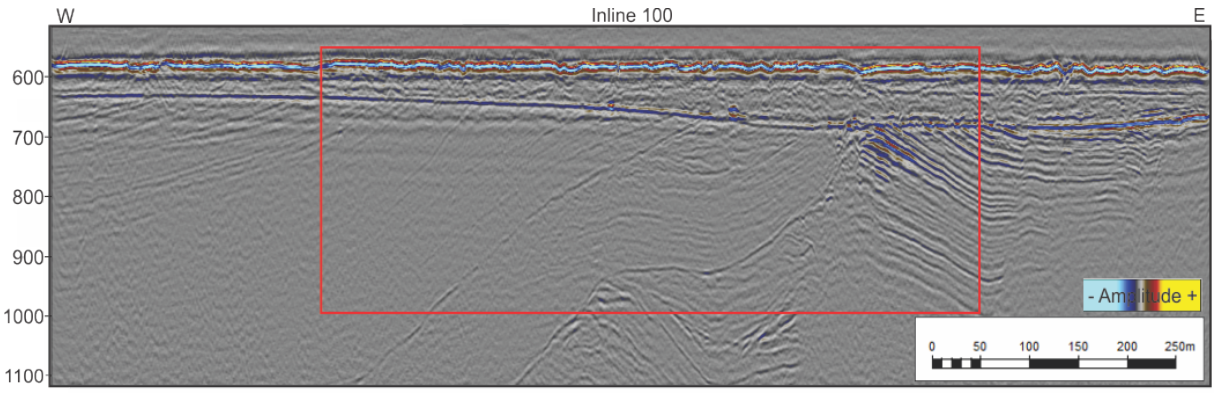

Figure 18. Seismic cross section of inline 100 with red square indicating the area used to calculate the frequency spectrum seen in Figure 19.

By using the peak frequencies within lithological layers, the vertical resolution may be calculated with the equation λ=V/f, and the vertical resolution is ¼ λ. The horizontal resolution before migration can be calculated with the equation: $rf=V/2\ (t/f)^{1/2}$. The horizontal resolution after migration is given by ¼ λ. The TWT (t) for the Neogene sediments is 0.615 s, Torsk FM 0.750 s, and Kolmule 0.900 s. The average velocities are interpreted from Figure 6, Chapter 1.1.2. The results of these equations are given in Table 1.

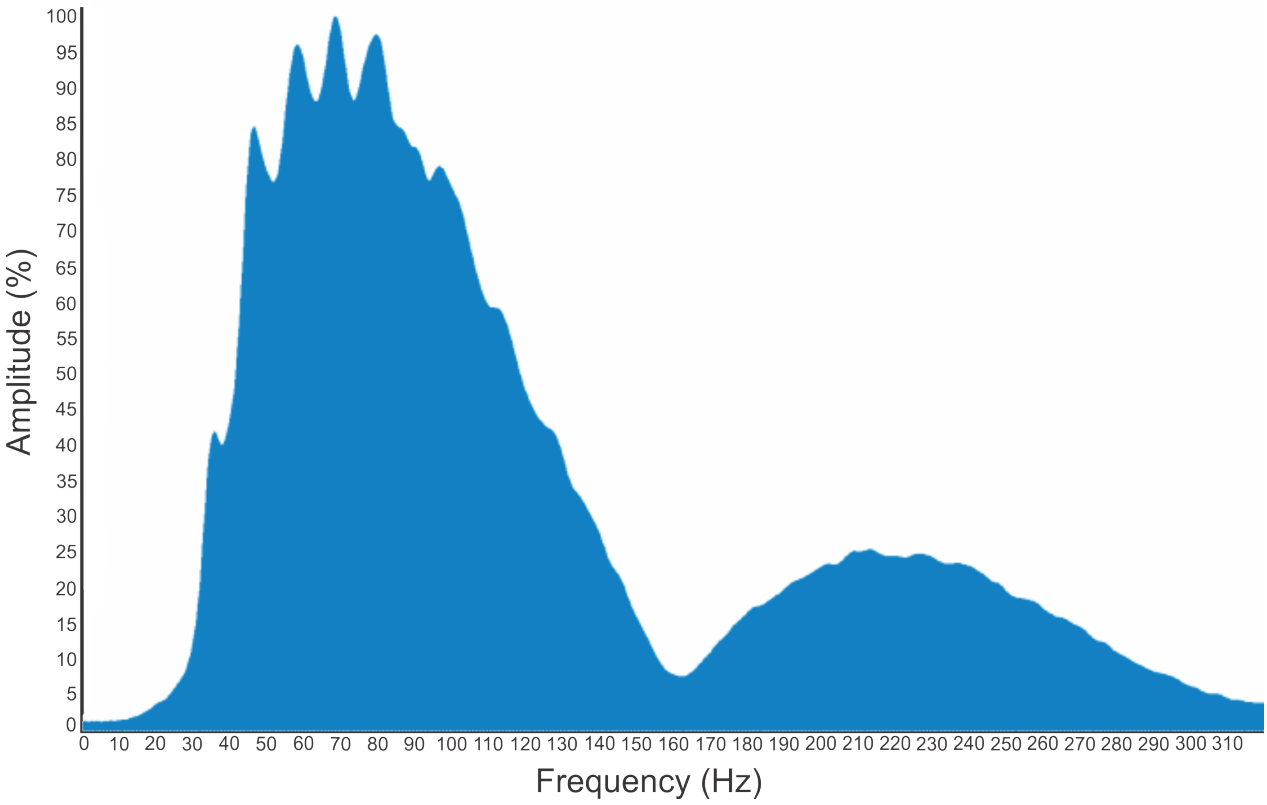

Figure 19. Frequency spectrum from inline 100 showing the three peaks with dominant frequencies of 55 Hz, 70 Hz, and 80 Hz. And a frequency spectrum of 40 to 110 Hz at a 60 % amplitude.

Dominant frequency	Lithological layer	Wavelength λ=V/f	Vertical resolution (m)	Horizontal resolution (m), before migration	Horizontal resolution (m), after migration
80	Neogene (1750m/s)	21.87	5.47	76.65	5.47
67	Torsk FM (1800 m/s)	26.86	6.71	95.4	6.71
45	Kolmule FM (1850 m/s)	41.11	10.28	130.4	10.28

Table 1. Vertical resolution and horizontal resolution before and after migration given for the peak frequencies in the most prominent lithological layers.

3 Processing

In this chapter, the steps taken to process the seismic data to the final migrated 3D-seismic volume are discussed.

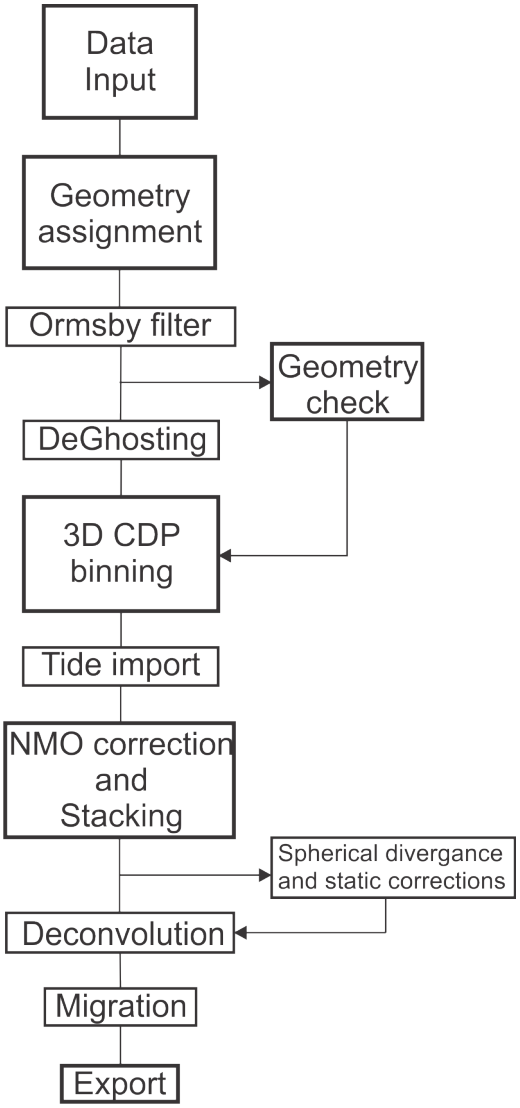

Figure 20. Illustration showing the processing steps taken, and the order they were done.

Processing is a necessary step for all seismic data in order to make the raw seismic data open for interpretation. The goal of processing is to get the best signal to noise ratio and obtain a correct image of the geological boundaries and features. Noise is a term covering all phenomena not related to the actual geology. Seismic processing can attenuate noise, but will never completely remove it. Random noise has no particular pattern and generally only degrades the quality of the seismic section. For an offshore survey like this one, random noise is generated by waves, bad weather, equipment being used on the ship, and other ships surveying the area (Geokompendium, 2009).

The processing can be divided into common steps (Figure 20) that will be discussed in further detail. Some processing steps are mandatory, while other steps vary depending on the dataset, the quality one wants to achieve, and the time available for processing. The navigation data from the GPS points was processed to achieve accurate streamer channel and shot coordinates (Figure 21 and 22). This was done earlier and added to my data during the input stage. Picking of the direct wave is done to calculate the true source-receiver offset. This is followed by tidal corrections, various filtering, NMO corrections, stacking, and migrating. For each step

described below I have chosen to provide some background theory prior to application to the data which results in a more coherent reading than separating theory and application into two different chapters.

For this thesis, the processing software RadExPro Professional, version 2014.1 was used. This software was developed by DECO Geophysical for advanced processing of 2D/3D near-surface reflection data, field processing and quality control of deep 2D/3D seismic data, processing of refraction seismic data, analysis of surface waves and processing of VSP data (RadExPro manual, 2014).

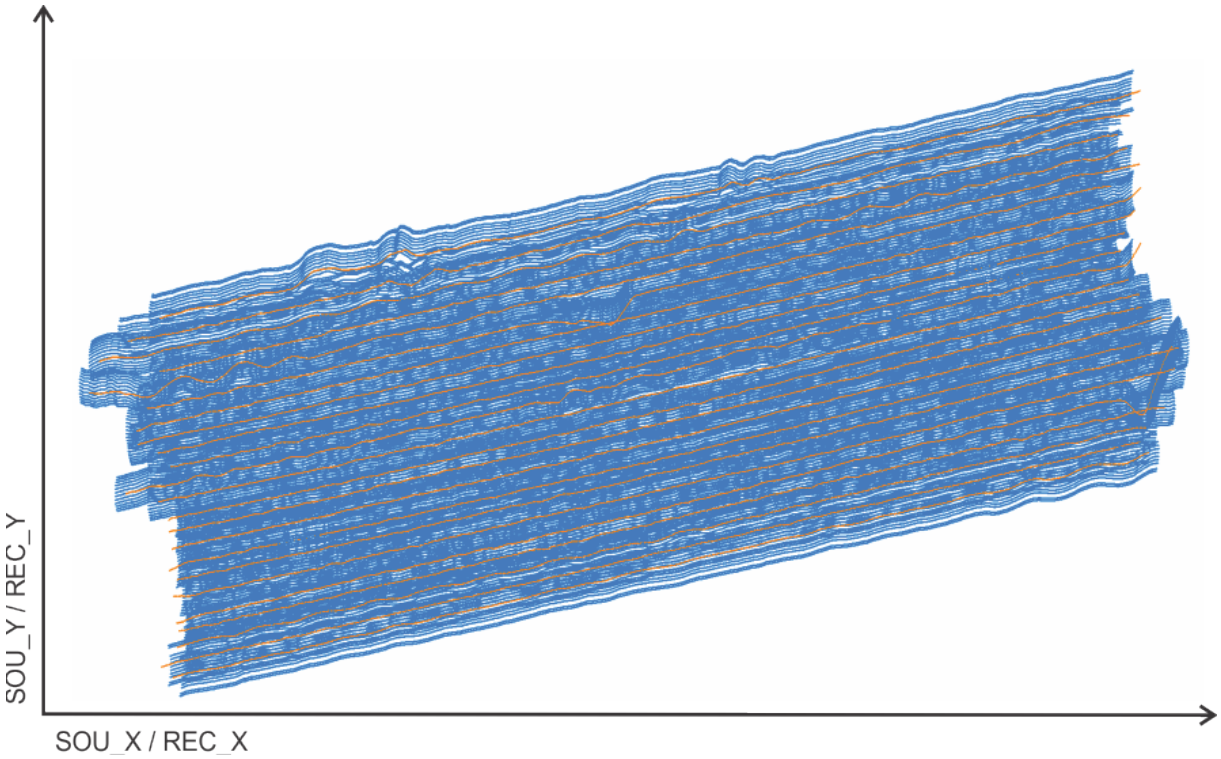

Figure 21. All Shot points and receiver points for the entire survey. Shot points seen as orange dots, and receiver points as blue dots. Close up of a single line can be seen in Figure 22.

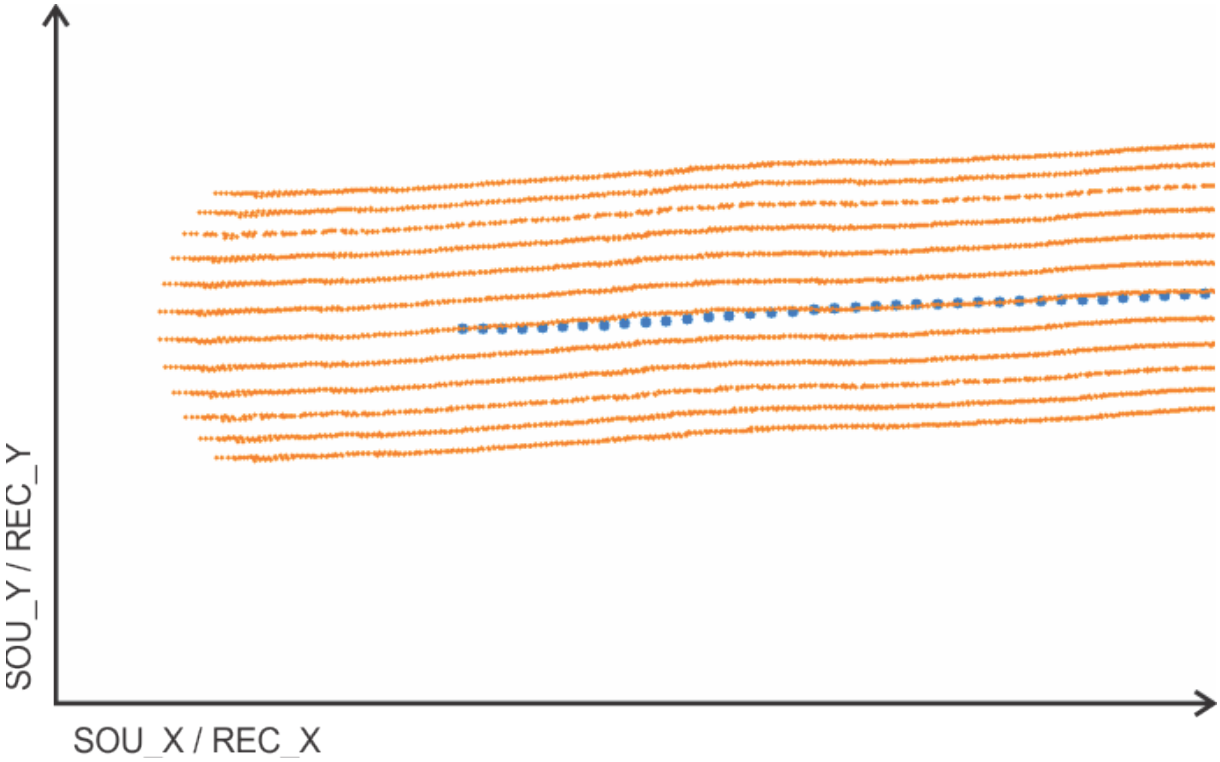

Figure 22. Shot points (source) shown in blue plotted against receiver points in orange. From the beginning of Line 3 raw data.

3.1 Data input and header assignment

The first step in processing is to create a project. For this dataset the project is called "Bjornoyrenna" and uses the data from the Lundin 2012 Area A survey. All the data processing is done within a processing project, which includes different types of data, their geometry and the processing flows applied to the data (RadExPro manual, 2014).

The project is divided into Area, which contains Lines, Lines which represent one line of seismic data from the ship's survey, and Flow which are the modules added to each Line to include different processing elements. The main page of RadExPro showing the Area with the Lines and the Flows within the Lines is presented in Figure 23. The raw P-cable seismic data containing 36980 shot points collected during the survey are stored as SEG-D files, which are loaded in-to the RadExPro program. Figure 21 gives an indication of the extent of the survey by showing data points in the dataset using the CDP points (pre-binning) for the survey.

The first flow consists of a SEG-D data input, Trace Header Math, Data Filter and Trace output modules. The SEG-D input is a basic module used to import SEG-D files into the flow.

The Trace Header Math module is designed for doing mathematical operations with header values (RadExPro manual, 2014). This is done by adding equations that produce the required changes to headers. The Trace Header Math module for Line 1 is shown in Figure 24. Here examples of adding values to headers can be seen, such as “S_LINE=1” defining this data as Line 1. Changing the header value, “CHAN = [CHAN] + 8” where 8 is added to the channel numbers since, for this Line, it begin on channel 9 instead of 1. Specifications for the DAY header where done for when the date changes as the survey time passes midnight. The header values are important throughout the processing procedures so making sure that the values are correct is a necessary step.

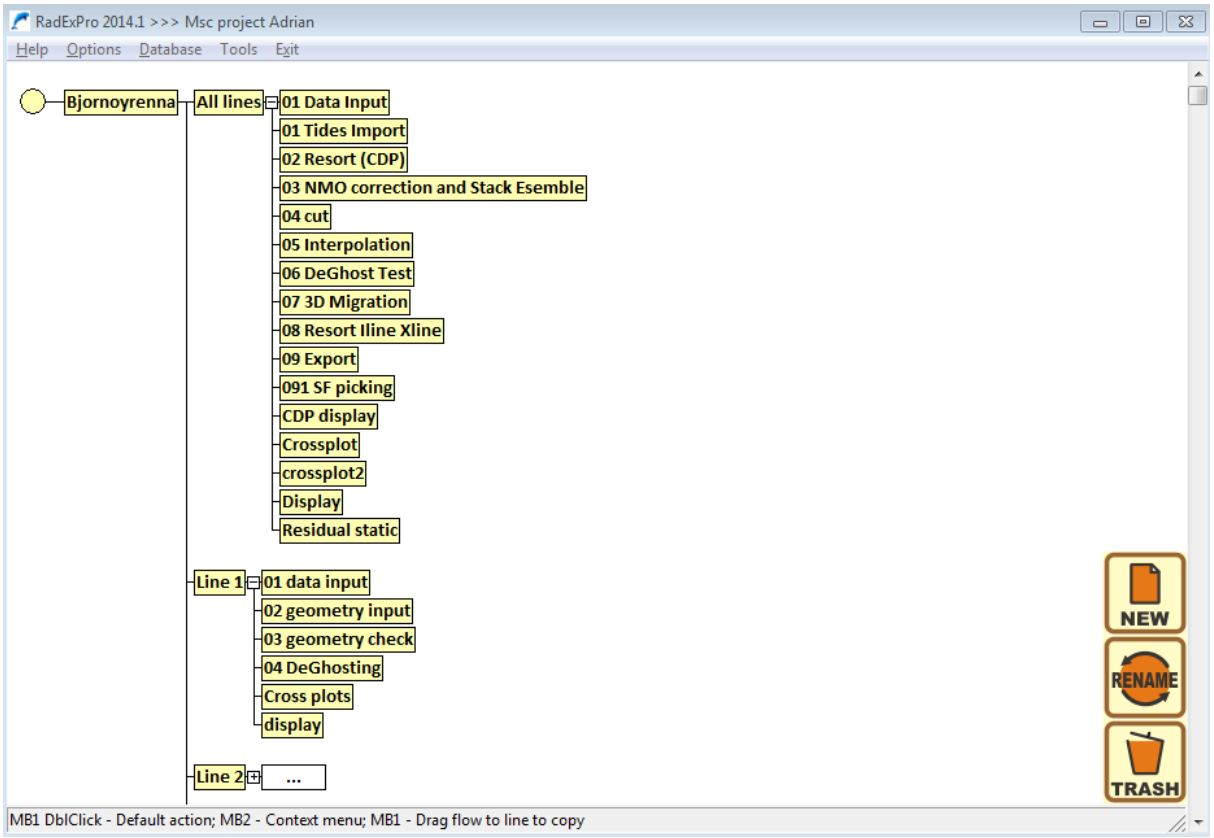

Figure 23. Screen shot of the RadExPro program showing the Area, Bjornoyrenna, the Lines, Line 1, and the Flows within the Lines. This shows what the main screen of a RadExPro project looks like.

For some of the Lines an additional module for Data Filtering is needed, to remove data that does not belong in the Line. For Line 1 a data filter matching the selected “channel 1-104” was used to keep data for channel 1-104 and remove all other channels. This was done because there are only 104 channels for Line 1 instead of the normal 112.

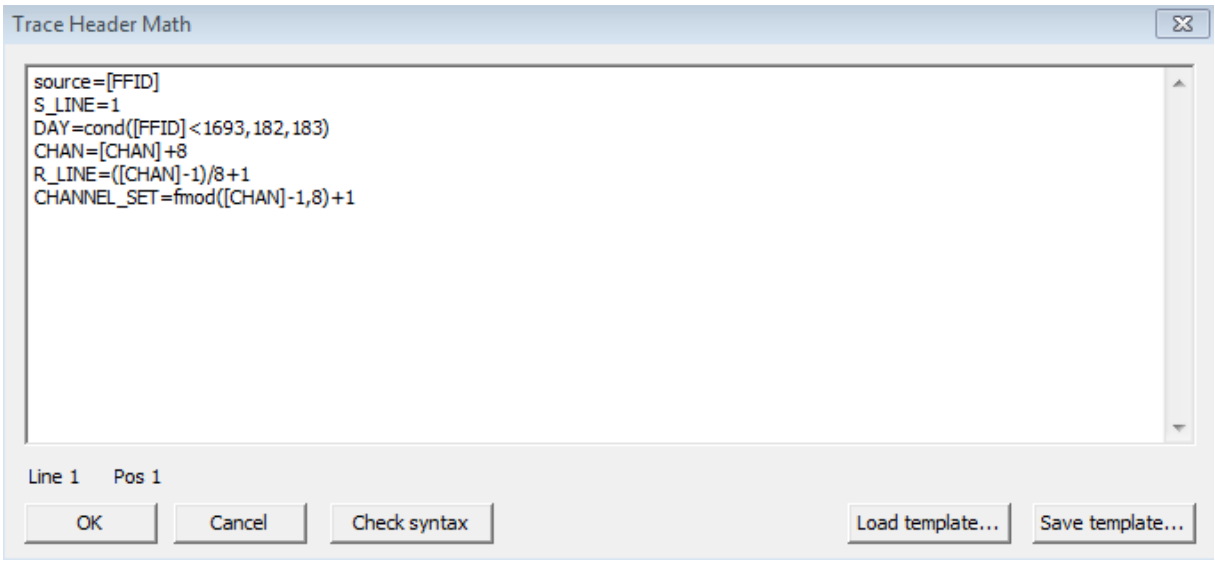

Figure 24. Screen shot example of the Trace Header Math module for Line 1. Showing how equations are added to change header values.

At the end of the flow, a screen display module may be used to view the raw shot data. Figure 25 shows the screen display module with the direct wave at about 100 ms (TWT), seafloor reflection and evidence of sub-bottom reflections are visible. Figure 25 shows part of Line 1 raw data, for channel 100 after geometry has been assigned but without any filtering. Once the data input flow has been used to create the necessary headers and sorted the data, the raw data file, which will be used for further processing is created.

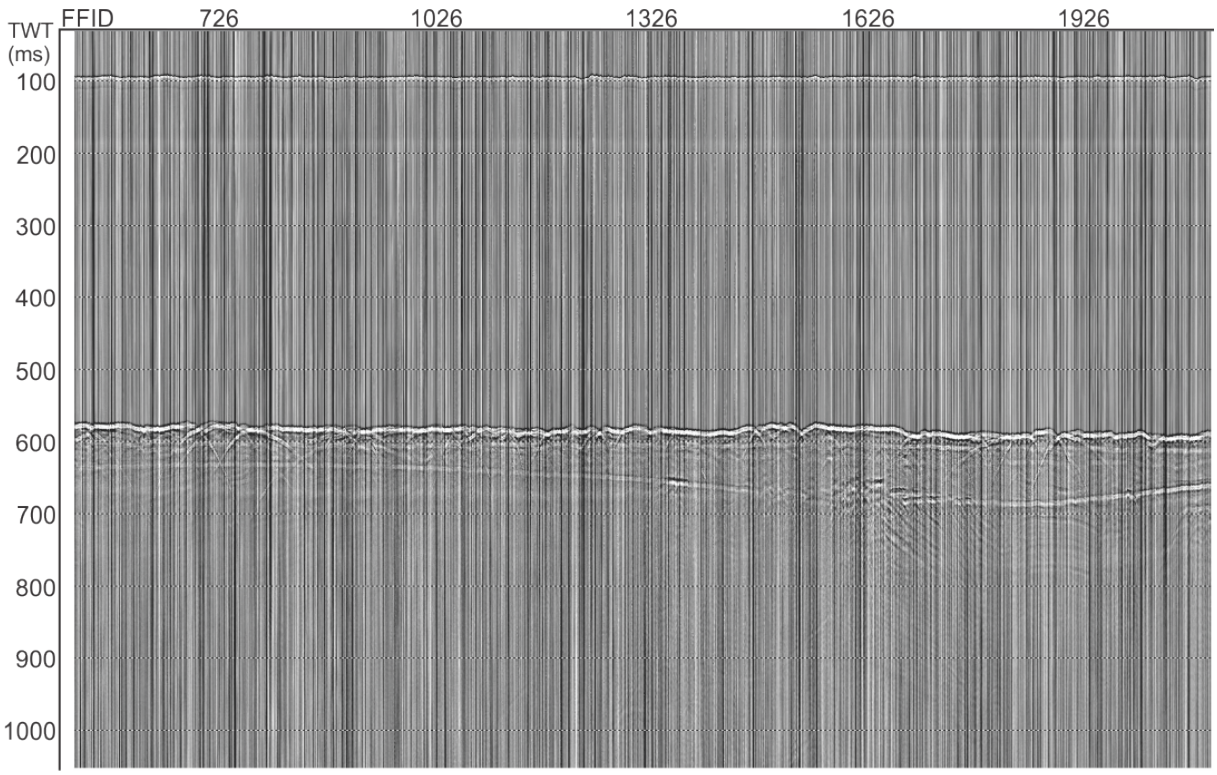

Figure 25. Screen display of Line 1 RAW channel 100. After importing the SEG-D data and assigning geometry, the seismic data appears like this and is the base for the continued processing. The direct wave can be seen at 100 ms (TWT) and the seabed at about 600 ms (TWT) with reflections seen below.

3.1.1 Geometry assignment

After creating the data input flow and concluding that the data looks correct, a new flow is added to the Line in order to assign geometry to the data. The navigation data from the survey has been processed beforehand, so only the assigning remains. The P-cable Geometry module shown in Figure 26 is the only module used in this flow. Several pieces of information are needed for the geometry assignment. Most of these are found in the ship log, where the streamer geometry information is kept. The basic setup of the gun and streamer are discussed in the previous chapter (Figure 14, Chapter 2.2.1), however the geometry is not the same for every line and so must be checked for each line in the ship log as well.

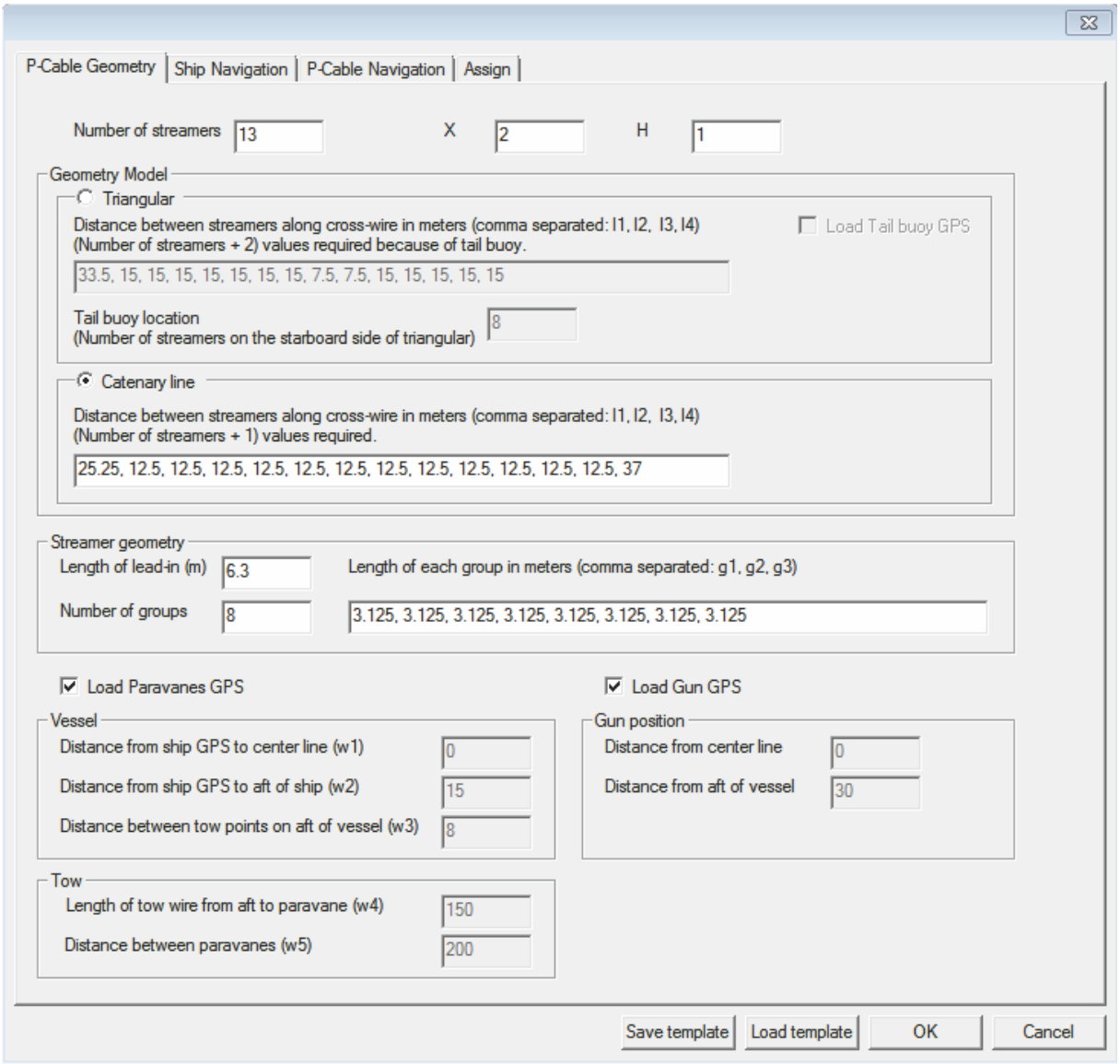

Figure 26. Screen shot of the P-Cable geometry input module for Line 1. The module is used to add streamer data and GPS data to the seismic data for the line.

The P-Cable geometry including number of streamers, the shift of the edge streamers relative to the paravanes, and the distance between each streamer along the cross line. For example, only 13 of the 14 streamers were used for Line 1 changing the P-Cable geometry from the default survey configuration seen in Figure 14, Chapter 2.2.1.

For the next two tabs of the geometry input module, the ships navigation files are assigned. The navigation files contain time in hour, minutes and seconds, and UTM_X/UTM_Y coordinates for the ship, gun, and port- and starboard-paravanes. In addition, the start date for the Line must be added manually in the module. The navigation data is added separately

for the ship and the P-cable setup. Since the navigation files for this dataset were pre-processed, they only needed slight adjustments before uploading to RadExPro. These adjustments include converting the files to a text format (.txt) that RadExPro would read, changing times and dates to the correct time zone, and removing data points not applicable for the Line in question.

3.1.2 Geometry check

After assigning the geometry to the data a “geometry check” of the line is necessary to make sure the offset is correct for the lines. This is done by Picking the direct wave to calculate the source-receiver offset. The offset is the distance between the source and the receiver. For the geometry check a horizon is created, Pick 1 (Figure 27), with the approximate water velocity (v = 1500 m/s). This will create a horizon following the theoretical first arrival of the direct wave. We can see in Figure 27 a wiggle display of the direct wave and the calculated theoretical first arrival indicated by the red line.

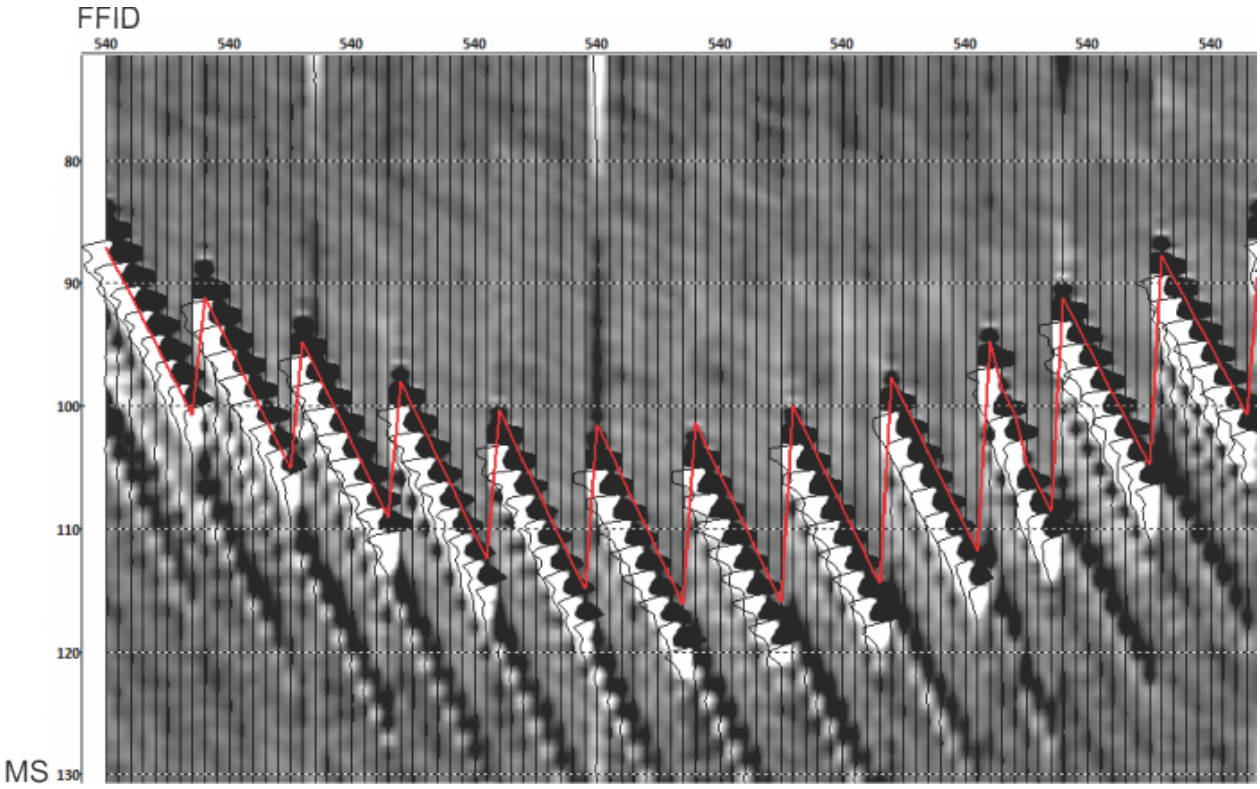

Figure 27. Screen shot of geometry check process for a part of Line 1, where Pick 1 calculated with the theoretical first arrival is indicated by the red curve, and indicates how well the given geometry fits with the wiggle display of the direct wave.

The Pick 1 header, representing the offset, is calculated with the use of the following equations in trace header math:

$$offset = \sqrt{([sou_x]-[rec_x])^2 + ([rec_y]-[sou_y])^2}$$

$$pick1 = \frac{[offset]}{1.5}$$

If the difference between the theoretical Pick 1 and the actual signal is too large or has errors, an offset correction is necessary to recalculate the Pick and adapt the geometry.

To correct the offset a new horizon, called Pick 2, is created using the Seismic Sequence Attribute Analysis (SSAA) module. The module calculates trace attributes in a window along an indicated horizon, and writes the seismic attributes to database headers (RadExPro manual, 2014). For the offset correction, the SSAA module was used to automatically find the peak amplitude time within a set window around a chosen horizon, since the first break is the first amplitude increase after the zero-crossing. Using Pick 1 as the horizon and a window of 10 ms (for Line 1) it is possible to select a better horizon for the offset. In Figure 28 both Pick 1 and the new Pick 2 are seen, where Pick 2 has been calculated using the SSAA module and Pick 1.

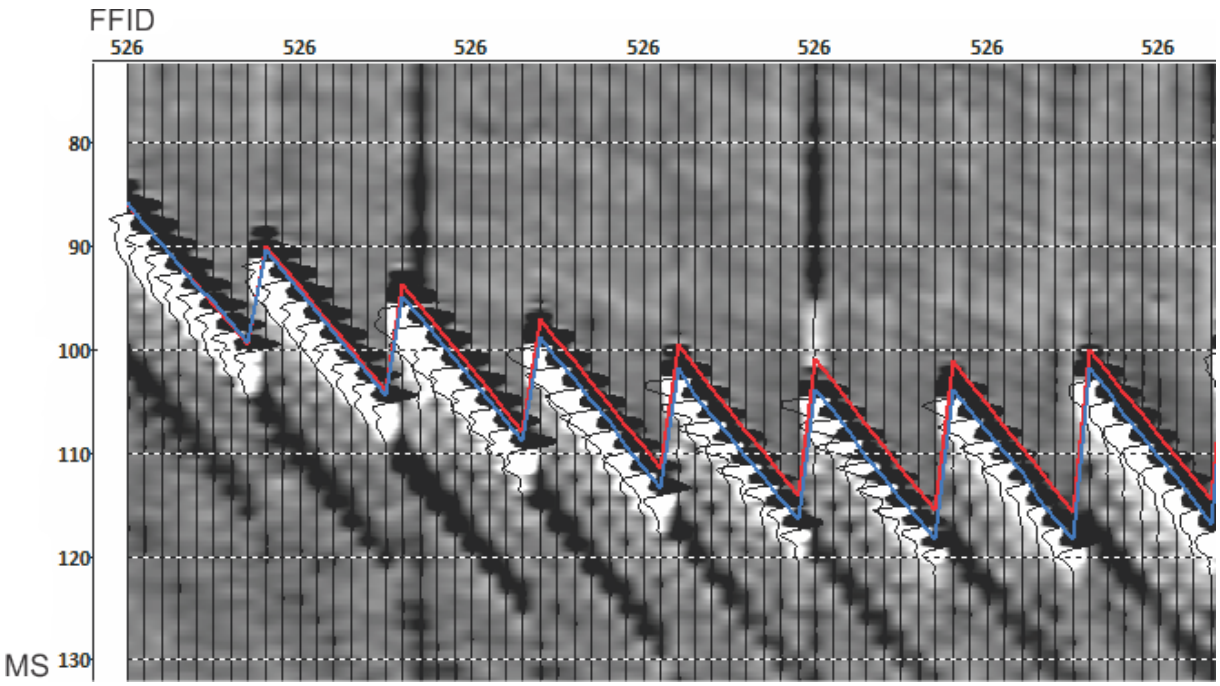

Figure 28. Screen shot of part of Line 1 showing Pick 1 as red horizon and the SSAA calculated Pick 2 as blue horizon. The difference between the two horizons vary across the line.

For some Lines, a third offset needs to be calculated since the second Pick is not accurate enough. This is done by using the Trace Header Math module to add or subtract the value needed to adjust the offset horizon and in some cases removing bad shot points that cause problems for the automatic Picking.

After assigning the geometry, and checking and confirming the offset of each Line, all the 23 2D lines were added together by multiple import to create one data file containing the entire dataset. By doing so we can create the CDP header by assigning traces to the CDP points using the 3D CDP binning tool.

3.1.3 Common mid-point

When assembling seismic data, reflections come from different parts of the interface. However, it is possible stack the data using rays reflected from the same part of the interface, which is called Common Mid-Point (CMP) surveying (Mussett, 2000). The Common Mid-Point gather is equivalent to the Common Depth Point gather when reflectors are horizontal and velocities do not vary horizontally (Geokompendium, 2009). RadExPro uses CDP points instead of CMP points so these will be interchangeable in this thesis. CMP

surveying is based around the principle of duplicating the subsurface coverage by recording successive data about a Common Mid-Point between the source and receiver. The traces with the same midpoint are sorted together, creating a CMP gather. A seismic survey using multifold coverage is done in shot-receiver coordinates, although the seismic processing is done in midpoint-offset coordinates. By sorting the data into CMP gathers, the required coordinates are achieved (Geokompendium, 2009). One of the main reasons for wanting a CMP gather is the ability to correct for Normal Move-Out (NMO). The traces will then have the same reflective pulses at the same time, but different random and coherent noise (Keary, 2002). This allows the traces to be stacked.

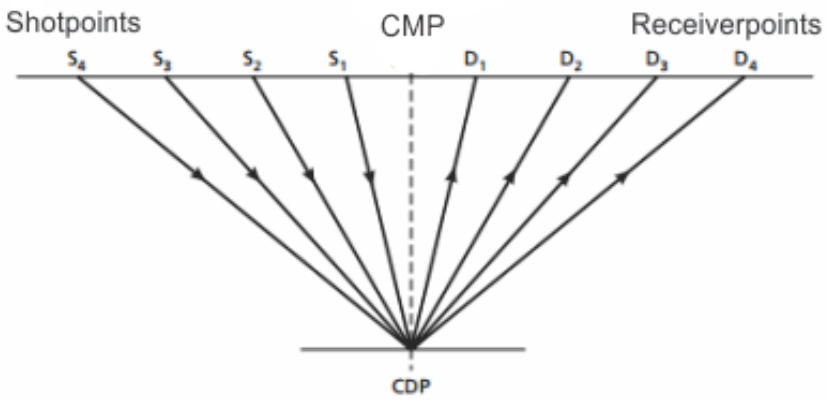

Figure 29. CMP stack illustration showing shot-points S1 through S4 and the receiver points D1 through D4 about a Common Mid-Point. Modified from Mussett, 2000.

As shown in Figure 29, a Common Depth Point is created due to successive shots being received by successive receivers. The number of channels added together is termed the fold, as in Figure 29 where it is fourfold (Mussett, 2000). The fold coverage is given as:

$$fold = \frac{n_g \Delta g}{2\Delta s}$$

Where Δg = the receiver-group interval, Δs = shot interval, and n_g is the number of recording channels.

The 3D CDP Binning is done through the tool menu in RadExPro instead of a flow. The CDP coordinates are calculated for each of the traces by creating a geometry table: X = (REC_X + SOU_X)/2 Y = (REC_Y + SOU_Y)/2.

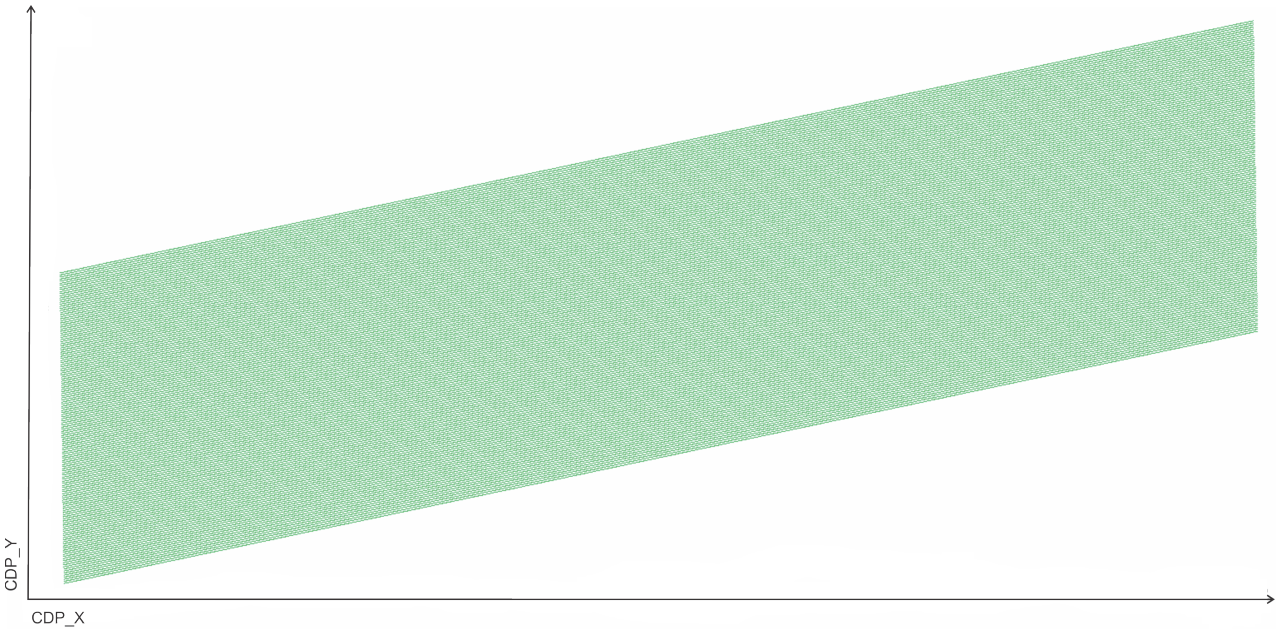

Figure 30. CDP points for the dataset created through 3D CDP Binning.

These coordinates are then used the binning mode (RadExPro manual, 2014). The binning mesh is used to select the scale of the area, and the X and Y step (horizontal and vertical size of the cells), which is 6.25 for this dataset, then assigns the CDP values to the selected dataset (Figure 30). This is done to create the Inline and Crossline headers in addition to the CDP values to the dataset, creating the required CDP gathered.

3.2 Filtering

Filters are a necessary step of processing to reduce the amount of unwanted data, reduce the signal to noise ratio, and improve the resolution. The seismic wave is always a combination of signal and noise where the signal represents the part of the waveform that shows geological structures of interest, and the noise represents all the other parts of the waveform. The noise can then be subdivided into random and coherent noise. Random noise is statically random and the result of weather conditions such as wind and waves, other equipment on the survey vessel, and other ships in the area. Coherent noise are true reflections, such as surface waves or multiples, which are not of any interest for the research (Keary, 2002). Filtering is mainly used to increase the signal to noise ratio by removing unwanted noise.

3.2.1 Multiples

Multiples are reflections that have undergone more than one reflection. An example of this is where the energy reflected back to the surface from a reflector, bounces off the air/water interface back into the subsurface before returning to the surface to be recorded. This will give the reflector approximately twice the length of the primary ray path (Figure 31) (Geokompendium, 2009). Multiples are divided into two main types; long-path and short-path.

The most common and important long-path multiple is the seabed / water-bottom multiple (Figure 31). This is due to the high impedance contrast between the air and water. These multiples can often be attenuated by CMP stacking (Chapter 3.3.2), but because of the short streamer length used for this survey they cannot be properly removed trough stacking. This lead to the choice of cropping the 3D-seismic volume at the first seafloor multiple.

The most common short path multiple are Ghosts (Chapter 3.2.3) (Figure 31). These occur during marine surveying when a pulse that initially traveled upward is reflected off the water-air interface and continues as a down going pulse. This results in the Ghost reaching the hydrophones slightly after the primary signal. Ghosts and how to attenuate these multiples are discussed further in Chapter 3.2.3.

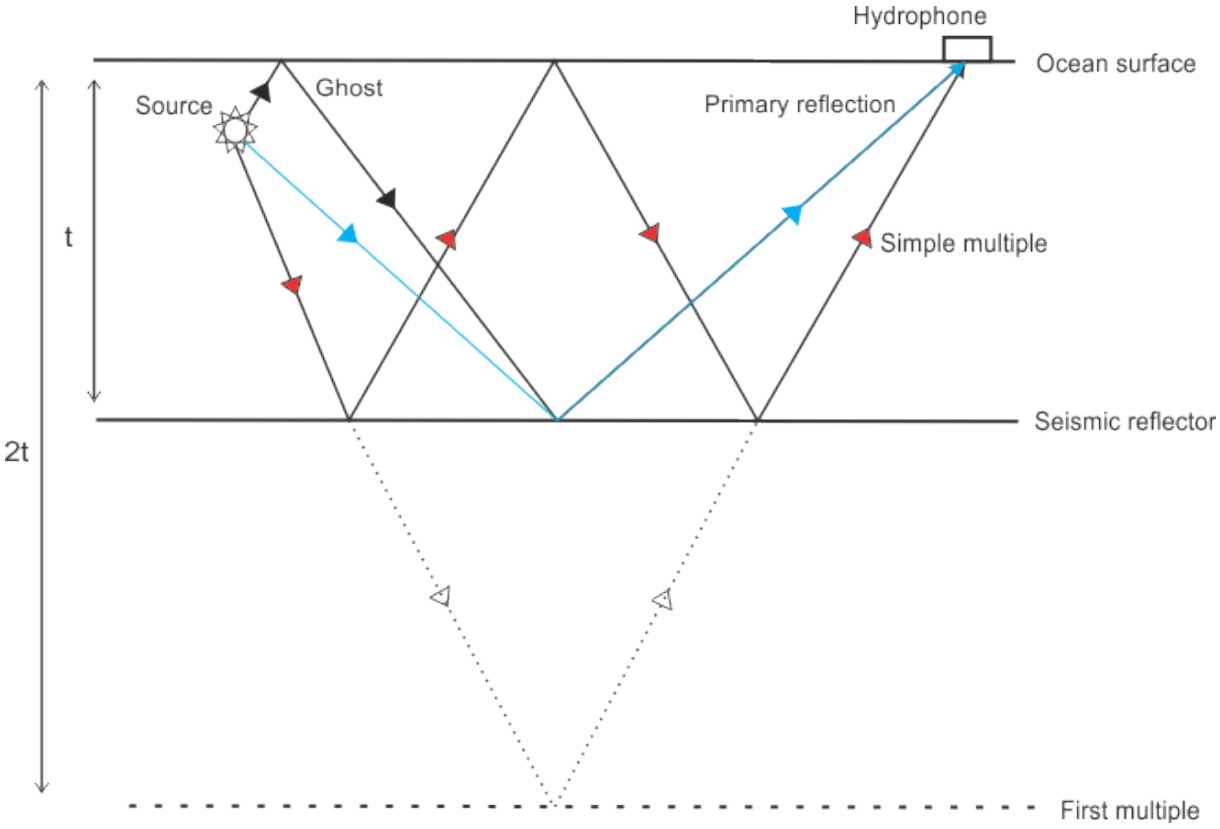

Figure 31. Illustration of simple multiples. The primary reflection shown in blue. The seabed / water-bottom multiple shown with red arrows, and with dashed line to show how it has twice the TWT of the primary reflection. Also the ghost multiple shown with black arrows, which will arrive slightly after the primary reflection.

3.2.2 Ormsby filter

By using the Average Amplitude Spectrum window in the screen display module, we can see a strong low frequency noise below 25Hz (Figure 33 A). This is quite normal for this kind of high-resolution offshore seismic data, and is the result of the noise related to the ship. To attenuate this noise, the Bandpass filtering module, which applies frequency filtering to every input trace, is used (RadExPro manual, 2014).

To achieve a better signal to noise ratio an Ormsby Bandpass filter was used to remove the ship generated noise. Ormsby wavelets are zero-phase wavelets with a trapezoidal shape filter (Figure 32 B) which when applied to a unit impulse function creates the Ormsby wavelet (Figure 32 A) (Ryan, 1994). The filter has several side lobes, which will increase with the steepness of the trapezoidal sides.

The Ormsby wavelet uses four frequencies to specify the shape of the filter. These frequencies are referred to the low-cut frequency (f_1), the low-pass frequency (f_2), the high-pass frequency (f_3), and the high-cut frequency (f_4) which are all used to generate the

Ormsby wavelet (Ryan, 1994). The cut-off frequencies used for this dataset were; low cut 10 Hz, low pass 20 Hz, high pass 500 Hz, and high cut 800 Hz. The frequencies are used to construct a window of the spectrum that will be removed by the filter. By using the screen display module, we can plot an amplitude spectra for a selected area, as seen used on the seabed in Figure 33 B. By inspecting the frequency spectrum, the correct parameters for the bandpass filter can be chosen.

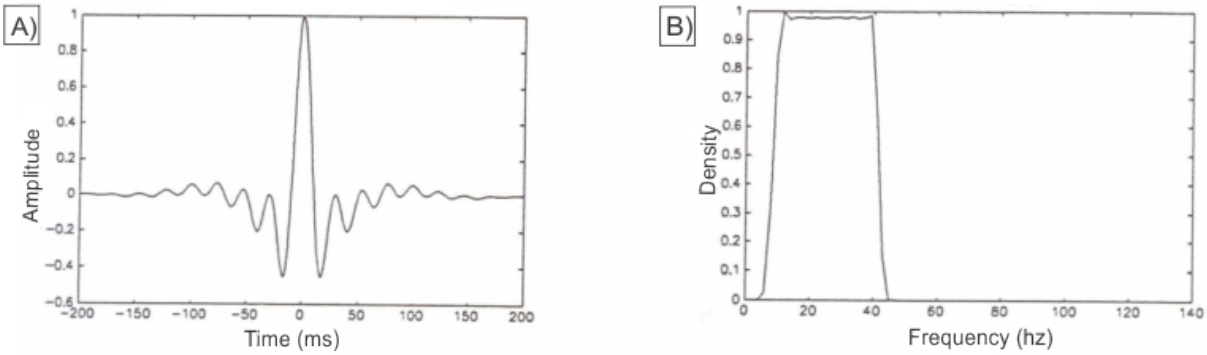

Figure 32. A) Ormsby wavelet in the time domain. B) Ormsby wavelet in the frequency domain (right). Modified from Ryan 1994.

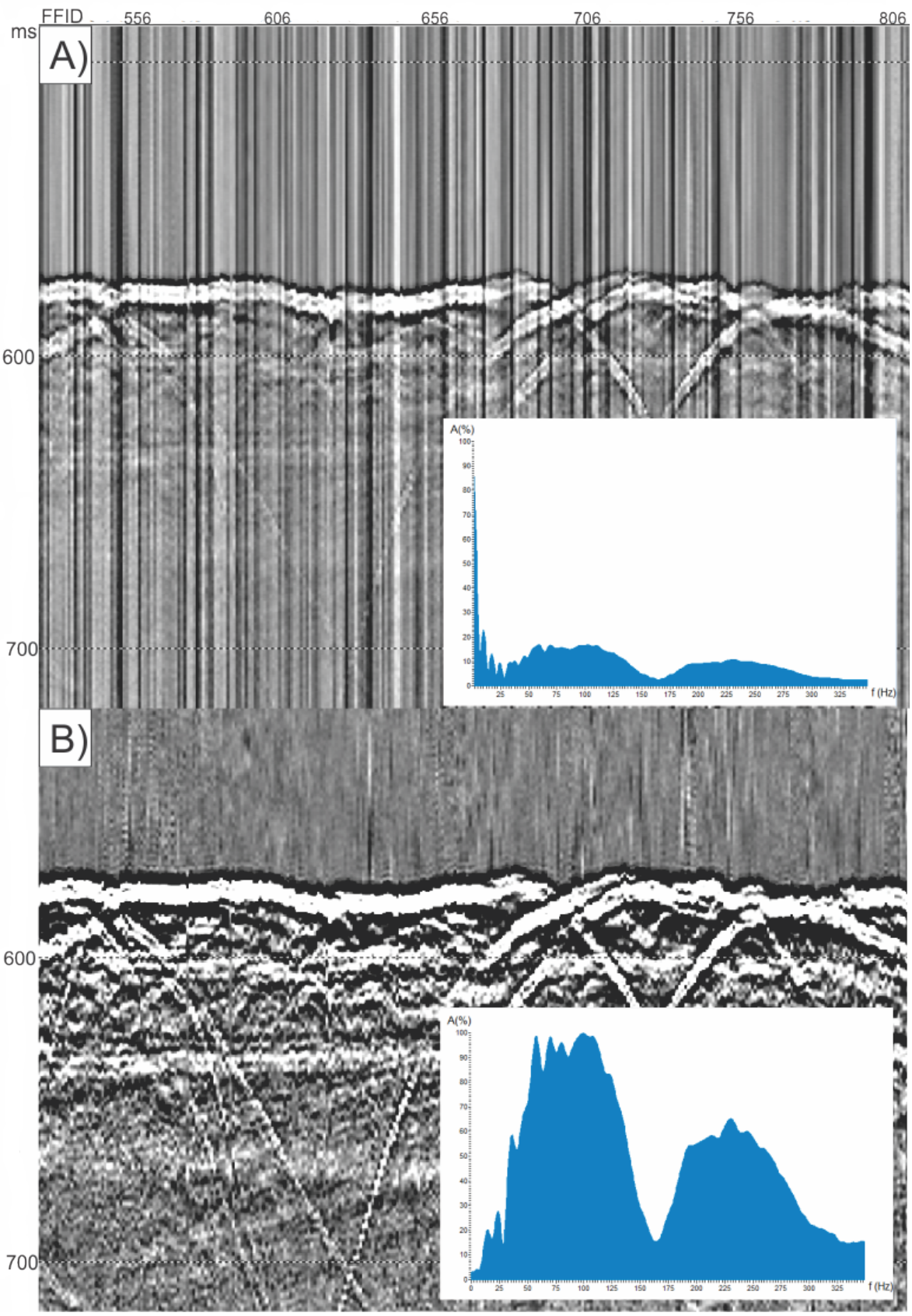

Figure 33. A) Screen display of a section of Line 1 raw data showing the average amplitude spectrum of the area around the seabed. B) The same section of Line 1 after applying an Ormsby bandpass filter.

3.2.3 DeGhosting

Ghosts are short-path multiples as explained in Chapter 3.2.1, created at either the source or receiver, or both (Figure 34). In Figure 33 B a notch is seen in the frequency spectrum, this is a consequence of the Ghost, most likely a source Ghost. When the acoustic wave travels from the source, some of the energy may travel up and reflect down off the air/water contact creating a Ghost of the direct wave. The ghost will then arrive at the hydrophones slightly later than the direct wave appearing as a horizon slightly below the main reflector. The depth difference will depend on the towing depth of both the source and the hydrophones (receivers). A deeper towing depth will result in a longer travel distance for the wave increasing the depth of the reflector. A negative interference between the source Ghost and the primary reflection will occur when the source depth is equal to half the dominant signal wavelength (Geokompendium, 2009).

$d = \frac{1}{2}\lambda$ Which will happen for frequencies:

$f = \frac{V}{\lambda} = \frac{V}{2d}$ hence when λ = 2d

When d = depth, λ = wavelength, and V = velocity.

The result is that the towing depth of the source and receivers will limit the resolution of the seismic data.

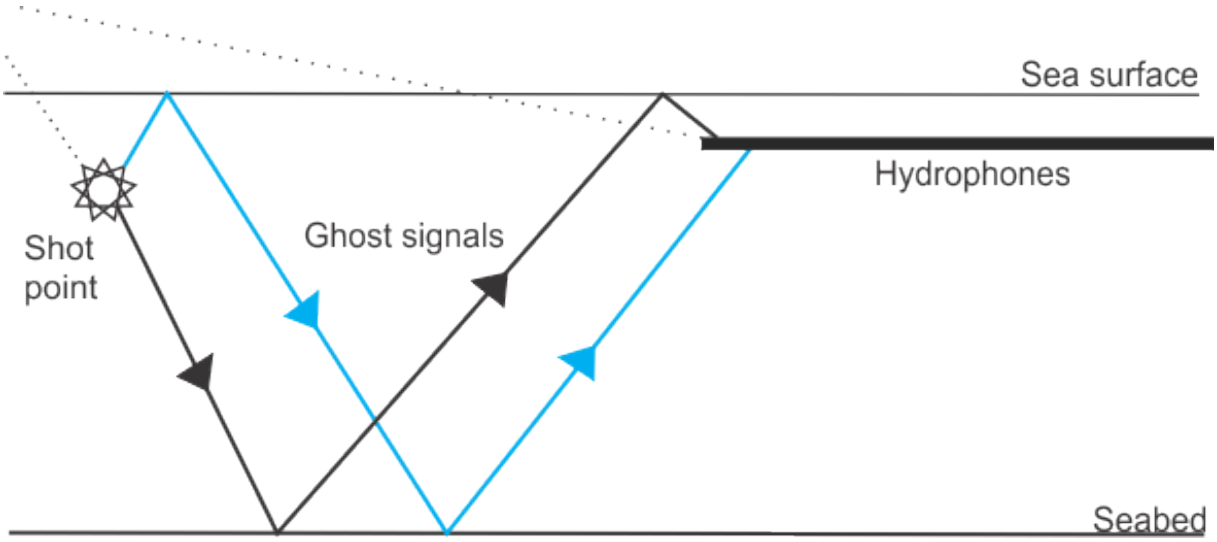

Figure 34. Sketch illustrating how the Ghost signals have a longer ray path than the primary signal since they reflect off the air / water contact before reaching the hydrophones.

DeGhosting removes the short-path multiple associated with the upwards travelling source reflection (Keary, 2002). In RadExPro, a DeGhosting module is used to suppress the Ghost waves in single-channel data. The algorithm implemented in the module is based on the Ghost wave model, which is created from the data itself by statically shifting the original trace by a specified time. The filter searches for similar reflections present in the data and the Ghost wave model, and then minimizes the root mean square amplitudes in the resulting field (RadExPro manual, 2014). The algorithm will work efficiently to a certain degree with an approximate Ghost model. However, the closer the Ghost wave model is to the actually observed Ghost waves, the better it will subtract.

The best way to get the model close to the real Ghost is by manually adjusting the module values, while visually checking the results on the seismic profile for the channel in question. The best result would be achieved with a minimum source-receiver distance, because a zero offset model is most accurate. In the case of this data, the rough weather conditions caused a variation in the offset, resulting in the module working less efficiently. The DeGhosting module was used on a single channel, adjusted, and then added to the remaining channels on the line. This was then repeated for each line separately before stacking (Figure 35).

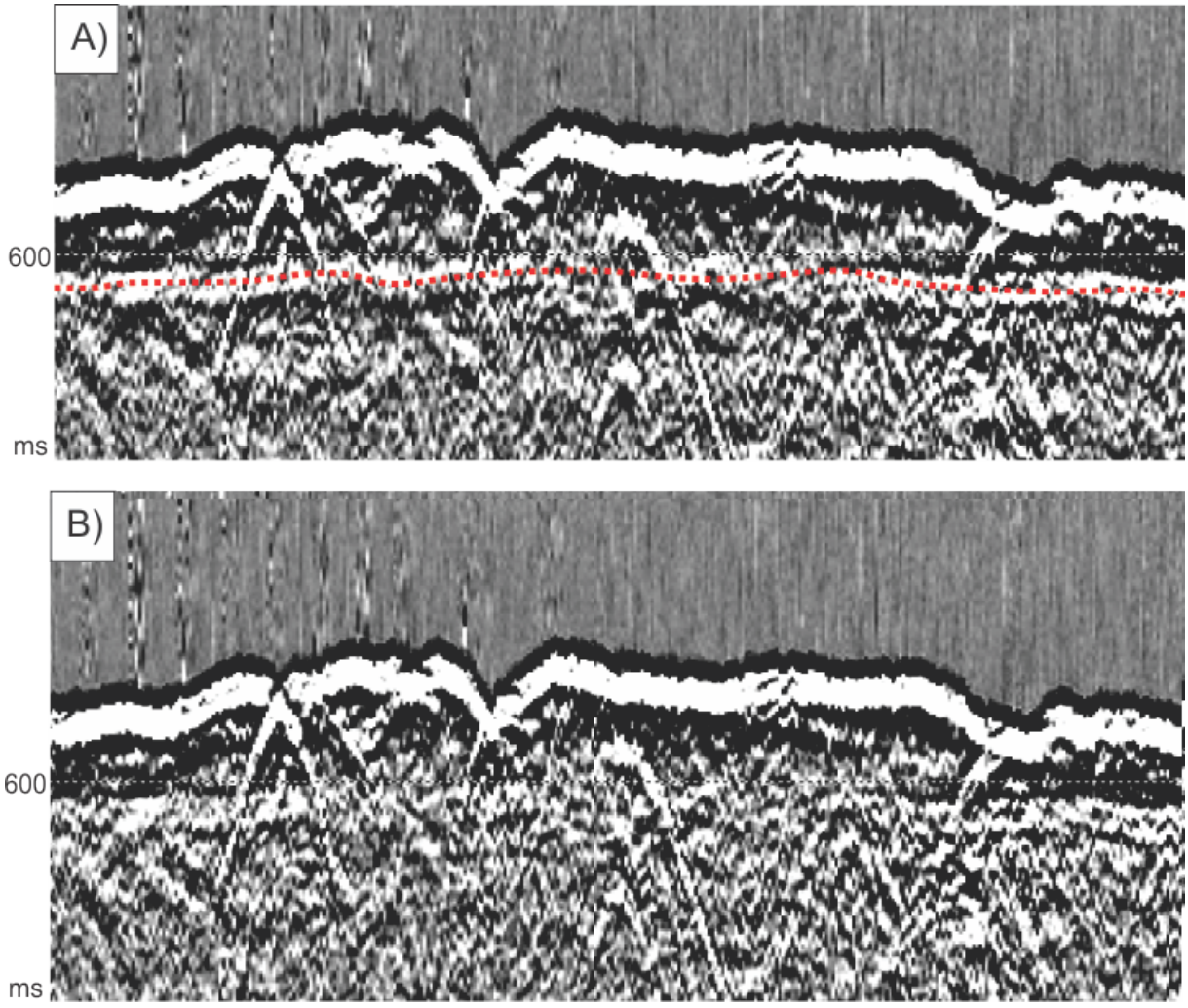

Figure 35. A) Showing Line 1 channel 100 with a red line highlighting the ghost signal B) showing the line after the DeGhosting process. The results vary along the line but an overall improvement is achieved.

3.2.4 Tide Import

The tide will create a variation in the depth of the survey, even though small, this may be corrected for by adding the variations to the data. Tide data was added to the dataset after stacking, instead of each individual line separately in order to save time during processing. The tide data used for the static correction was collected in Hammerfest, since this was the nearest location to the cruise with available tide data. The tide data was gathered from a table where the water level information is stored (www.sehavniva.no) (Figure 36). The Tides Import module in RadExPro imports static corrections for tides into trace headers of a dataset (RadExPro manual, 2014).

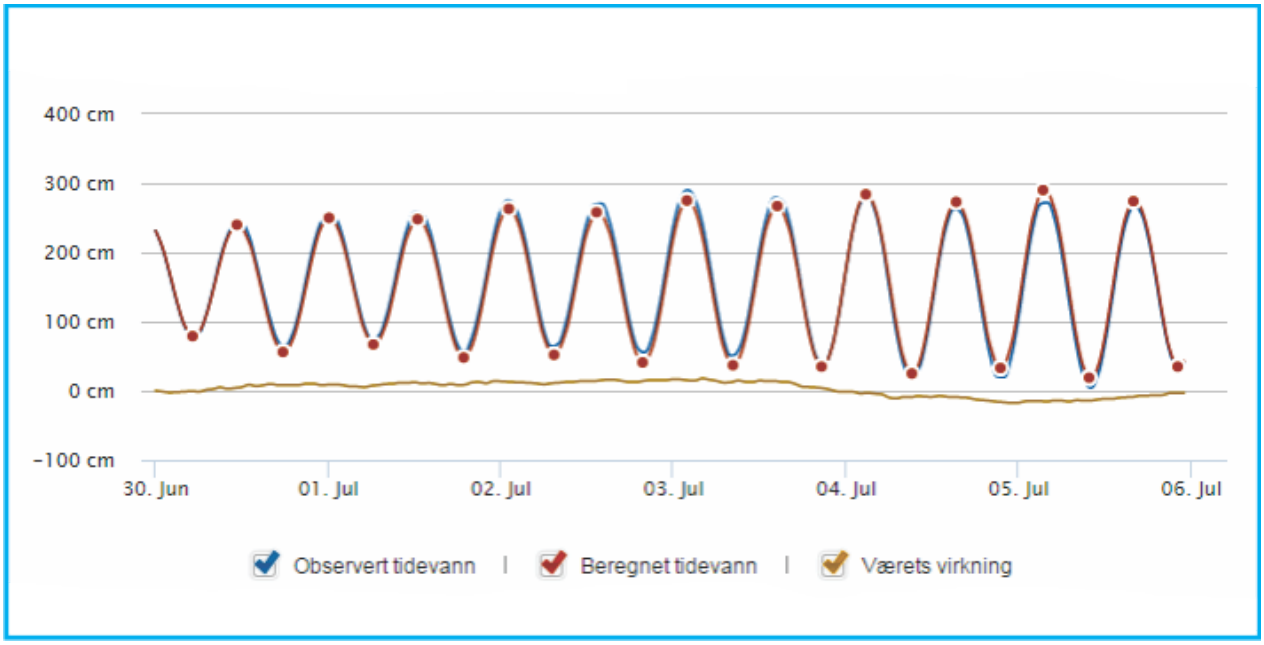

Figure 36. Tide date from Hammerfest showing the variations in the tide for the time of the survey. Modified from sehavniva.no

The tide fluctuations are added to a specific line matching the time and date together. The tide data improves the velocity analysis and the quality of the stacked data. The tides are represented as the difference between the first line and following lines in centimeters. Since the shooting interval is much shorter than the tide data collection, a linear interpolation is applied when the static corrections are loaded.

3.2.5 Spherical divergence correction

Spherical divergence is one of the factors which reduces the amplitude, or causes loss of seismic energy with depth. The seismic wave is represented as a ray path as a mathematical aid to visualize the wave front, as it is always perpendicular to the wave front, indicating where the energy is assumed to travel (Geokompendium, 2009). The energy is however, traveling spherically away from the source point and not in a ray and the spherical divergence represents the effect that the energy of a seismic wave is spread over its expanding wave front. The amplitude decreases proportionally with the increase of the radius of the wave front as it propagates through the earth. The effects of the spherical

divergence on amplitudes is approximated by the inverse square of the distance, which for a constant velocity is the inverse square of time (Henry, 2004).

To attenuate for this we use the amplitude correction module. This module applies a gain function variable in time to the traces. Each sample of the trace is then multiplied by the corresponding time and by a constant coefficient (RadExPro manual, 2014).

3.2.6 Static subtraction and applied fractional statics

Static subtraction involves removing travel time artifacts related to the positioning of the source and receive. Differences in the travel time to the same reflector because of distance differences from the source and receivers must be removed. To achieve this the relative elevation for each shot and the receivers must be known (AAPG wiki, 2014). The velocity used for this is the average water velocity 1500 m/s.

For these static corrections, we use the module “Apply Statics”. This module is used to apply static corrections, which are added manually, read from the database or from a trace header field. The static corrections are expressed in milliseconds. Negative values reduce time, which moves the data upwards in the seismic section. Positive values add time and moves the data down (RadExPro manual, 2014). For my data the previously loaded tide data was used to create a new header STAT1 which was used as the header for the static correction. The stat1 is given by:

$$stat1=-(([tot\_stat]/150)*2000/1500)$$

Where tot_stat is the Tide data.

3.2.7 Deconvolution

Convolution is a mathematical definition of how waveform changes shape when passing through a filter. This can be illustrated by how a seismic pulse from an air gun is filtered by effects in both the ground and the recording system, so that the filtered output differs significantly from the initial seismic pulse (Keary, 2002). The effect of convolution is in general the lengthening of the seismic pulse by progressive absorption of higher frequencies. This will lead to degradation of deeper interfaces since they become concealed by shallower interfaces.

The effect of a filter is given as a convolution operation where y(t) is the filtered output, g(t) is the is the input signal, and f(t) is the convolution operator which in our case is the sediment package the signal travels through (Keary, 2002):

$$y(t) = g(t) * f(t)$$

Deconvolution is the process that counters the convolution effect on the signal. This can be represented by the function:

$$g(t) = y(t) * f'(t)$$

Where y(t) and f(t) are known, and f'(t) is the function that must be convolved with y(t) to recover g(t). We can substitute y(t) with the previous formula giving us:

$$g(t) = g(t) * f(t) * f'(t)$$

We can also replace g(t) with:

$$g(t) = g(t) * \delta(t)$$

Where δ(t) is a spike function which combined with the previous functions give us:

$$\delta(t) = f'(t) * f(t)$$

Thereby if f(t) is known, f'(t) can be derived to recover the input signal g(t), where the f'(t) function is the deconvolution operator (Keary, 2002). Deconvolution is used to improve the seismic output through the removal of additional filters added to the signal wave during its passage through the ground. To do this we use the F-X Predictive Filtering module.

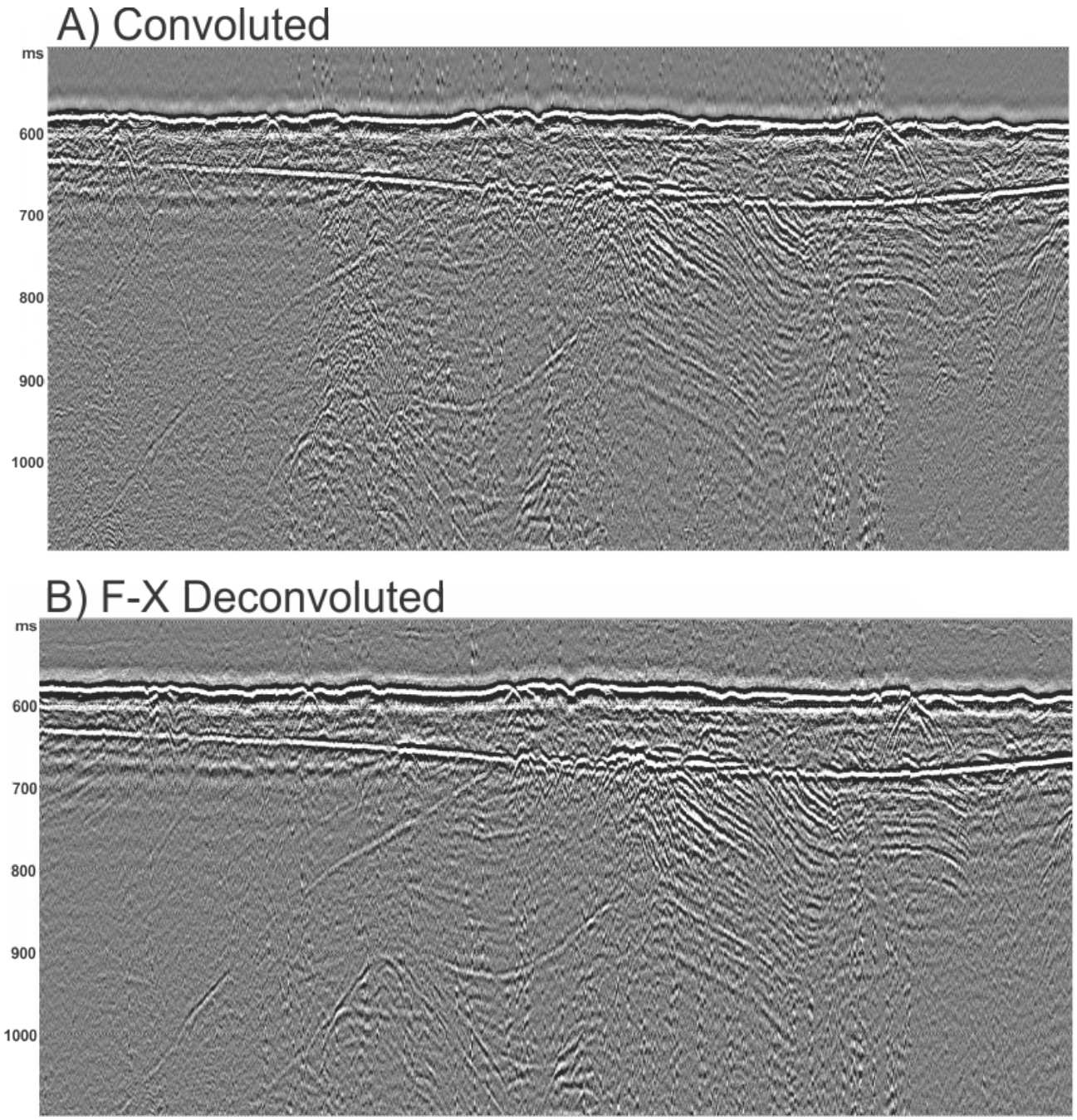

Figure 37. Figure showing how the F-X deconvolution process improves the deeper interfaces of seismic inline 100. A) showing a section of inline 100 before the process of deconvolution and B) showing the same section after the processing where we can see deeper interfaces more clearly and with less noise.

F-X Deconvolution, or F-X Predicted Filtering is one of the most common techniques in seismic processing to attenuate noise (Sanchis, 2010). It is used to suppress random noise on both trace ensembles and stacked sections, for this dataset it was used on a stacked section. This gives a much better view of the deeper interfaces by shortening the pulse length and improving the vertical resolution, as we can see in Figure 37 B.

3.3 Normal move out (NMO) and Stacking

3.3.1 Normal move out

Before stacking the data, normal move out corrections must be applied to the CDP traces. The NMO (Normal Move Out) correction is a vertical time-shift for the reflected energy recorded at a certain offset from the source (Geokompendium, 2009).

The velocity, and thereby the depth, of a layer can be calculated using a number of receivers and offset to one or both sides of the shot point. For the shortest reflected ray path a formula using the offset X and the travel time T from the shot point, and the unknown values V and h for velocity and depth, can be created (Keary, 2002):

$$t = \frac{\sqrt{(x^2 + 4h^2)}}{v}$$

The rays that reach the receivers have traveled progressively further, using more time from the shot point, creating the curve (hyperbola) shown in Figure 38. The additional time (t) depends on the velocity (v) and the thickness of the layer. To calculate this we start with the vertical two-way travel time (TWT), t_0, which is twice the depth divided by the seismic velocity $2h_1/v_1$. To reach the receiver at offset X the formula becomes $2SA/v_1$. By using Pythagoras's theorem and squaring both sides, we end up with the formula (Mussett, 2000):

$$t^2 = (t_0 + \Delta t)^2 = t_0^2 + \frac{x^2}{v_1^2}$$

If the offsets are small compared to the thickness of the layer, which usually is the case, the time is given as:

$$\Delta t = t - t_0 \approx \frac{x^2}{2v_1^2 t_0}$$

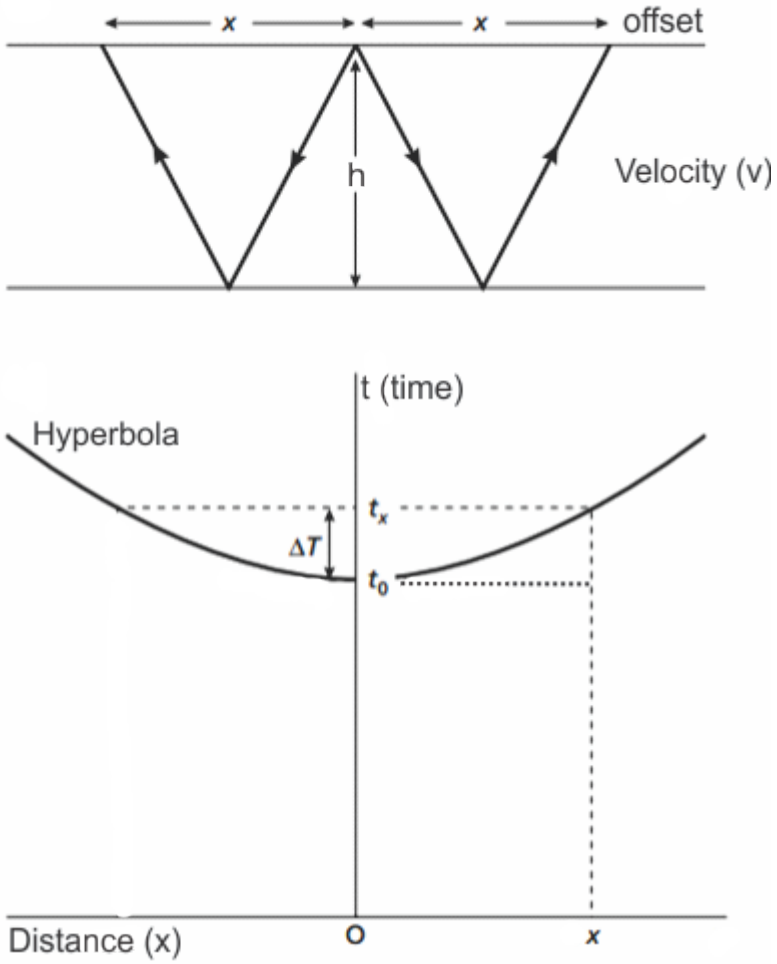

Figure 38. Illustration of the principle of normal move out. Edited from Musset, 2000 and Keary, 2002.

In short, the NMO is the difference between the two-way time at a given offset and the two-way zero-offset time (Geokompendium, 2009). The NMO has to be corrected before stacking to increase the CMP gather strength (Figure 39 and 40).

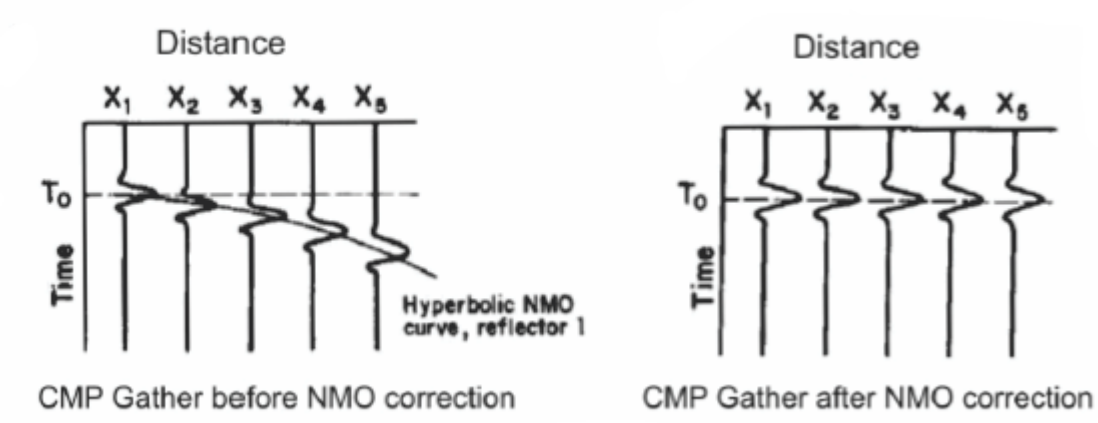

Figure 39. Figure showing a CMP Gather before and after NMO correction and how the hyperbolic NMO curve is straightened. Modified from Geokompendium, 2009.

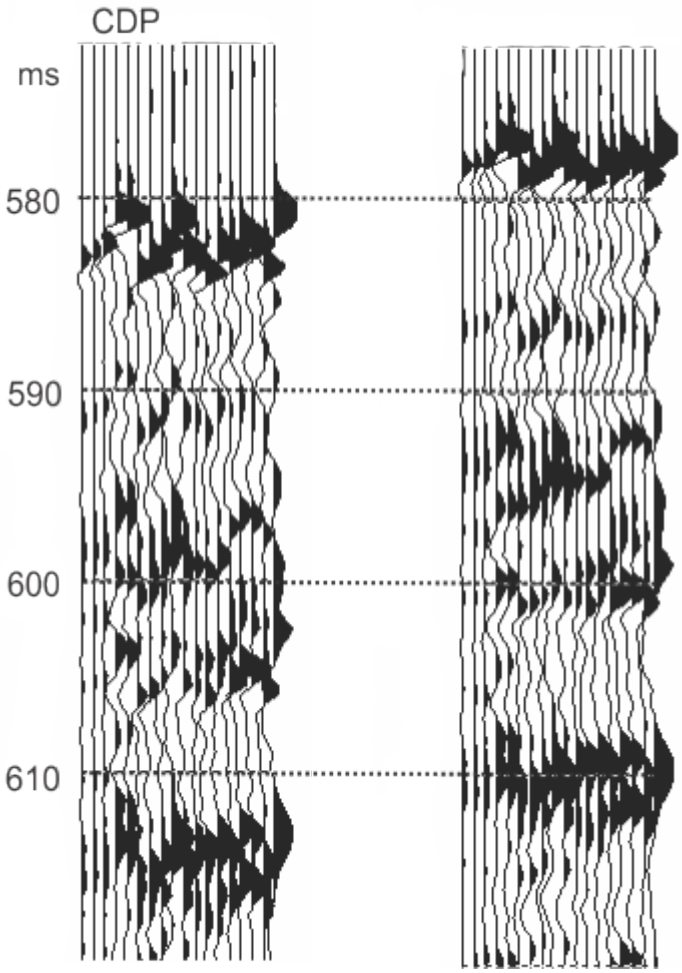

Figure 40. CDP traces shown in wiggle display to show how the CDP traces are aligned before stacking. Modified from screen shot RadExPro.

3.3.2 Stacking

The seismic reflectors are often weak, especially the deeper reflections, because of the energy being spread over large areas. It is often difficult to distinguish reflectors because of the surrounding noise. By stacking signals we are able to make the reflections stronger and improve the signal to noise ratio. Figure 41 shows multiple CDP gathers stacked to four traces. This shows how a stronger more consistent signal is achieved through stacking.

Before stacking, the traces have to be corrected for their move out, as seen in Chapter 3.3.1 where we migrate the hyperbolas into straight lines. If the NMO correction is done correctly the arrival of the various traces will line up so they can be added together to create a stronger signal (Mussett, 2000). To stack the data I used the Ensemble Stack module in RadExPro. In this module, we can stack all traces within each ensemble of the flow into one trace (RadExPro manual, 2014). An ensemble is a group of traces with the same value as the primary sorting key in the trace input, which in this case is the CDP. During this process, sample values are being averaged, and samples with zero values are considered results of muting and not used in the stacking.

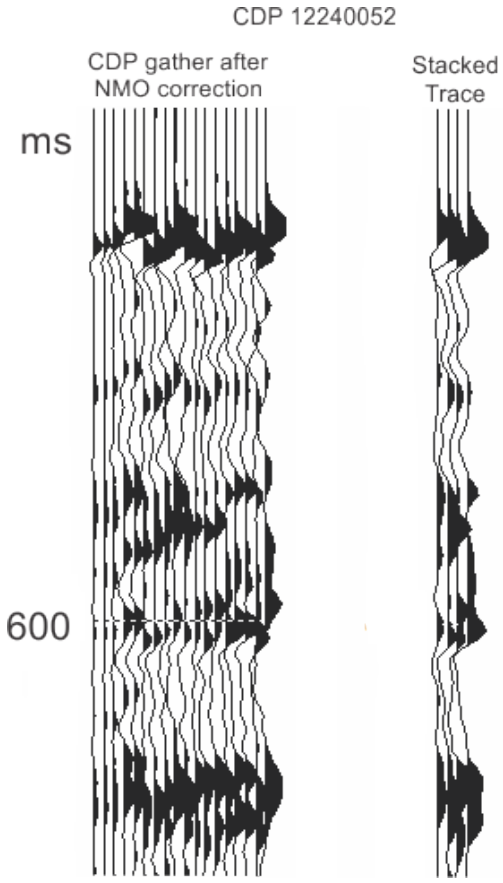

Figure 41. Image of multiple CMP gathers after NMO corrections, and again after Stacking.

3.4 Migration

The main goal of seismic data processing is to image the Earth's subsurface, by creating a picture of the structures using seismic waves. As seen in previous chapters we use deconvolution to sharpen the deeper reflections and stacking to enhance the signal to noise ratio. However, until the migration step the seismic data has only represented recorded traces of echoes from the subsurface (AAPG wiki, 2014). Migration can then simply be defined as the process where geological events are geometrically relocated to the location where the event occurred in the subsurface, instead of the location where it was recorded (Sanchis, 2010). Through migration the signals are transformed into features in their proper position both laterally and vertically.

3.4.1 Interpolation

Before the migration the data needs to be prepared by interpolation. The migration process requires the traces to be located within a rectangular grid. The Profile Interpolation module (Figure 42) is used here to interpolate the data into a regular grid, a process similar to the 3D CDP binning done earlier. A cut of the dataset is done to remove the messy outer edges of the survey, which contain the turning points of the vessel. For my dataset a cut section containing inline 50 through 190, and cross lines 300 through 2600 was used. The same parameters used for the CDP binning is used for the interpolation with a gridding of 6.25 x 6.25. The interpolation will change the inline and cross line headers to correspond with the X-axis and Y-axis of the interpolated grid.

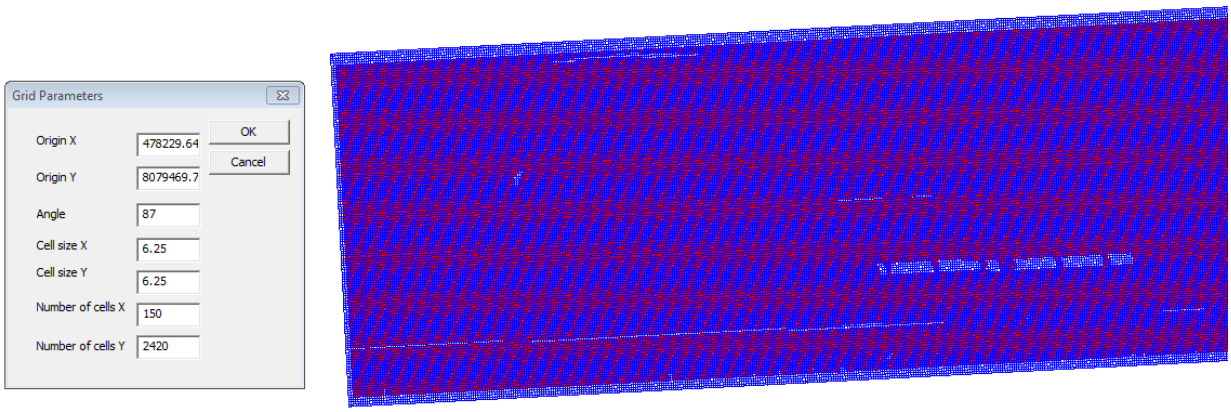

Figure 42. Screen shot of RadExPro Profile Interpolation gridding process. Showing blue interpolation grid with a 6.25 x 6.25 spacing over the data points shown in red.

3.4.2 3D STOLT Migration

When looking over the NMO-corrected and stacked dataset we can see several anticlinal features. These are artifacts created by dipping layers. For horizontal reflectors, the receivers will record data at a midpoint between the source and the receiver. For a dipping reflector, the data point is not midway between the source and receiver. The offset of the position increases with the angle of the dip. The effect of this is that the reflector appears to be shallower and with a lower gradient to the dip then the actual reflector. If the reflector is curved, the distortion is more complex. On unmigrated data sections, the reflective strength decreases over syncline structures due to a focusing effect. As we see in Figure 43, as the shot point moves from 1-10 the shortest travel path for the ray shifts from one side to the other of the synclinal (Mussett, 2000). The arrival times for the position creates a bow tie feature in the section.

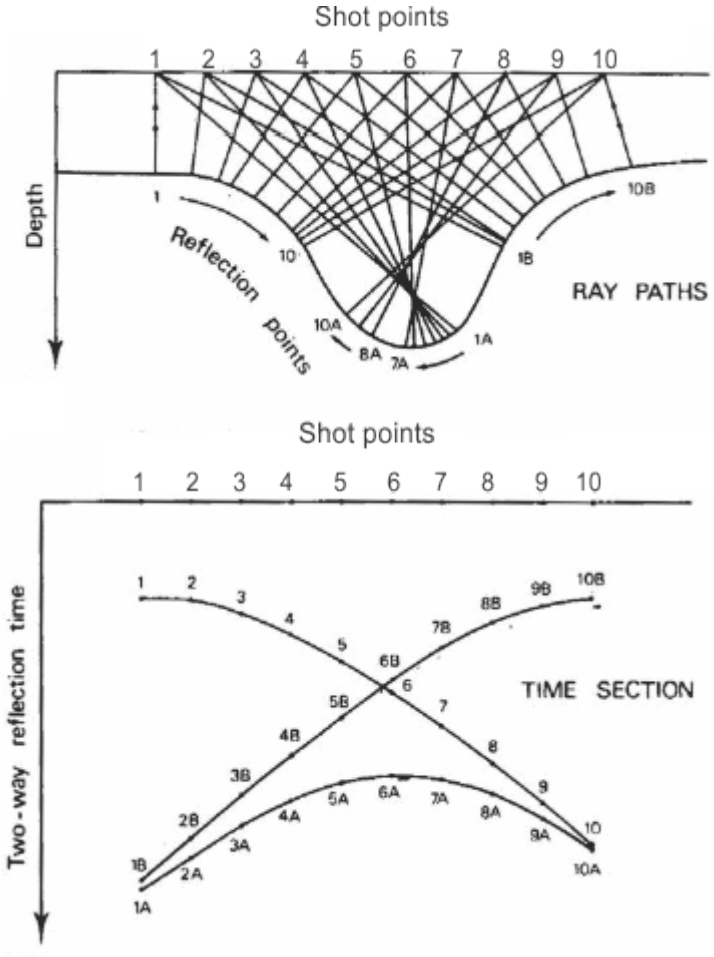

Figure 43. The bow-tie effect shown as a geological model of a reflector with a larger curvature than the wave front, and a schematic seismic section showing the reflectors resembling a bow tie. Modified from Badley 1985, Geokompendium 2009.

To correct for the dip effects seen in the seismic data the migration process is used. Migration steepens the dip and shortens the lengths of the reflection, collapsing the diffraction curves to the apex of the diffraction hyperbolas. After migration anticlines become narrower and synclines become broader as the reflection points are moved to their true location. Migration may also improve the resolution of the seismic by collapsing diffraction patterns and focusing the energy spread over the Fresnel zone (Keary, 2002).

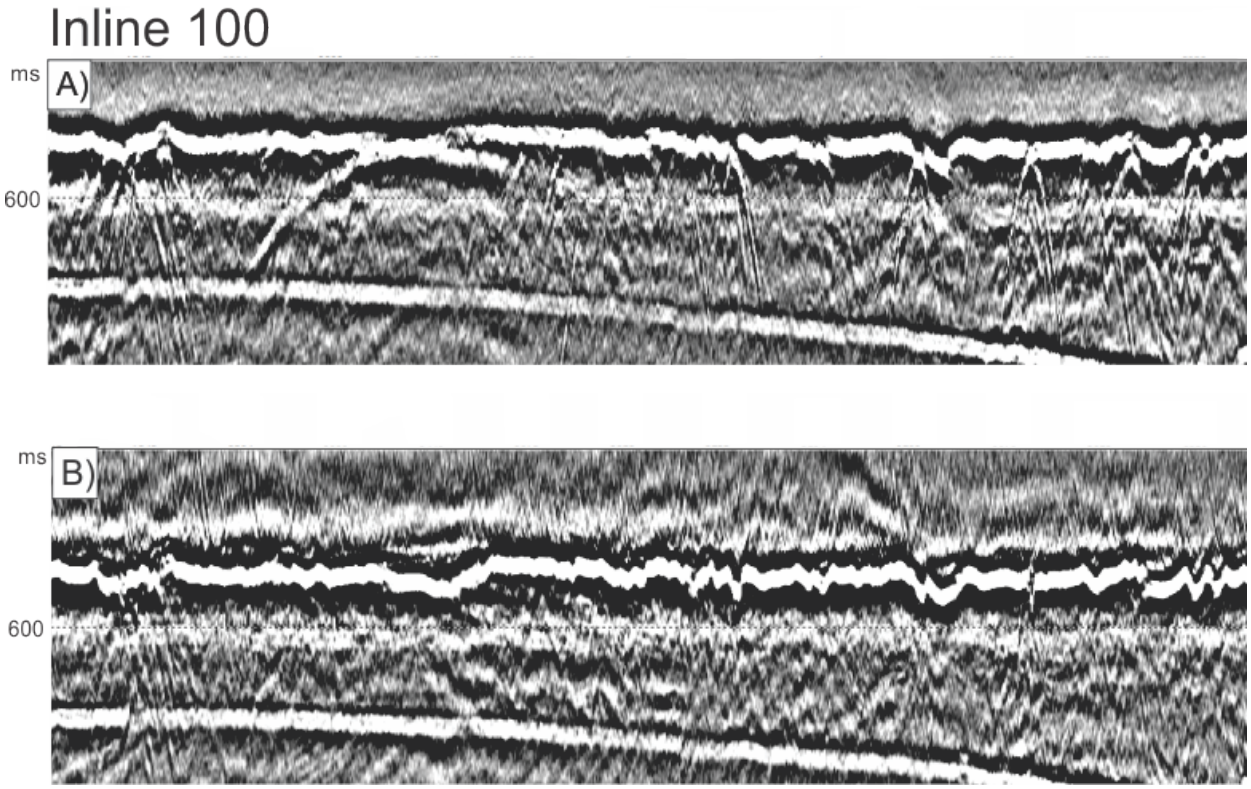

Figure 44. Section of Inline 100 showing A) before migration and B) after STOLT 3D migration.

This is done using the STOLT3D module, which performs a 3D Stolt migration of the seismic gathers acquired at zero source-receiver distance (RadExPro manual, 2014). The traces must be located in a rectangular grid, which is why the interpolation process was done previously. The input data is sorted after the Inline and Crossline numbers assigned during the interpolation. The areas that do not contain any data will be zero-padded. Figure 44 shows a section of Inline 100 before and after STOLT 3D migration. For the 3D STOLT migration a velocity of 1.5 m/ms, and a grid spacing of 6.25 m x 6.25 m.

3.5 Export

After importing the raw data into RadExPro, assigning the geometry, filtering the data to improve the signal to noise ratio, and stacking and migrating it, we can export it so that we can start interpreting it. The processing is not necessarily completed, as there are always further improvements one can make. However, this is a good point to look over the results in order to determine the quality, and further course of action. The data is exported using a SEG-Y export module. The SEG-Y file is then available for visualization in an interpretation program.

4 Results

The interpretations and observations from the 3D-seismic dataset “Bjornoyrenna” are presented in this chapter. The focus of the interpretations is the development of shallow gas accumulations, such as flat spots and their relationship to the structural development of this area. The 3D seismic will also allow mapping of the gas trap structures both vertically and horizontally. Using the 3D-seismic cube created through processing, a closer look at features that can give information about the migration, trapping and possible leakage of gas within the Bear Island Trough area, may be mapped. In addition, 2D lines are used in order to connect the 3D cube to the regional stratigraphy. Well data is used to correlate the structural features with stratigraphic units in order to date the features.

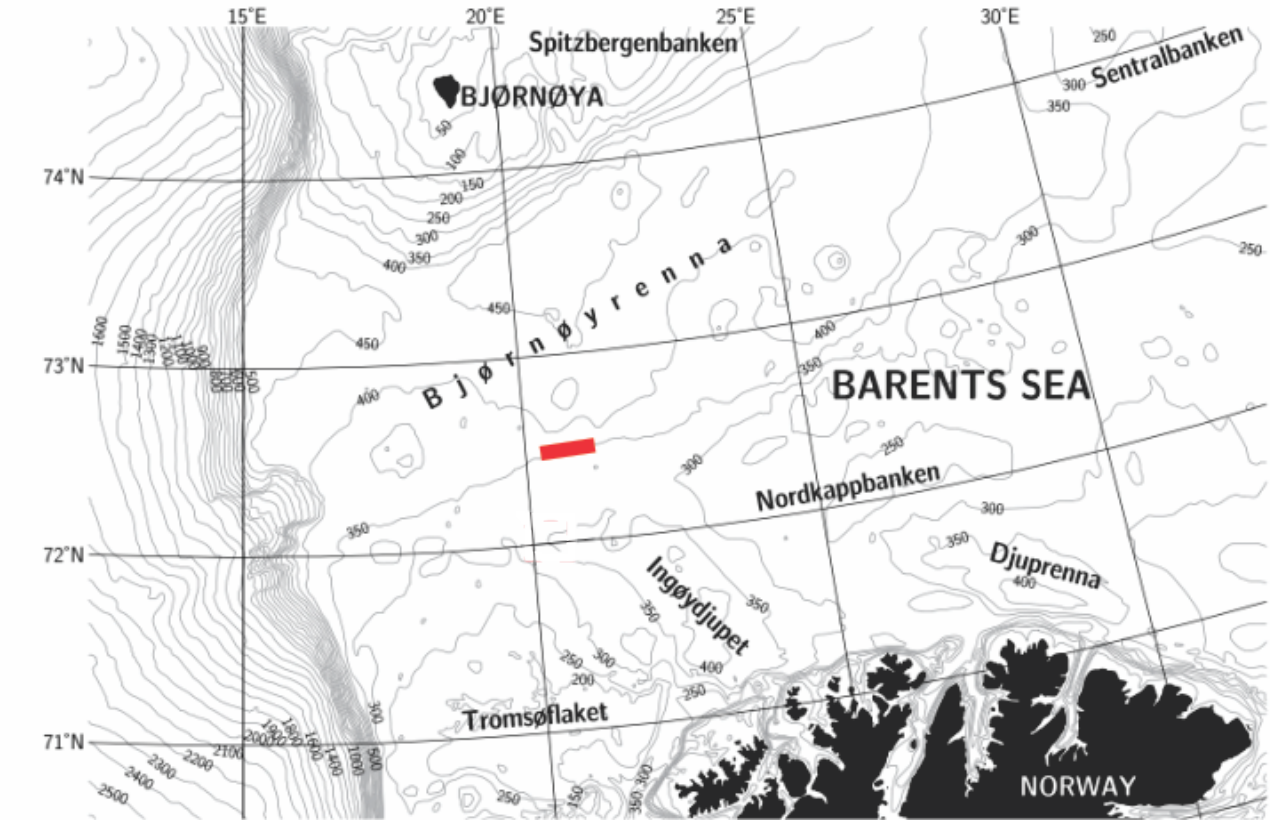

Figure 45. Map showing the approximate location of 3D cube within the red box in the southwestern Barents Sea. Modified from Pau, 2014.

4.1 Stratigraphic and structural interpretation

The geological setting of this area as mentioned previously (Chapter 1) has been heavily effected by glacigenic activity. Evidence of this can be seen on the seabed and Upper Regional Unconformity (URU). In this chapter, features found on the seabed are described, followed by mapping of the stratigraphy, major beds and horizons within the dataset.

4.1.1 Seabed features

The seabed shows several geological features (Figure 46). Most prominent are the large curved furrows with varying orientation. Within this dataset, the furrows show depths between 4 to 13 meters, lengths between 100 to 425 meters, and widths between 6 to 15 meters, which most likely continue outside this dataset. They generally have a linear to slightly curved shape with a few examples of sharp “U” shapes, and are abundant across the entire dataset. These features are interpreted as iceberg ploughmarks formed by wind and current driven icebergs scouring the seabed (Judd and Hovland, 2007). These were most likely created during the deep water glacier calving during the late Weichselian (19-15 cal ka BP) deglaciation phase (Winsborrow et al., 2010).

There are also lines which are parallel to the inline direction. These are survey footprints and not real geological features. They are caused by noise left after the processing and cover the entire seabed (Figure 46). The noise is created by variations in the streamer depth. The streamer depth is effected by the slack in the cross cable which is affected by the ship speed and currents. Waves during the survey due to changing weather conditions produce jittering along the profile due to the variations in gun depth (Petersen et al. 2010). Processing attenuates some of this noise; however, weather conditions were particular bad during this survey resulting in the visible noise.

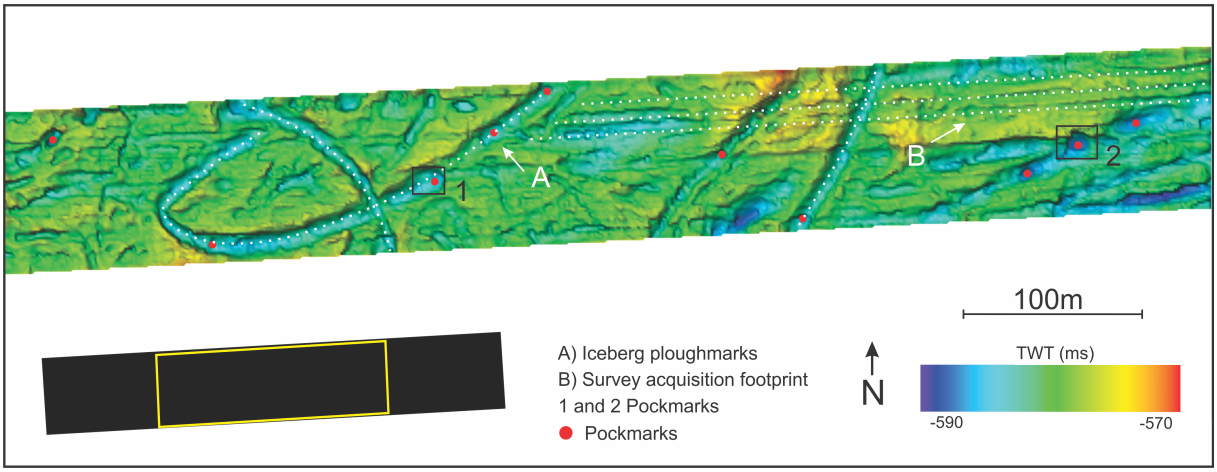

Figure 46. Features seen on the seabed, highlighting ploughmarks, survey footprints, and pockmarks. Close up of pockmarks 1 and 2 in Figure 46.

Several circular to sub circular depressions with varying size are seen on the seabed. Most are located within ploughmarks as either single depressions or chains of depressions. Figure 47 shows a couple of examples of pockmarks within ploughmarks in detail. Their size varies from a few meters in diameter to about 13 meters within this dataset, and they are interpreted as pockmarks. Pockmarks usually have steep flanks and relatively flat bottoms and are a result of fluid flow through the seabed, usually seeping hydrocarbons such as methane but also other fluids such as groundwater (Judd and Hovland, 2007). Some of the depressions are seen located above high amplitude anomalies (described in a later section) as we can see in Figure 47 1. Pockmarks are divided into groups based on the classification of pockmarks (Hovland et al., 2002). Two of these classifications are seen within this dataset: Unit pockmarks which are small depressions usually 1 to 10 meters wide and up to 0.5 meters deep, and Normal pockmarks which are circular depressions usually from 10 meters and up in width and depths from 1 meter to 45 meters (Hovland et al., 2002).

In Figure 47, we see two examples of normal pockmarks with different sizes. The first one (Figure 47 1) has an average diameter of 10 meters and a depth of 3.75 meters with a water velocity of 1500 m/s. This depression is located above a high amplitude anomaly located at a depth of 75 m (86 ms TWT) below the seabed using a velocity of 1750 m/s. The depression has a U-form in the seismic section, with steep sides on the two sides correlating with the

boundary of the ploughmark and less steep more elongated sides in the NNE-SSW direction. Elongated pockmarks are a separate classification (Hovland et al., 2002) which have one axis that is longer than the others are, but are otherwise more or less the same as normal pockmarks.

The second pockmark (Figure 47 2) is larger than the first and located at a deeper part of the survey area. It is also located within a ploughmark. The diameter is 15 meters and it has a depth of 6.37 meters (V_P = 1500 m/s). This pockmark has a U-shape and relatively flat bottom in the seismic cross section common for pockmarks.

Several more potential pockmarks are observed within the survey area (Figure 46). The examples shown here reflect the general size and appearance of these features.

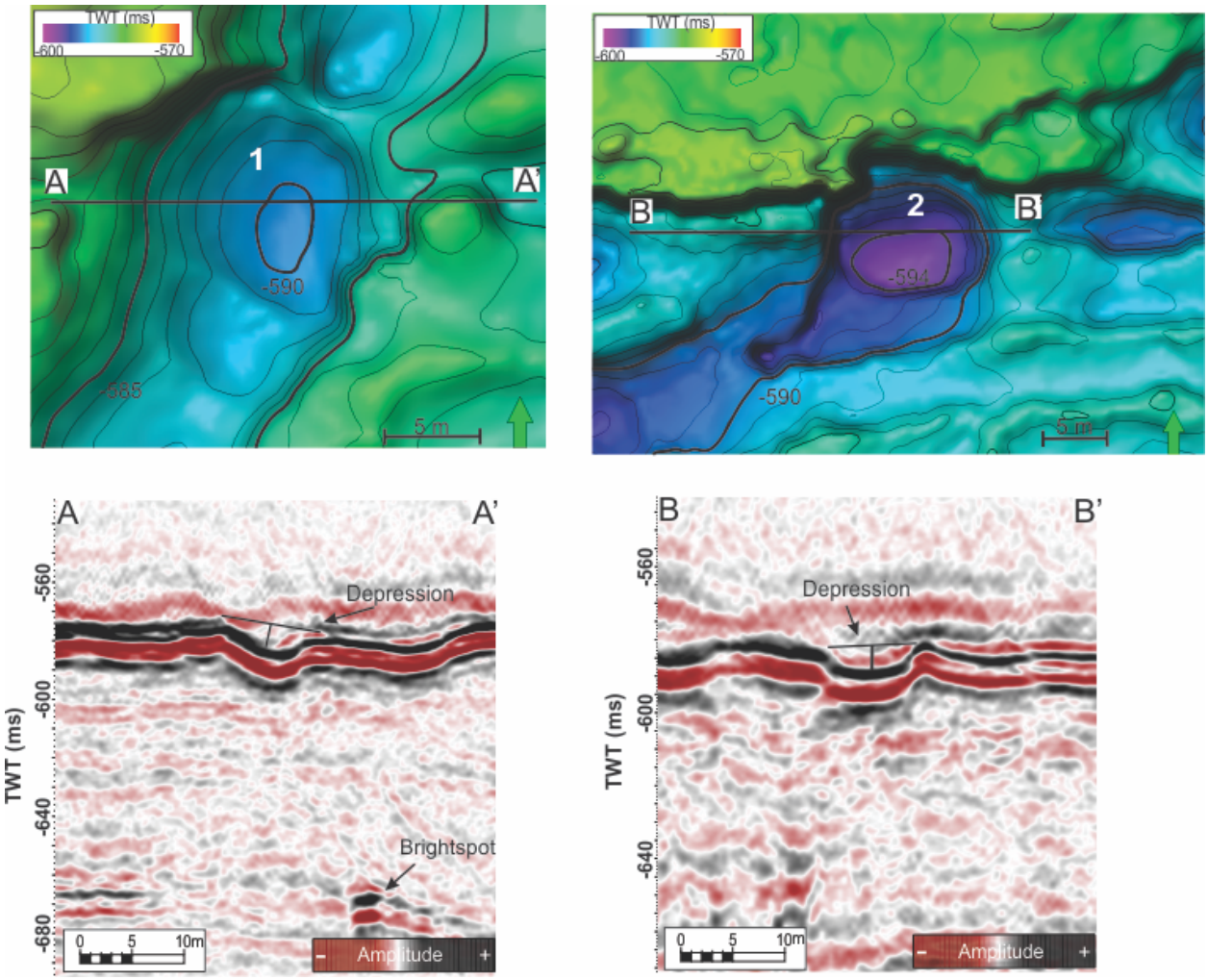

Figure 47. Figure showing two examples of depressions interpreted as pockmarks (1 and 2 as seen in Figure 42). The pockmarks are seen in a map view of the seabed surface. Below the pockmarks are shown in a seismic cross section indicating their depth and shape.

4.1.2 Stratigraphy

The stratigraphy of the dataset has been correlated by use of seismic 2D lines that intersect the 3D cube (Figure 48 and 49). Prominent reflectors within the 2D line LHSG89-211 have been stratigraphically correlated with the well 7219/9-1 (Figure 49). The well data was obtained from NPD's Petrobank and contains well tops from the Nordland Group to the Snadd Formation. Because of the shallow depth of the 3D cube, many of these formations are not seen within the dataset. Also because of the distance to the well many stratigraphical units are not possible to correlate across all the 2D lines LHSG89-211, LHSG89-212, LHSG89-225, and LHSG89-422 before reaching the dataset cube.

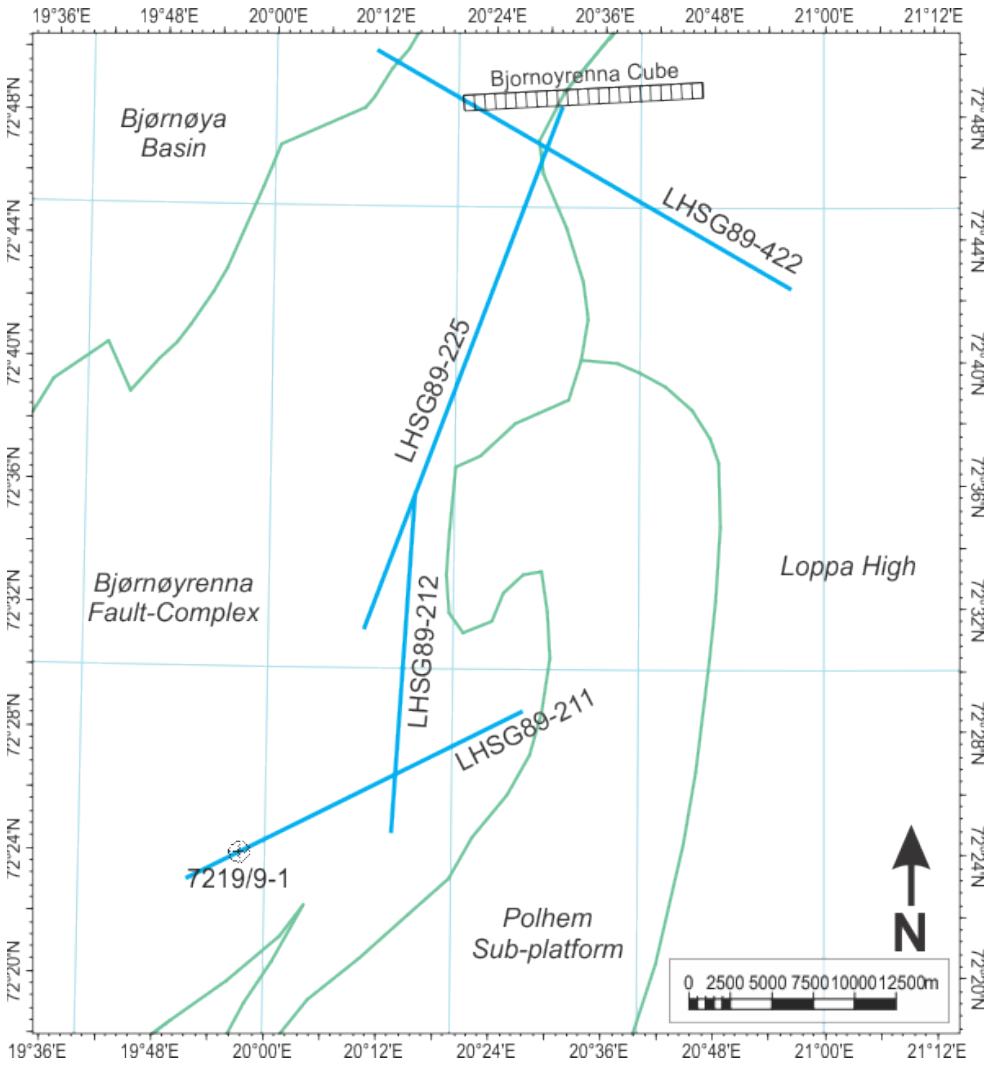

Figure 48. Overview map showing position of well 7219/9-1 and the seismic lines used to connect the well data to the seismic dataset. Well data from NPD fact pages. 3D view of lines seen in figure 48.

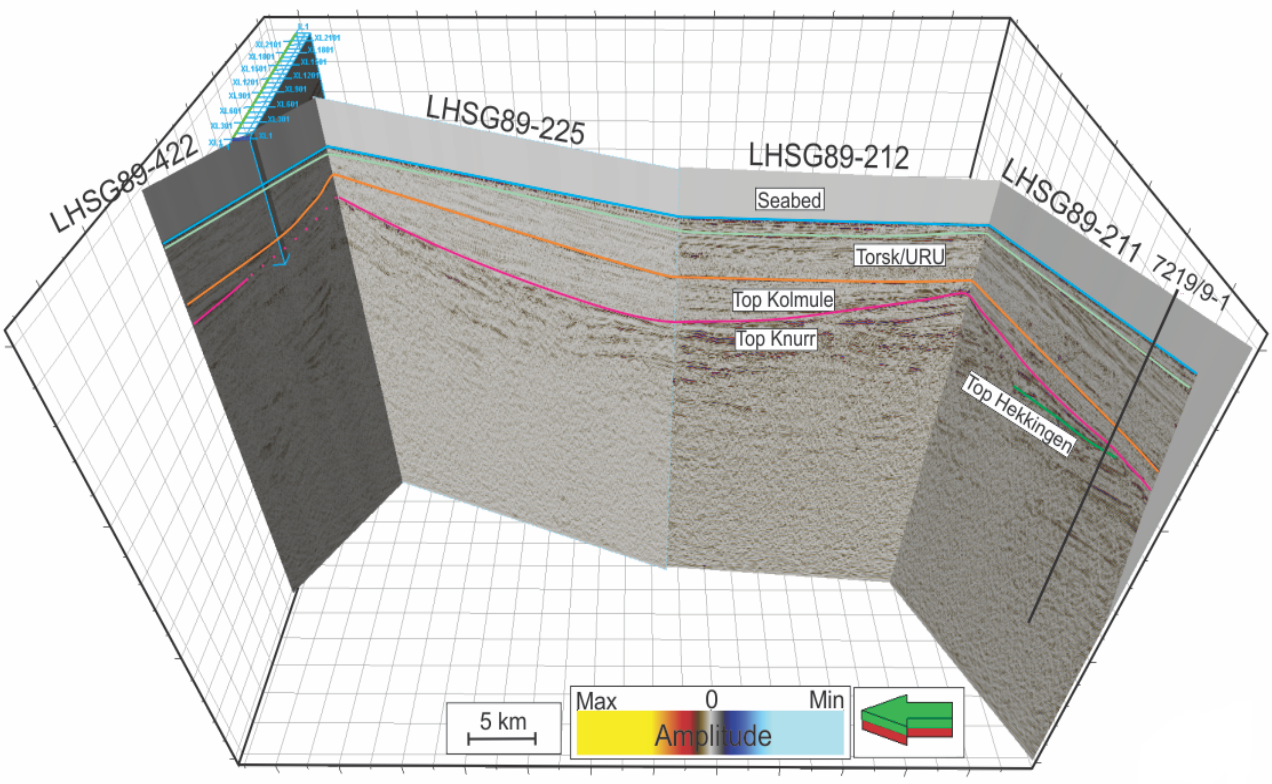

Figure 49. 3D view of seismic 2D lines used to correlate well 7219/9-1 to the dataset. Stratigraphic sequences shown as different colors from their observed location and traces to the dataset cube. Map view of this figure seen in Figure 47.

The Top Snadd formation is the deepest formation penetrated by the well and is located within the Triassic strata. However, this is not seen within the dataset due to its depth. The top of the Triassic strata is seen by the dashed white line (Figure 50). This is because it is located directly below the Jurassic strata but the transition from Jurassic to Triassic is not clear in the dataset and could be below the extent of the 3D cube depending on the thickness of the Jurassic strata.

The Top Hekkingen formation (Figure 49 and 50) represents the top of the Jurassic strata, and base Cretaceous unconformity. Within the Jurassic sediments, we see dipping layers towards the east within the fault block. The Hekkingen Formation is greatly influenced by the fault complex, and due to the location of the well not possible to trace to the eastern fault blocks in the dataset through the 2D lines.

The Top Knurr formation occurs within the Cretaceous strata above the Hekkingen Formation (Figure 49). The Reflectors are downlaping on to the Top Hekkingen Formation.

It is shaped as a wedge thinning away from the footwall, indicating sedimentation during the faulting.

Top Kolmule represents the top of the Cretaceous strata. It occurs as a tilted strong reflection below the Torsk formation terminating at the URU in the center of the dataset (Figure 50). Structural features within the Kolmule Formation are difficult to see because of the seismic quality.

The top of the Torsk Formation correlates with erosional surface of the URU (630 ms TWT) and extends out of the dataset in the western part of the dataset (Figure 50). Within the Torsk Formation, layers with a westward dip onlap the Top Kolmule surface.

The eastern fault blocks (Figure 50) are not interpreted because the structures are too uncertain. Glacial erosion, uncertainness of the throw of the faults and the distant location of the well makes interpreting these blocks difficult. Better quality seismic within the 3D dataset, as well as the 2D lines, could show stronger reflective layer aiding in tracing the formations along the faults. Well data located nearer the study area would also aid in determining the age of these structures.

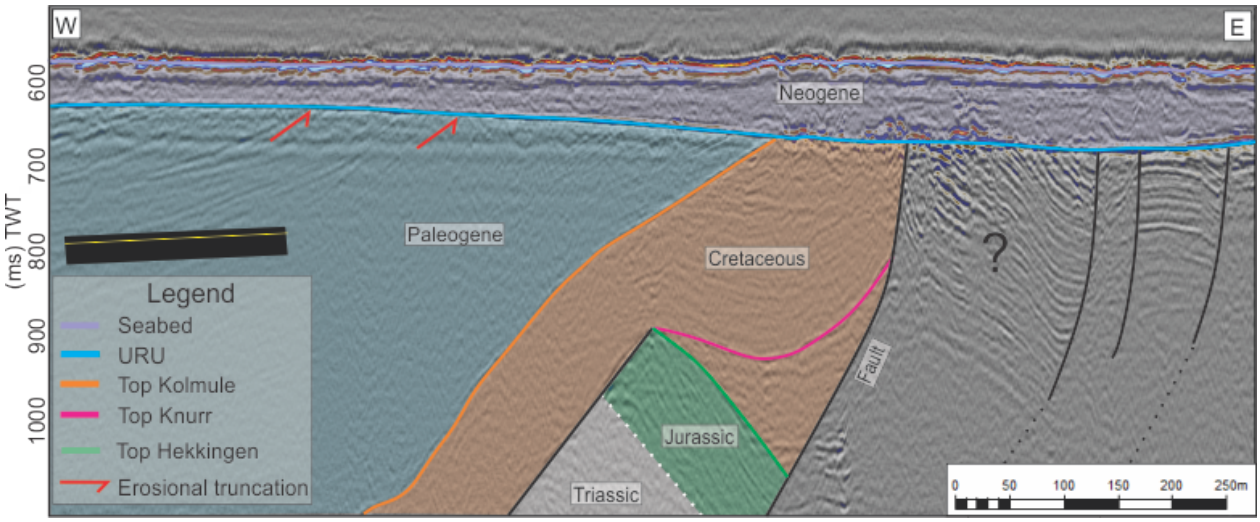

Figure 50. Seismic cross section of dataset showing different stratigraphic sequences from Hekkingen to Torsk. Yellow line shows location of seismic line. Eastern fault blocks not interpreted due to well location.

4.1.3 Upper Regional Unconformity

Below the seabed, the strongest horizon is the Upper Regional Unconformity, which separates the underlying sediments and overlying Neogene glacial deposits (Figure 51) (Andreassen et al., 2008). The URU covers most of the Barents Sea separating various sedimentary rocks from overlying sequences of glacigenic sediments. The thickness of the glacigenic sediments varies from 0 to 300 meters on the shelf, and up to 1000 meters at the shelf edge, assuming velocities of 2000 m/s (Vorren, 1991; Andreassen et al., 2008). The URU represents the erosional base for several glaciations on the continental shelf and varies in age across the Barents Sea. Using a constant velocity of 1750 m/s (Ostanin, 2013) for the sediments above the URU the thickness was calculated to be between 48 meters and 84 meters for my dataset. It is also useful in connecting the dataset to the well 7219/9-1, because it is a strong reflection seen across all the 2D lines. In Figure 51, we see a seismic cross section of inline 20 with the URU marked by a green horizon.

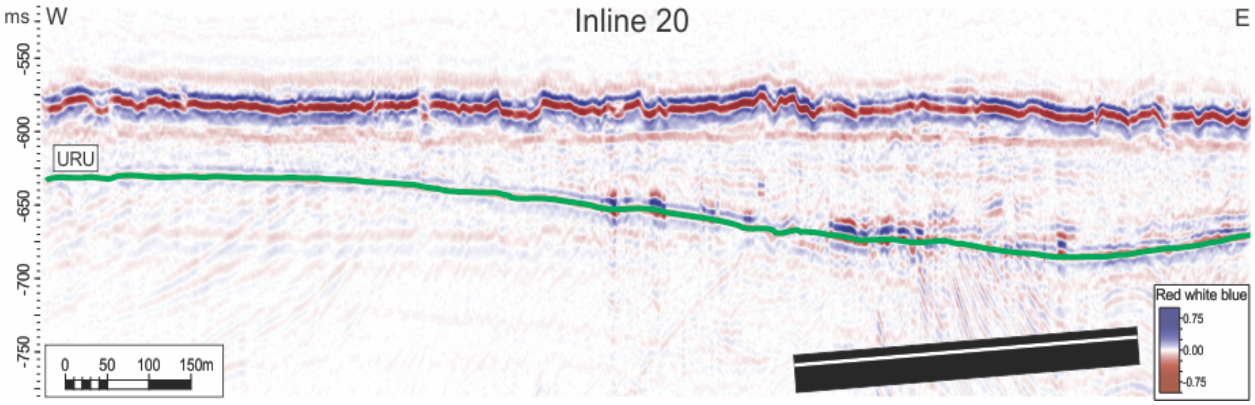

Figure 51. Seismic cross section showing inline 20. The Upper Regional Unconformity is indicated by a green horizon. Red white blue scale shows seismic amplitudes.

4.1.5 Faults

Two general types of faults are observed in this dataset; deep-seated larger-scale faults and shallower smaller scale faults (Figure 52). The larger part of these faults are seen in the eastern half of the dataset. The deeper-seated faults, which seem to extend beyond the depth of the dataset, can easily be located, but the shallower faults are more difficult to

trace due to the quality of the seismic data. The small-scale faults are located within the larger scale fault blocks.

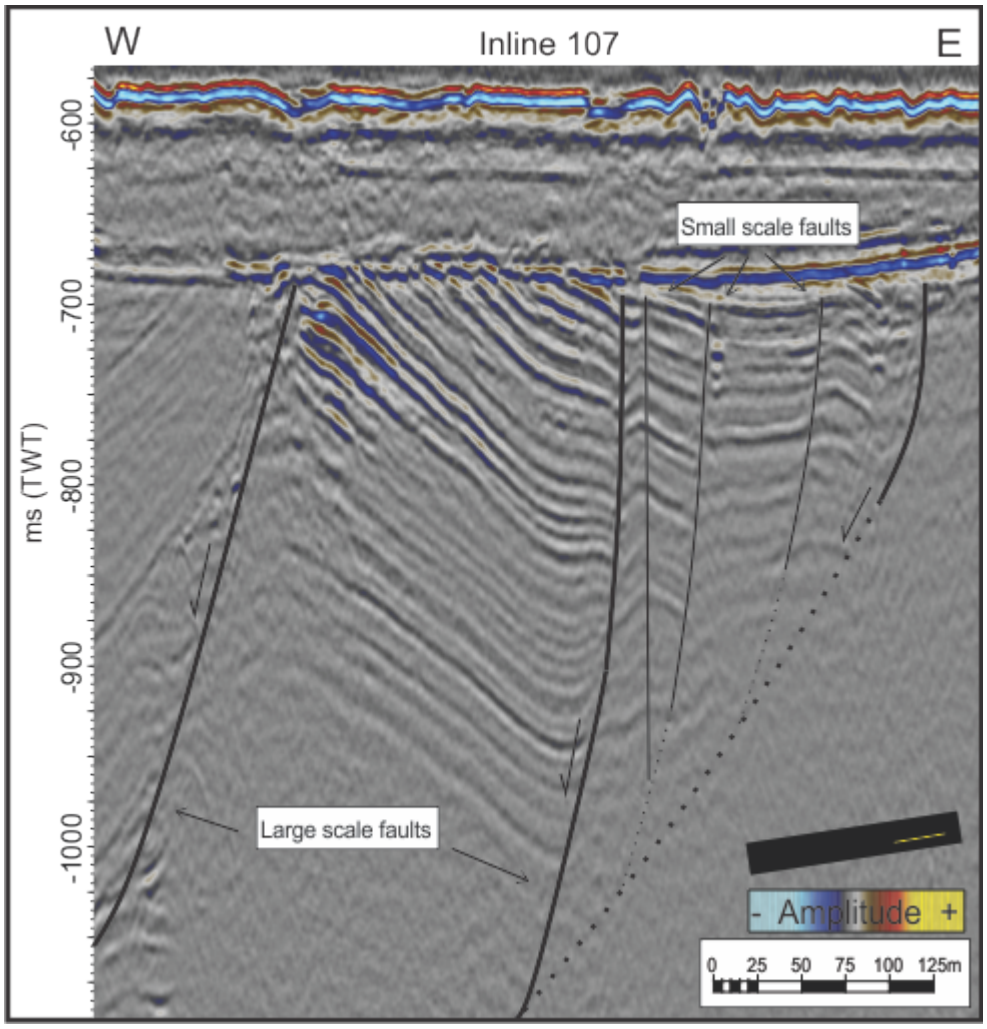

Figure 52. Seismic cross section of eastern part of Inline 107, showing interpreted faults.

The larger-scale fault complex has an East-West direction. The faults are relatively parallel and can be interpreted as normal faults half grabens (Twiss and Moores, 2007) (Figure 53). We can see that the normal faults have a decreasing angle of dip with depth, which are assumed to meet and join a detached fault below the scope of the dataset. The vertical offset of the faults is not seen because of the URU erosional surface. None of the faults crosses the URU within the dataset. Figure 52 shows an interpretation of some of the major faults located within the eastern part of the survey area and how they may join in the deeper sections.

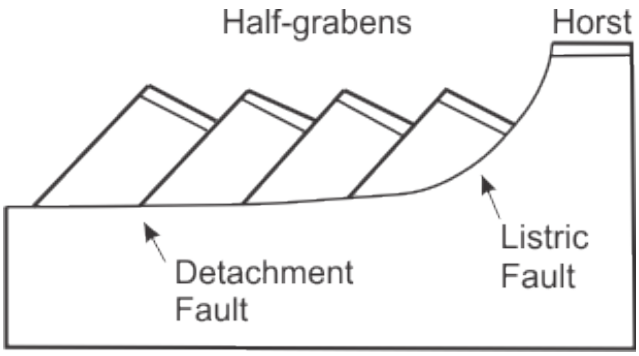

Figure 53. Figure illustrating the half-graben fault structure. Modified from Twiss and Moores, 2007.

4.2 Fluid flow interpretation

Several high amplitude anomalies are seen within the 3D cube of the dataset. These features vary in shape, size, and orientation. In this chapter, a selection of the most prominent features are interpreted and described in detail.

4.2.1 RMS amplitude

Several enhanced seismic reflections, are observed in vertical seismic sections (e.g. bright spot in Figure 54). These enhanced reflections are common in the Barents Sea and represent shallow gas accumulations (Vadakkepuliyambatta et al., 2013; Chand et al., 2012) In order to map these reflections as 3D features several attributes are available in the Petrel software. These attributes may help in finding migration pathways for gas, and map the extent of accumulations. In order to map paleo-environments, a volume within a defined sediment package is set. This is done by defining an area between two horizons or a time window above or below a horizon. For the bright spot in Figure 54, a horizon was made both below and above it (at about 630 ms and 670 ms TWT) to create the attribute map.

The Root Mean Square (RMS) amplitude is used as a volume attribute in order to highlight gas presence in the subsurface, but will also show lithological contrasts, since it maps strong amplitudes regardless of whether they are positive or negative. A minimum-value seismic amplitude attribute map will display only the strongest negative amplitude within a defined volume and may be better suited for mapping gas features (Andreassen et al., 2007).

4.2.2 Gas accumulation 1

This strong reflection amplitude occurs at the Upper Regional Unconformity. The top of the high amplitude reflection is located at about 637 ms (TWT) and the base at about 670 ms (TWT). The amplitude anomaly seen on the RMS amplitude map (Figure 54) is an elongated feature with a NE – SW orientation. The length is about 100 meters and width about 25 meters at the widest, giving it an area of 2500 m^2.

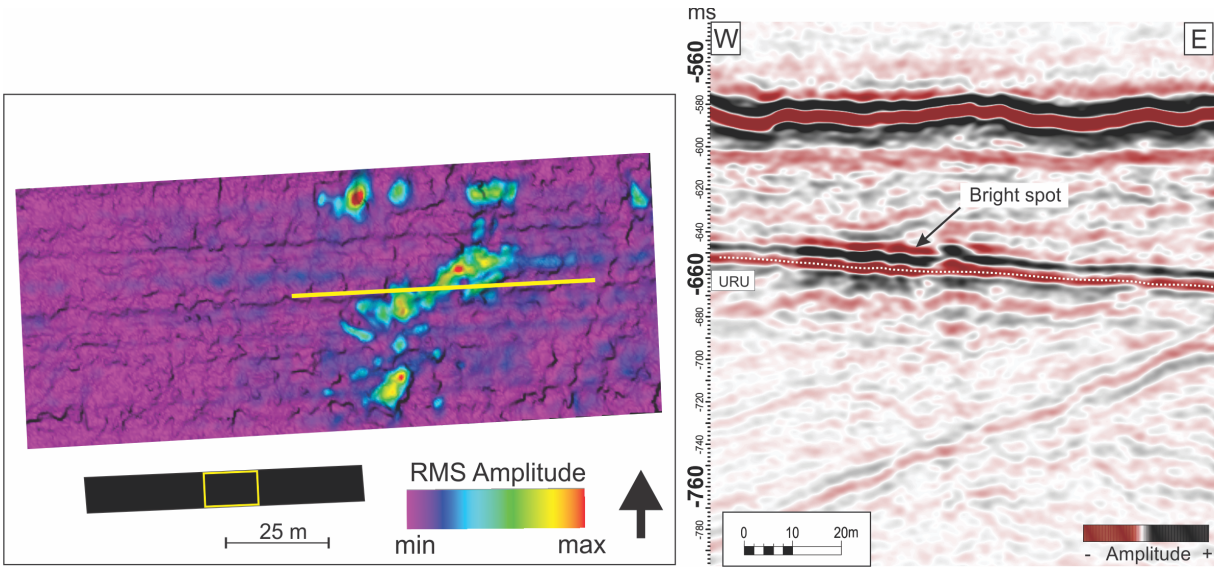

Figure 54. Seismic cross section showing acoustic bright spot located at the URU (dashed line). RMS amplitude map of values between 630 ms – 670 ms TWT showing the amplitude anomaly, with the yellow line indicating the seismic section.

4.2.3 Gas accumulation 2

Amplitude anomaly (Figure 55) is located at the URU in the northeast section of the dataset and interpreted as a gas accumulation. The feature shows several bodies located at roughly the same depth, which may be connected to each other through the faults or the strata. The high amplitude anomalies show a phase reversal relative to the seafloor. The amplitudes are strongest in the northern part and have an east-west orientation. The strongest reflectors are located at -670 ms TWT, about 83 ms TWT below the seabed. The length of the feature is about 125 m and about 40 m in width. Several faults are located below the anomalies leading up to the URU, including a couple of larger-scaled faults. The stratigraphy below the anomalies indicates rotated fault blocks, shown by dipping layers.

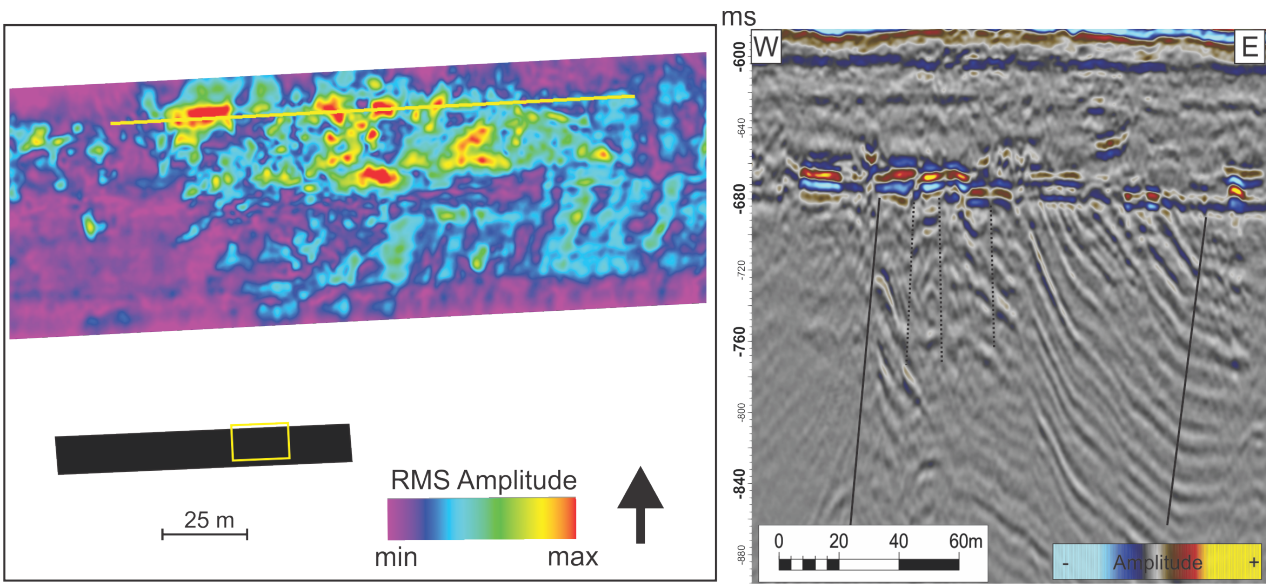

Figure 55. Seismic section showing amplitude anomalies located above deep and shallow faults (shown with whole and dashed lines). RMS amplitude map including values between 650-700 ms TWT of the amplitude anomalies.

4.2.4 Gas accumulation 3

Strong phase reversals are observed at URU in the northeastern part of the dataset interpreted as a gas accumulation. The high amplitude feature appears as an elongated feature in North-South direction documented in the minimum amplitude map (Figure 56 B). The top of the bright spot feature are located at 672 ms (TWT) and the base at 687 ms (TWT) (Figure 56 A). Using a velocity of 1800 m/s (Figure 6, Chapter 1.1.2) the depth below the seabed is 85 ms TWT (76.5 m TVD). The length of the anomalies are 22 m and 27 m respectively, making these small features.

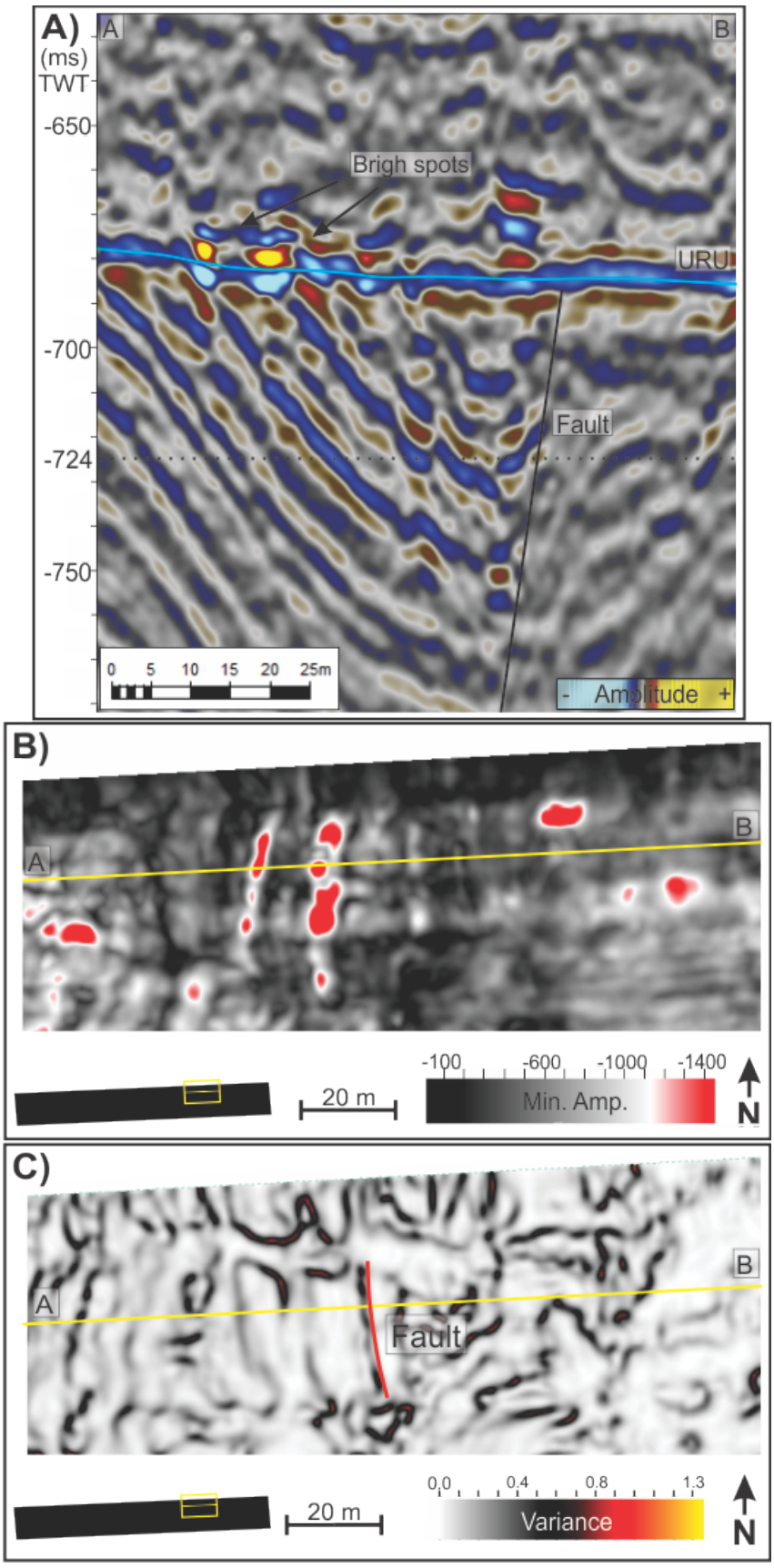

Figure 56. A) Seismic cross section of the dataset that shows bright spots located at the URU and high amplitude layers located below. B) Minimum amplitude attribute map of the volume between 660 ms and 690 ms TWT showing the amplitude anomalies. C) Variance attribute map showing fault seen in cross section A).

These gas accumulations are located in relation to a fault (Figure 56 A). The dipping reflections indicate that the fault block has been rotated. The strong reflections indicate that hydrocarbons have migrated up through the layers. However, the hydrocarbons can not have originated within these layers leading to the belief that the hydrocarbons have migrated up along the fault before entering the sediment layer. The fault can be seen in a time slice (724 ms TWT) through a variance cube of the area in Figure 56 C.

4.2.5 Gas accumulation 4

This amplitude anomaly is interpreted as a flat spot feature (Figure 57 A). The flat spot is observed at 975 ms (TWT) in the center of the dataset. The flat spot is located within the Jurassic strata in between a fault and the Top Hekkingen stratigraphic boundary. A time slice at 975 ms (TWT) shows the fault boundary and the Top Hekkingen boundary. In Figure 57 B a RMS amplitude map of the volume between 950 ms and 990 ms (TWT) is overlain a time slice showing how the flat spot is confined between the boundaries. Because of the positioning of the flat spot within the structural features, it is interpreted that the gas has migrated up through the strata within the Hekkingen formation before accumulating at the fault, which acts as a seal for further migration.

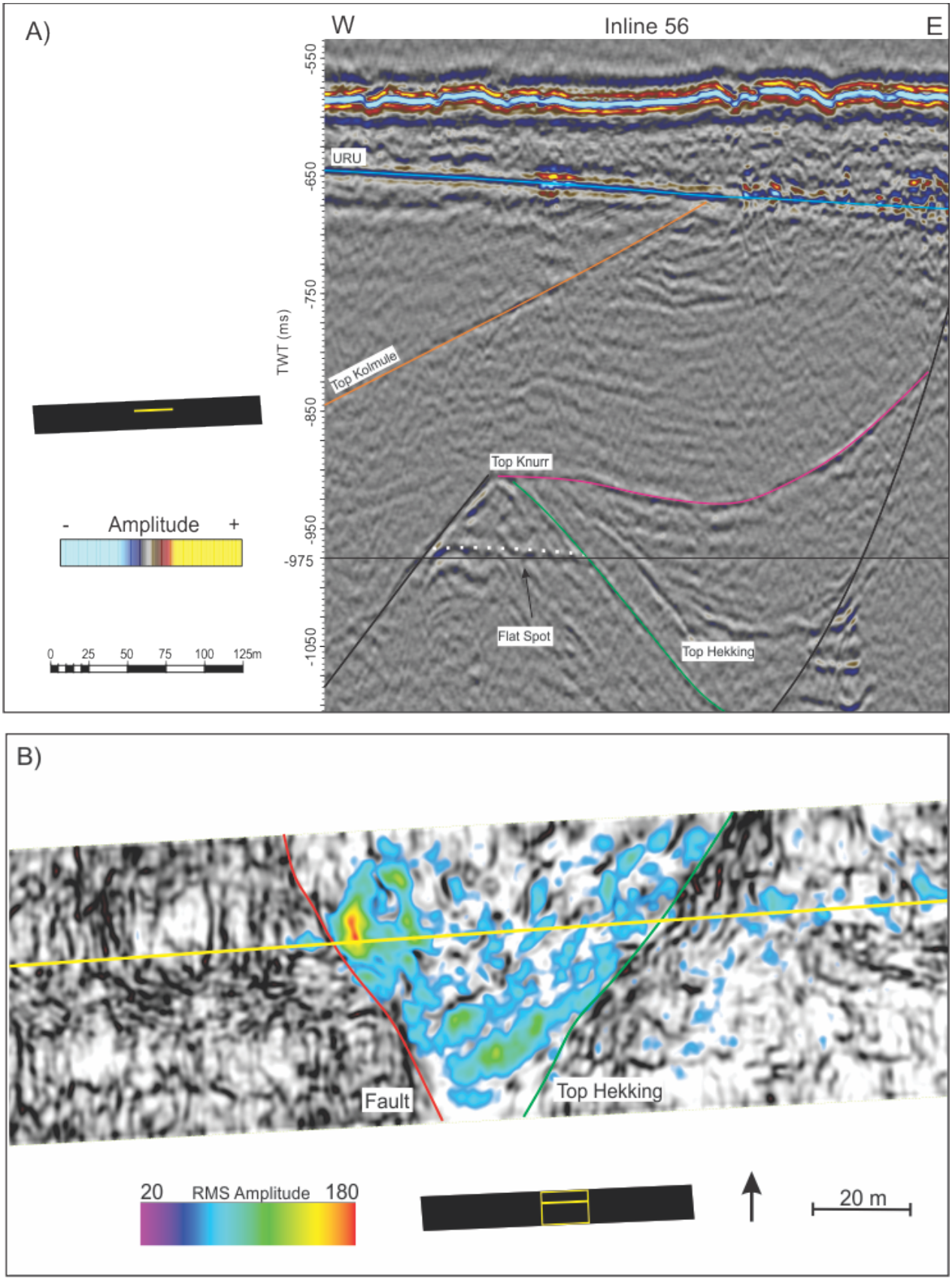

Figure 57. A) Seismic cross section of part of Inline 56 showing a flat spot amplitude anomaly below the Top Hekkingen horizon. B) Time slice through a variance cube made of the dataset showing the Top Hekkingen horizon and fault boundary. A RMS Amplitude attribute surface is overlain the time slice to show the location of the flat spot within the confines of these boundaries.

4.2.6 Vertical fluid migration

In the dataset, there are areas with acoustic masking. They vary in size and shape both vertical and horizontally. Figure 58 shows an example of what could be interpreted as a focused fluid flow feature (Løseth et al., 2002). It can be identified by a semi-circular vertical zone of more chaotic seismic data from deeper to shallower strata (Løseth et al., 2002). The vertical zones terminate in high amplitude anomalies. Pull down effects are also observed in some locations. This structure could resemble a chimney or pipe which occur widespread in the Barents Sea (Vadakkepuliymabatta et al., 2013).

The small gas chimney feature is located in the northern central part of the dataset above the fault termination seen in Figure 57. The feature extends down to about -900 ms (TWT) and terminates in a high amplitude anomaly at -650 ms (TWT) giving it a vertical extent of 250 ms. Using a velocity of 2000 m/s (Figure 6, Chapter 1.1.2) the observable vertical extent is 250 meters (TDV). In a time slice (Figure 58 B), we can see a circular shape following the chimney structure laterally. Pull down effects in the seismic section correlating with the chimney structure are also observed. The chimney feature terminates at a bright spot feature located at the URU (-650 ms TWT). Directly below the bright spots are areas of acoustic masking. These bright spots are located directly below depressions on the seabed.

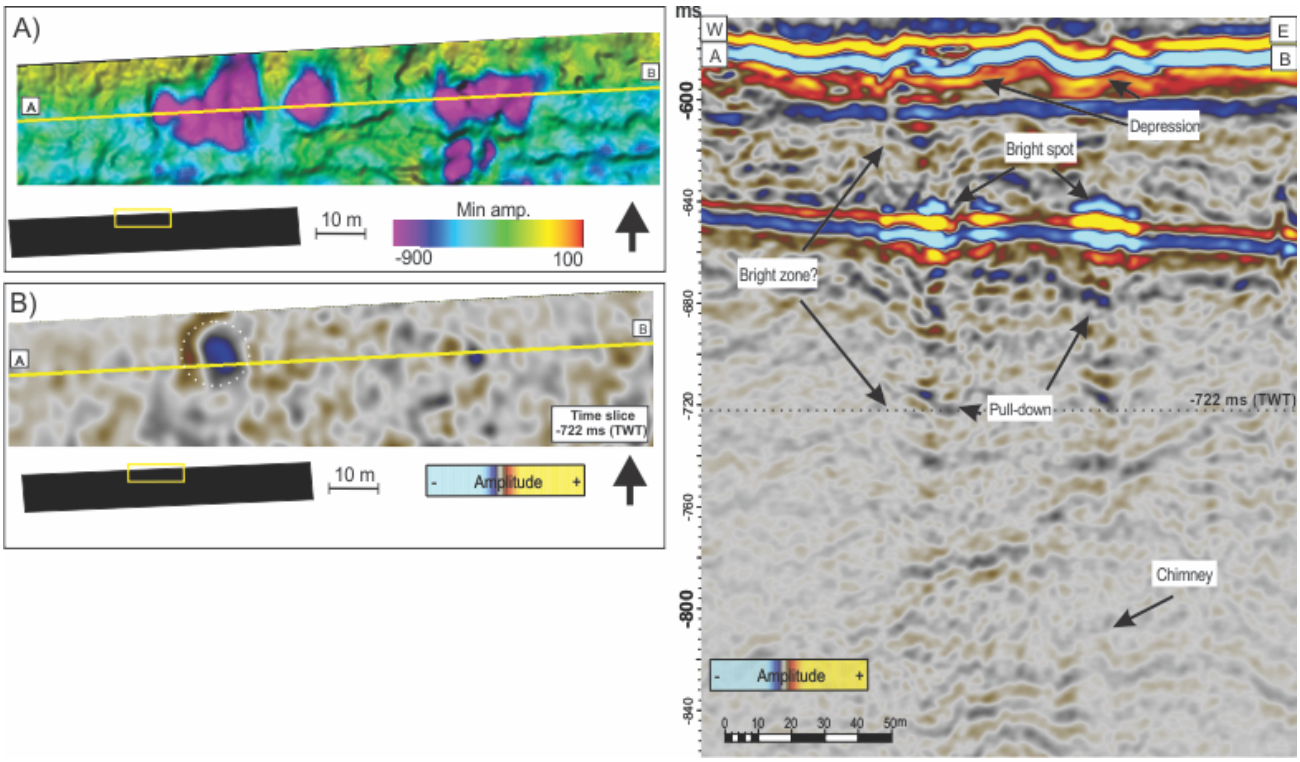

Figure 58. Fluid migration features seen in a seismic cross section. A) Shows a minimum amplitude attribute map of bright spots located at the URU. B) Shows a time slice at -722 ms (TWT) showing the semi- circular shape of the chimney structure, which can be followed up through the seismic section.

5 Discussion

In this chapter, I will look at the interpretations and observations presented in the Results chapter with the goal of understanding the relationship between the shallow gas accumulations, migration of the gas and the structural development of the study area. This chapter will connect these features together in order to understand the hydrocarbon migration system within this area. I will also present a brief evaluation of the processing including some discussion of processing options that were tried but ultimately not included in the final processed volume due to time constraints.

5.1 Processing

During processing several steps where considered but not included. The main reason for not including processing steps was the time restraints. Several steps were dropped in order to save time, or due to low yield for the time invested. A few of the processes that were considered, but not included are explained further here.

5.1.1 SharpSeis DeGhosting

One processing step that was looked into, but not included in the final product was the SharpSeis DeGhosting process. The SharpSeis routine is dedicated for removing ghost wave field from marine seismic data (RadExPro manual, 2014). The SharpSeis module utilizes a stabilized approximate recursive filter solution, applied to a seismic trace in both forward and reverse time. This creates two traces; one trace with the primary signal and the ghost, and one with the ghost but not the primary signal. These two traces are then combined in a nonlinear way in order to maximize the signal and suppress the noise (Figure 59).

The main difference between the SharpSeis module and the standard DeGhosting module is the fact that it creates two traces giving a much higher quality than the filter used in the standard DeGhosting. The module in RadExPro is more complicated than the standard DeGhosting, which is the main reason why it was not used in the processing.

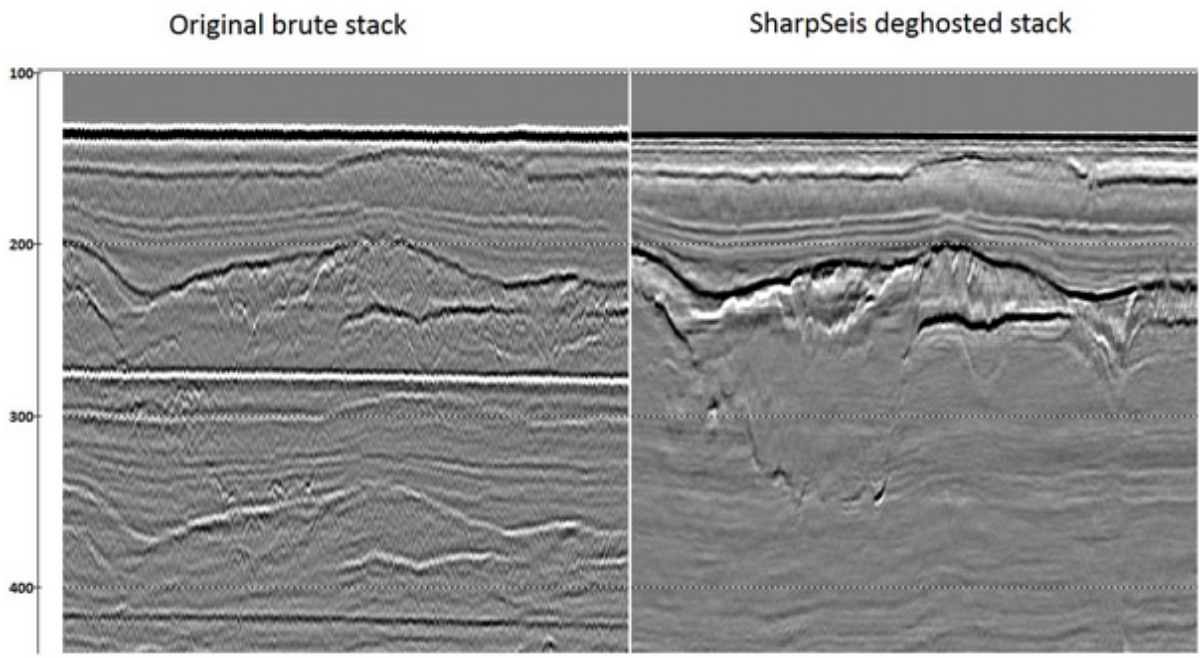

Figure 59. Example of improvements made with the SharpSeis DeGhosting. Data from the Norwegian Sea acquired with a P-Cable system with an air gun source and 12 8-channel streamers at around 2.5 m. From RadExPro webpage.

In my processing the SharpSeis DeGhosting was done for one channel, but did not proceed further due to time constraints. An attempt was also made for addition to an entire line to save time, which (in my case) did not work. Given more time SharpSeis is a processing step that I would include seeing as it greatly improves the signal to noise ratio.

5.1.2 Filtering

Several filters were used during processing to improve the signal to noise ratio, however, a few were tested but not included in the end result.

The Butterworth filtering module applies Butterworth frequency filtering (Figure 60) to each input trace. It is designed in such a way that it makes its amplitude frequency response as smooth as possible within the pass band, but drops to almost zero for frequencies within the stop band range (RadExPro manual, 2014). The amplitude frequency response G(w) of an n^{th} order Butterworth low-pass filter is expressed by:

$$G^2(w) = \frac{1}{1 + \left(\frac{w}{w_c}\right)^{2n}}$$

Where n represents the filter order. For a first order filter the response rolls off at -6 dB per octave and so on. W_c represents the cut-off frequency.

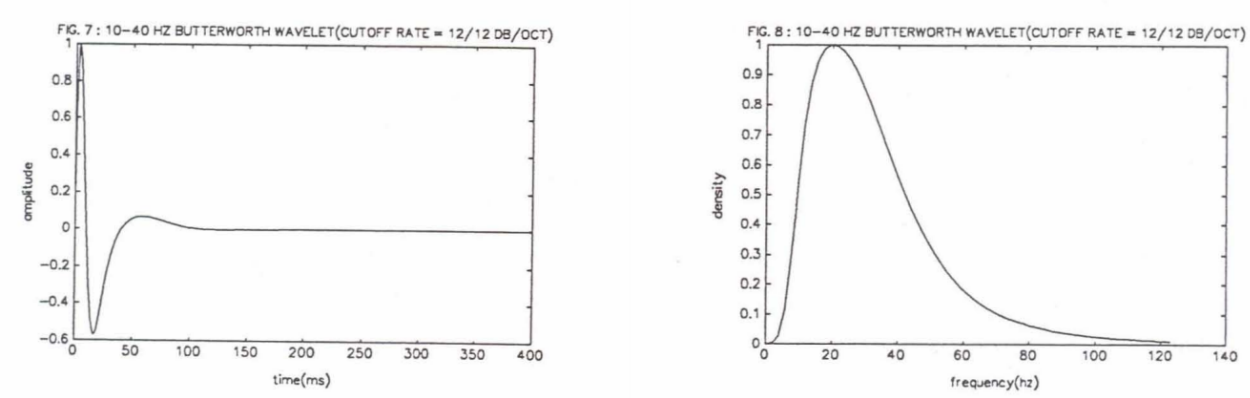

Figure 60. Butterworth wavelet shown in a time and frequency spectrum. From Harold, 1994.

The most distinct difference between the Butterworth wavelets and other wavelets, such as Ormsby (Chapter 3.2.2), is that it is a minimum phase and physically realizable (Ryan, 1994). This filter was added to my data during the NMO and Stacking stage, however, this filter did not yield any noticeable results and was not used in the final product.

In addition to the Butterworth filtering module an additional Ormsby bandpass filter was considered in order to remove the notch in the frequency spectrum (Figure 19, Chapter 2.3) by smoothing the signal. This reduced the signal so extensively that it was discarded and the noise was kept in.

Given more time, more filtering and processing could be conducted in order to improve the dataset quality, but a seismic dataset will never be perfect, and for this thesis, the dataset was sufficient for interpreting the desired features.

5.2 Vertical migration of fluids

Vertical fluid migration can be inferred from zones of acoustic masking and acoustic pipes. Acoustic masking may also occur along faults, indicating fluid migration along the fault. These areas of acoustic masking can give us a better understanding of hydrocarbon sources, their migration systems, and leakage zones (Andreassen et al, 2007 B).

5.2.1 Origin of the gas

For hydrocarbon migration to take place a source rock is needed to produce the hydrocarbons. As seen in Chapter 1.1.1 for hydrocarbon production to occur the organic material (kerogen) must be at a certain temperature and pressure. During the rifting of the Barents Sea in the Cenozoic, regional uplift has occurred in addition to glacial erosion, resulting in potential source rocks not being buried as deeply as assumed (Dore, 1996; Faleide et al, 1996). No oil shows have been interpreted within my dataset indicating that the potential source rock is below the oil window leading to the belief that the source of the gas is Triassic or older in origin. This also fits the model presented by Ohm et al. seen in Figure 4, Chapter 1.1.1, though the number of wells penetrating this deep are few and the quality of the source rocks are more uncertain. However, based on this dataset the source rock has been interpreted to be of Triassic age.

5.2.2 Migration systems

Acoustic masking is an important indicator of fluid migration in seismic data. Masking refers to an area of the seismic profile with low seismic reflectivity or areas that are highly distorted, or disturbed (Andreassen et al, 2007 B) due to scattering of the seismic energy when the acoustic signal hits gas (Figure 61). The acoustic masking also coincides with faults or extends from fault terminations, which indicates gas migration along and from faults. Figure 58, Chapter 4.2.6 shows a masked zone in map view, having a semi-circular shape suggesting concentrated vertical fluid flow typical of gas chimneys.

A pull-down effect is seen within several of the acoustic masked zones. In Figure 58, there are indications that the pull-down effect is decreasing with depth. This may be an indication

of the amount of gas in the chimney, with the largest effects seen directly below bright spots. Bright spots along the chimney may indicate areas where gas has accumulated due to seals or lower permeability. Evidence of this can be seen in Figure 61 where bright spots occur at the fault and the top Kolmule stratigraphic horizon. This indicates that migration occurred after the Torsk Formation was deposited.

Within the dataset, fluid migration is observed (Figure 61) from the interpreted Hekkingen Formation, Jurassic and Triassic sediments. However, the acoustic masking within these formations may not be the source of the fluid migration. The source may be deeper Triassic to Carboniferous sediments.

Even though hydrocarbon indications are seen above the URU, the most prominent features are seen at or below the erosional surface. The URU thus acting as an impermeable surface with all bright spots and flat spots below it, though evidence of limited fluid migration to the seafloor is observed (Pockmarks Figure 63).

5.2.3 Fluid accumulation

Figure 54, 55, 56, and 57 show that there exists large areas of high amplitude anomalies within the survey area. Most of these accumulations are located at the URU. Zones of acoustic masking lead up from the deeper formations and terminate at the amplitude anomalies. Most likely, the URU acts as an impermeable boundary where hydrocarbons accumulate beneath. Structures below indicate lateral migration along the strata in the eastern part of the survey area. The hydrocarbons may have migrated up along deep-seated fault before entering more permeable strata and then followed the strata up to the URU.

Figure 61 shows a sketch of the survey area, highlighting the gas features and accumulations. The sketch shows the flat spot within the Jurassic sediments from Figure 57, and how the gas may have migrated up from the flat spot along the fault as observed in the seismic. Gas chimneys are observed from the termination of the fault and leading up to flat spots at the URU (Figure 58). From the gas accumulations at the URU periodical leakage may be the cause of observed pockmarks on the seabed (Figure 63). Gas has also been observed to migrate up along faults in the eastern part of the survey area as well, before entering permeable strata and accumulating at the URU (Figure 56). Accumulations of gas directly

above faults also support the idea that the gas uses faults as a migration pathway (Figure 55).

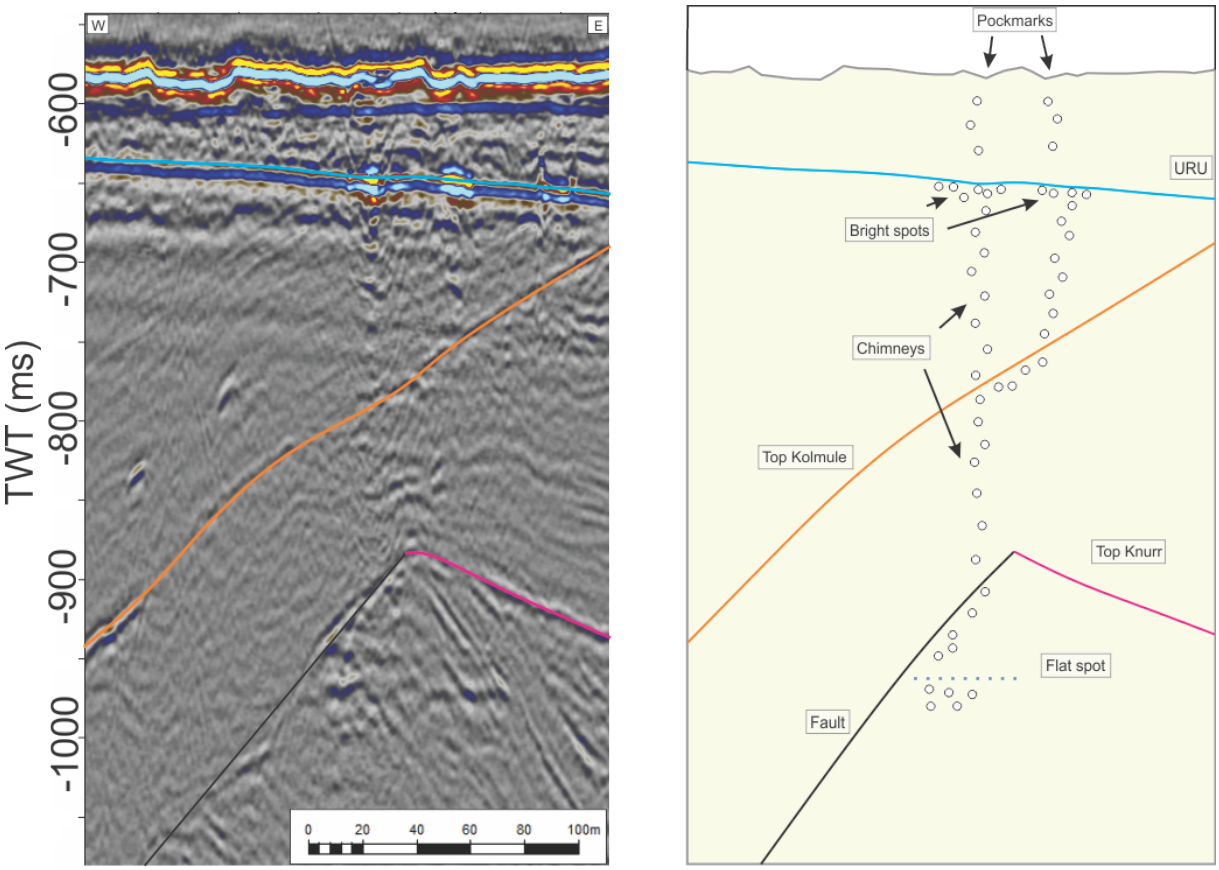

Figure 61. Seismic cross section with interpretation. Interpretation showing how gas has migrated from an observed flat spot within the Jurassic strata along a fault boundary with migration up through Cretaceous sediments to the URU. Along the gas chimney, bright spots indicate places where gas has been trapped, such as the Top Kolmule surface. Bright spots at the URU show where the gas has accumulated. Pockmarks on the seabed indicate leakage from the reservoirs to the seabed.

5.3 Pockmarks

Several depressions are observed on the seabed (Figure 46 and 47) in the dataset. These depressions may have been formed by several different processes.

The Barents Sea has been effected by glacial erosion and deposition during the Cenozoic. A range of geomorphic features are seen within the dataset related to the glacial activity. One of these features is linear to curved furrows observed on the seabed. These are interpreted as iceberg scours, created by icebergs eroding the seabed (Figure 62). When the icebergs

detach from a glacier they are dragged along the seabed by wind and ocean currents. The furrows are typically 100-300 m wide, with relief of 3-10 m and an extent of up to 20 km (Andreassen et al, 2008). Several of these features where observed within the dataset (Figure 46).

Within the scour marks, circular depressions interpreted as pockmarks were observed. Pockmarks are considered to be areas with focused fluid flow through the seabed. Pockmarks may be formed by freshwater, conducted through permeable units from land (Pau, 2014). This is not likely for this dataset as it is far from land without any visible or possible connection.

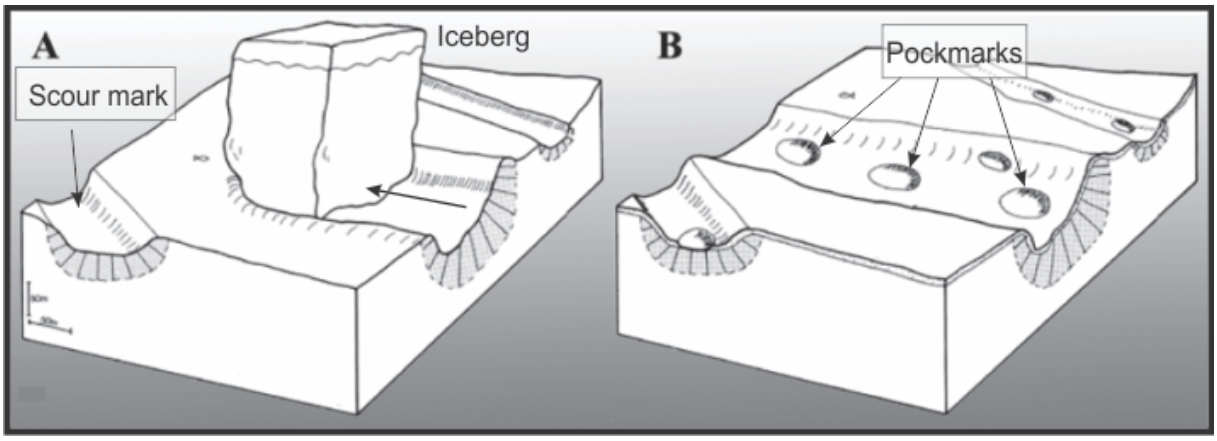

Figure 62. Illustration showing the process of icebergs creating scour marks and pockmarks located within these marks. Modified from Hovland,1988.

Pockmarks may also be formed by escaping pore water from softer sediments such as silt or clay. This happens when the pressure builds up due to sedimentation, until the pressure causes the pore water to migrate up through the sediments to the seabed, and create depressions by eroding the sediments on the seabed (Harrington, 1985). Since there are examples of acoustic masking below the pockmarks in the dataset (Figure 47 and 63), which would not be caused by water migration, the pockmarks are not interpreted as the result of water migration.

The most common fluid related to the creation of pockmarks is hydrocarbons, mainly methane of biogenic source, because of the shallow depth it is produced at. This is supported by the features found in the dataset. Fluids from deeper structures might have

leaked up to the seabed through pipe structures. Several of the pockmarks seen in the dataset have areas of masking below indicating gas migration from a deeper source up to the seabed. The time of formation of the pockmarks is hard to determine because of their dynamics. There is debate as to whether pockmarks are currently active, previously active or even episodically active (Pau, 2014).

In this dataset, no evidence of a Bottom-Simulating Reflector (BSR) was found, leading to the assumption that the gas is leaking from a structural trap rather than from hydrates. However, gas hydrates may still be a factor even without a visible BSR. The pockmarks seen on the seabed must have been created after the deglaciation following the Last Glacial Maximum (LGM). No pockmarks were observed on the URU, which indicates that gas migration did not occur before the LGM, or that they have been eroded after creation.

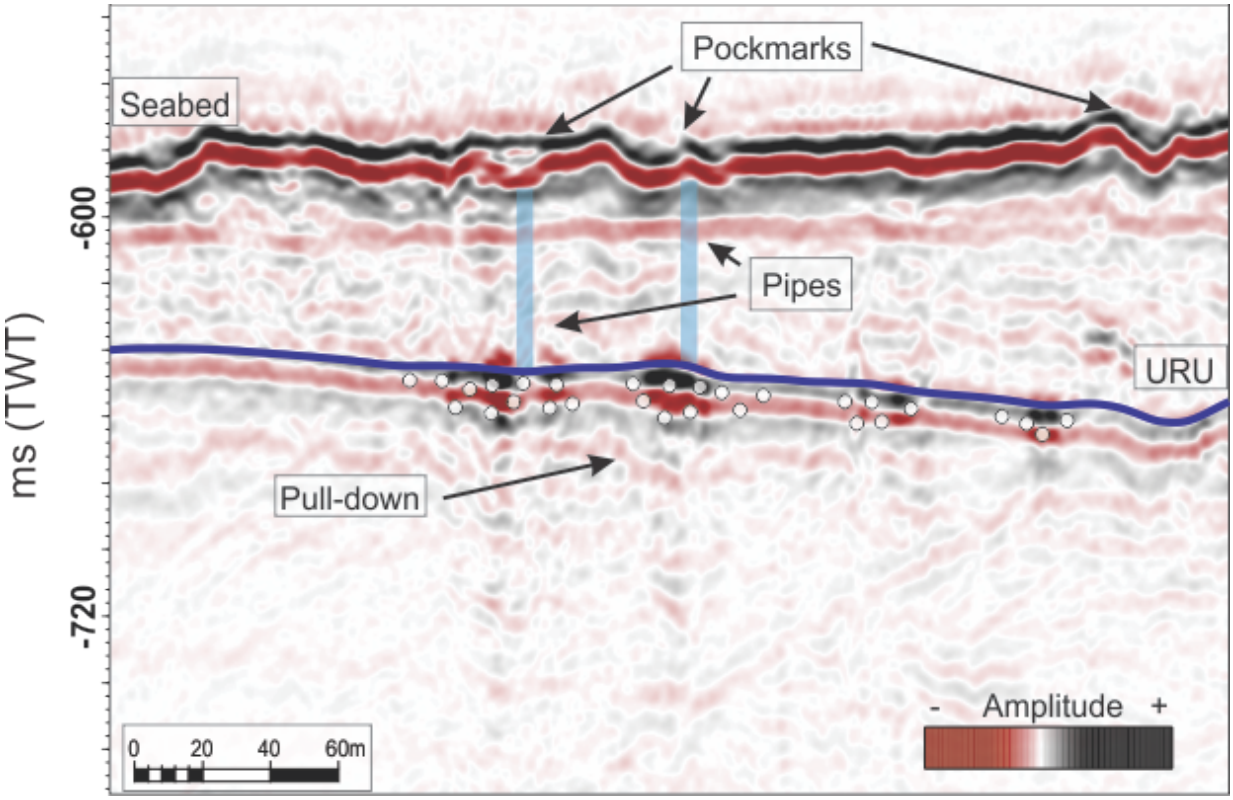

Figure 63. Seismic cross section of Inline 18. Showing pipe structures going from high amplitude anomalies located at the URU, and up to pockmark locations on the seabed.

5.4 Model of fluid migration

The Bear Island Trough Fault Complex defines the transitional zone between the Loppa High platform to the southeast and the Creaceous basin to the northwest (see map Figure 16, Chapter 2.3) (Gabrielsen, 1997). The dip-slip components on the upper Triassic level indicates extensional origin. During the late Cretaceous this area saw renewed subsidence of the Bjørnøya Basin, which can be observed by patterns of extension and listric faulting. The major structuring of the Fault Complex occurred during an extreme phase of subsidence in the early Cretaceous (Gabrielsen, 1997). Although no direct evidence of reactivation of the faults is seen within the dataset, this might have been a factor in the hydrocarbon migration along the faults.

Due to the erosion (URU) of the Loppa High, seen in the eastern part of the dataset, the termination time of the late Cretaceous inversion remains unknown.

The tectonic events may have resulted in cessation of petroleum generation, migration from source rocks, and leakage from reservoirs. The glacial activity may have led to leakage to the seabed and the formation of pockmarks.

The glacial activity in the area has led to significant erosion as seen by the Upper Regional Unconformity, but also the effect of loading due to the weight of the ice on the sediments below. Extraordinary pressure fluctuations may provide a mechanism for episodic discharge of methane from deep petroleum systems (Cavanagh et al., 2006). Up to 2000 meters of sediments were removed during the erosion (Henriksen et al., 2011). This lead to reduction in pressure causing expansion of oil/gas in existing reservoirs and possible spills out of traps. In addition to the pressure reduction, a temperature increase may have occurred due to the removal of the ice enhancing the effect on hydrocarbons (Cavanagh et al., 2006). Zones of acoustic masking (Chapter 5.2.2) interpreted as gas chimneys, lead up to and terminate at the URU, supporting the conclusion that migration occurred after the ice was removed. As seen in the previous chapters, the high amplitude anomalies in the dataset are located below or at the URU, most likely due to its trapping properties. From these structural traps, acoustic pipes and areas of chaotic signals leading to the seabed are observed. These acoustic pipes may be a result of a breach of the capillary seal.

The hydrocarbons may therefore have migrated up along faults, before gas expansion and erosion of the overburden lead to further migration up to the erosional surface. When the pressure within the structural trap exceeds the limits of the seal, gas may have leaked to the seabed creating the observed pockmarks. Figure 64 shows a sketch of how this migration may have happened. With gas located at the flat spot within the Jurassic sediments migrating up along the fault, before leaking into the Cretaceous sediments at the fault termination. The gas then migrates up through a focused flow observed as a gas chimney before accumulating at the URU. When the pressure becomes too great for the seal, the gas may periodically leak to the seabed and create the observed pockmarks directly above.

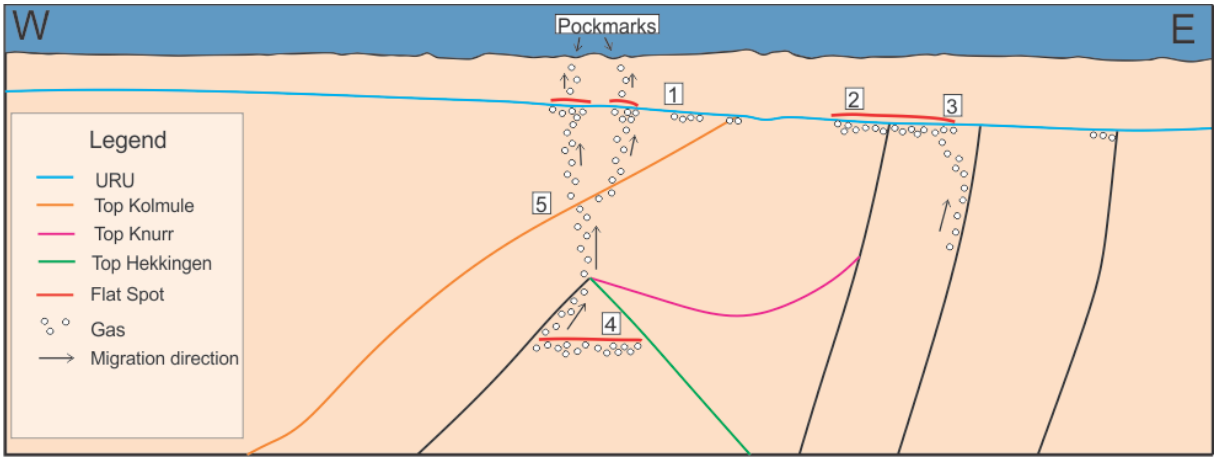

Figure 64. Sketch of survey area showing all identified gas accumulations, and observed fluid flow features seen in seismic sections. Fluid flow feature 1 is seen in Figure 54. Gas accumulation 2 is seen in Figure 55. Fluid flow feature 3 is seen in Figure 56. Gas accumulation 4 is seen in Figure 57. Fluid flow feature 5 is seen in Figure 58.

6 Summary

For this thesis, I processed and interpreted P-Cable high-resolution 3D seismic data from the Bjørnøyrenna Fault Complex acquired during a Helmer Hanssen cruise in 2012. The initial phase of the processing included geometry assignment, merging of data sets from each acquisition line and 3D binning. After assembling the seismic data, a number of different processes are performed to enhance the signal to noise ratio. For this thesis the filtering included Ormsby filtering, DeGhosting, importing tidal data, spherical divergence corrections, static corrections, and deconvolution. All of these processes increased the general quality of the data by removing unwanted noise. For future processing, I would include several more processes in order to further improve the quality. The main goal for further processing would be to remove the notch seen in the frequency spectrum by using the new SharpSeis module. This would allow the studying of features in even greater detail. After filtering the seismic data, stacking and migration is performed. These are essential steps in making a useable seismic cube removing much of the noise and creating a stronger signal. The processed seismic data was exported to the Petrel software for interpretation.

Within the survey area many geological features were observed. The thesis focuses mostly on gas accumulations, and migration features, of which several good examples where examined in detail. Among these were flat spots, bright spots, gas chimneys, and pockmarks. Stratigraphical features such as erosional surfaces, sedimentary packages, and faults were also interpreted in order to better understand the regional history and the processes behind the fluid migration. In order to understand the stratigraphy the nearest available well was utilized. There is a well situated at the location of the dataset, however the data from this well will not be available before 2016. With this data a much better correlation of stratigraphical boundaries could be made, including dating the sediment packages within the eastern fault blocks.

The interpretations of the seismic data indicates that gas has migrated from below the extent of the seismic cube, most likely Triassic or Permian source rocks. These have migrated up along faults before entering more permeable sediment packages such as the Cretaceous and Jurassic, where a prominent flat spot was observed. Within these sediments, the gas has continued migrating upwards along faults and permeable sediments before eventually being

trapped beneath the URU. Most of the gas accumulations are seen at the URU and in the sediments directly below. There are several indications of gas leaking from the accumulations along the URU and up to the seabed. This is observed by zones of acoustic masking, pull-down effects and pockmarks on the seabed.

There are features seen in the seismic cube indicating the glacigenic effects on the area. The most distinct being the URU where glaciers have eroded the subsurface, the sediments above being deposited after the LGM and most likely containing mostly glacigenic material. On the seabed, ploughmarks created by icebergs eroding the seabed after the LGM are seen. Mega scale lineations may also be present in the survey area, but due to the small size of the cube are difficult to observe. Given more time for processing, filtering would give a smoother seabed surface making features easier to observe. Additional processing may also attenuate the survey footprints giving a smoother surface.

7 References

AAPG Wiki (2014): Ln. http://wiki.aapg.org/Main_Page

Andreassen, K. “Geokompendium 2009”. Marine Geophysics Lecture Notes for Geo-3123, University of Tromsø 2009.

Andreassen, K., Laberg, J. S., and Vorren, T. O. (2008): “Seafloor geomorphology of the SW Barents Sea and its glaci-dynamic implications”. Geomorphology 97, 157-177. Elsevier.

Andreassen, K., Nilssen E.G., and Ødegaard, C.M. (2007 B): “Analysis of shallow gas and fluid migration within the Plio-Pleistocene sedimentary succession of the SW Barents Sea continental margin using 3D seismic data”. Springer-Verlag.

Andreassen, K., Ødegaard C. M., and Rafaelsen, B. (2007 A): “Imprints of former ice streams, imaged and interpreted using industry three-dimensional seismic data from the south-western Barents Sea”. The Geological Society of London.

Bjørlykke, K. (2010): “Petroleum Geoscience: from Sedimentary Environments to Rock Physics”. Berlin, Heidelberg: Springer-Verlag Berlin Heidelberg.

Büenz, S., and Mienert, J. (2004): “Acoustic imaging of gas hydrate and free gas at the Storegga Slide”. Journal of Geophysical Research, Vol. 109.

Cavanagh, A. J., Di Primio, R., Scheck-Wenderoth, M., and Horsfield, B. (2006): “Severity and timing of Cenozoic exhumation in the southwestern Barents Sea”. Journal of the Geological Society. 163. 761-774.

Chand, S., Thorsnes, T., Rise, L., Brunstad, H., Stoddart, D., Bøe, R., Lågstad, P., Svolsbru, T. (2012): Multiple episodes of fluid flow in the SW Barents Sea (Loppa High) “Evidenced by gas flares, pockmarks and gas hydrate accumulation”. Earth and Planetary Science Letters. Vol. 331-332. 305-314.

Department of Geology, University of Tromsø (2011): “Geosystem 3D seismic imaging” Ln. http://www.ig.uit.no/geosystem3d/infrastructure.html

Dore, A. G. (1995): “Barents Sea Geology, Petroleum Resources and Commercial Potential”. Arctic, 48(3). 207-221.

Dore, A. G., and Jensen, L. N. (1996): “The impact of late Cenozoic uplift and erosion on hydrocarbon exploration: offshore Norway and some other uplifted basins”. Global and Planetary Change 12. 415-436.

Faleide, J. I., Solheim, A., Fiedler, A., Hjelstuen, B. O., Andersen, E. S., and Vanneste, K. (1996): “Late Cenozoic evolution of the western Barents Sea-Svalbard continental margin”. Global and Planetary Change. 12. 53-74.

Gabrielsen, R. H., Grunnaleite, I. and Rasmussen, E. (1997): “Cretaceous and Tertiary inversion in the Bjørnøyrenna Fault Complex, south-western Barents Sea”. Marine and Petroleum Geology, Vol. 14, No. 2, pp. 165-178.

GI GUN Operation and Maintenance Manual (2009).

Glørstad-Clark, E., Faleide, J. I., Lundschien, B. A., and Nystuen, J. P. (2010): “Triassic seismic sequence stratigraphy and paleogeography of the western Barents Sea area”. Marine and Petroleum Geology 27, 1448-1475.

Guzzetta, G., andd Cinquegrana, R. E. (1987): “Fluid Tectonics – A Little Appreciated Facet of Buoyancy Tectonics”. Tectonophysics, 139 321-324.

Harrington, P. K. (1985): “Formation of Pockmarks by Pore-Water Escape”. Geo-Marine Letters 5. 193-197.

Heggland, R. (1998): “Gas seepage as an indicator of deeper prospective reservoirs. A study based on exploration 3D seismic data”. Marine and Petroleum Geology, 15, 1-9.

Henriksen, E. et al. in press (2011): “Uplift and erosion of the greater Barents Sea: Impact on prospectivity and petroleum systems”. Arctic Petroleum Geology. Memoir of the geological Society of London.

Henry, S. (2004): “Understanding Seismic Amplitudes”. Search and Discovery Article #40135.

Hovland, M., Gardner, J. V., and Judd, A. G. (2002): “The significance of pockmarks to understanding fluid flow processes and geohazards”. Geofluids, 2(2) 127-136.

Hovland, M., and Judd, A. G. (1988): “Seabed Pockmarks and Seepages: Impact on Geology, Biology and the Marine Environment”. Graham and Trotman, London. 127.

Judd, A.G., Hovland, M., 2007. Seabed Fluid Flow: The Impact on Geology, Biology and the Marine Environment. Cambridge University Press.

Keary P., Brooks, M., and Hill, I. (2002): “An Introduction to Geophysical Exploration. Vol. 3”. Blackwell Publishing.

Løseth, H., Gading, M., and Wensaas, L. (2009): “Hydrocarbon leakage interpreted on seismic data”. Marine and Petroleum Geology, 26(7), 1304-1319.

Mienert, J. (2013): “Gas-hydrate Systems in Petroleum Provinces”. Discovery Article #90177, Arctic, Polar Petroleum Potential Conference & Exhibition, Stavanger, Norway, October 15-18 2013.

Mussett, A.E., and Khan, M.A. (2000): “Looking into the Earth, an Introduction to Geological Geophysics”. Cambridge University Press.

Ostanin, I., Anka, Z., di Primio, R., and Bernal, A. (2013): “Hydrocarbon plumbing systems above the Snøhvit gas field: Structural control and implications for thermogenic methane leakage in the Hammerfest Basin, SW Barents Sea”. Marine and Petroleum Geology, 43, 127-146.

Pau, M., Hammer, Ø., Chand, S. (2014): “Constraints on the dynamics of pockmarks in the SW Barents Sea: Evidence from gravity coring and high-resolution, shallow seismic profiles”. Marine Geology 355, 330-345.

Petersen, C. J., Bünz, S., Hustoft, S., Mienert, J., and Klaeschen, D. (2010): “High-resolution P-Cable 3D seismic imaging of gas chimney structures in gas hydrated sediments of an Arctic sediment drift”. Marine and Petroleum Geology. (In press) 1-14.

Petrel 2011, Petrel Fundamental Course. Schlumberger.

RadExPro Manual (2014): Deco Geophysical.

RadExPro Webpage (2014): ln. radexpro.com DECO Geophysical SC 2010.

Rafaelsen, B. (2014): “Seismic resolution (and frequency filtering)”. University of Tromsø.

Reemst, P., Cloetingh, S., and Fanavoll, S. (1994): “Tectonostratigraphic modelling of Cenozoic uplift and erosion in the south-western Barents Sea”. Marine and Petroleum Geology, 11(4), 478-490.

Ryan, H. (1994): “Ricker, Ormsby, Klander, Butterworth – A Choice off wavelets”. Canadian Society of Exploration Geophysicists. September 1994.

Sanchis, C. (2010): “Signal Processing Techniques for the Enhancement of Marine Seismic Data”. University of Tromsø.

Schlumberger (2015), “Oilfield Glossary”: http://www.glossary.oilfield.slb.com/en/Terms/p/pull-up.aspx

Selly, R.C. (1998): “Elements of Petroleum Geology”. San Diego, USA: Academic Press.

Storvoll, V., Bjørlykke, K., and Mondol, N. H. (2005): “Velocity-depth trends in Mesozoic and Cenozoic sediments from the Norwegian shelf”. AAPG Bulletin, V. 89, No. 3 pp. 359-381.

Thiessen, O. (2013): “Petroleum Systems of the Norwegian Barents Sea”. AAPG Search and Discovery Article #90177.

Tissot, B. P., and Welte, D. H. (1984): “Petroleum Formation and Occurrence”. Springer, 2nd ed.

Twiss, R. J., and Moores, E. M. (2007): “Structural Geology”. New York. W. H. Freeman and Company.

USGS (2014): “WHSC Seismic Profiling systems”. Ln. http://woodshole.er.usgs.gov/operations/sfmapping/seismic.htm

Vadakkepuliyambatta, Sunil; Bünz, Stefan; Mienert, Jurgen; Chand, Shyam. Distribution of subsurface fluid-flow systems in the SW Barents Sea. Marine and Petroleum Geology 2013; Volum 43. ISSN 0264-8172.s 208 - 221

Veeken, P. (2007): “Seismic Stratigraphy, basin analysis and reservoir characterization”. Handbook of Geophysical Exploration: Seismic Exploration (Vol. 37) Elsevier.

Vorren, T. O., Richardsen, G., Knutsen, S. M., and Henriksen, E. (1991). “Cenozoic erosion and sedimentation in the western Barents Sea”. Marine and Petroleum Geology, 8(3).

Vorren, T. O., Bondevik, S., Elverhøi, A., Fjeldskaar, W., Mangerud, J., Salvigsen, O., Siegert, M. J., and Svendsen, J.I. (1998): “The Last Glacial maximum of Svalbard and the Barents Sea area: Ice sheet extent and configuration”. Quaternary Science Reviews, Vol. 17 pp. 43-75.

Winsborrow M. C., Andreassen, K., Corner, G.D., and Laberg, J. S. (2010): “Deglaciation of a marine-based ice sheet: Late Weichselian paleo-ice dynamics and retreat in the southern Barents Sea reconstructed from onshore and offshore glacial geomorphology”. Quaternary Science Reviews .

3D seismic line log

Expedition: Helmer Hanssen June/July 2012 Survey: Lundin Area A 30.06. – Sheet #: 1 - 4

Survey configuration: see end of document Times are UTC

3D line number:	Date: Start - end	Time (UTC): Start - end	Shot point number First - last	Shot point number when crossing planned start and end of line	Comments (sailing direction, ship speed, depth sensor, wind speed, air temperature downtime, etc.)
0					Test run prior to survey; Disbaled Switch position 1 due to comm. problems with A/D no.1 (occasional bad, slow response, 1 in every 10 pings not returned), resulting in late incoming data, incomplete data files and missing serial string errors. !! **Update geometry** !!! **Inactive Channels:** **CH 65-72 show the same strange persistent noise as on the previous survey.** **Spiky CH: 18, 41,81**
1	30.06.2012	22:22 – 00:34	526 - 2103	600 - 2087	East; 4.0 kn; wind 3.5 m/s from SSE; 7 degC Deactivated also CH 18,41,81 at shot 694 Seismic signals from nearby vessel affect our data. Seapath navigation lost at 00:00:00 UTC resulting in that shot times might be wrong for several minutes until Seapath has been rebooted. Check geoeel logfile for shot numbers affected.
2	01.07.2012	00:58 – 2:58	2104 - 3544	2172 - 3535	West; 4.2 kn; wind 6.0 m/s from SSW; 8.1 degC Polar Duke started to shoot again at 01:33
3	01.07.2012	03:27 – 05:21	3545 - 4923	3567 - 4914	East; 4.3 kn; wind 3.5 m/s from SW; 8.2 degC Manual trigger at the beginning of line S/V Polar Duke's signal is now acceptable weak

8 Appendix

					Line-Offset is up to 15 m 04:10 Gun occasionally shows bad deltaT sometimes, but hydrophone looks fine - maybe due to miscalculation 04:15 Last six sections show increasing noise. 04:20 Continues constant line-offset of up to 20 m S till

4	01.07.2012	05:43 – 07:39	4924 - 6330	4946 - 6310	West; 4.5 kn; wind 3.3 m/s from SSW; 7.6 degC **Last six sections show increased noise**
5	01.07.2012	08:03 – 10:01	6331 - 7746	6345 - 7731	East; 4. kn; wind 3.3 m/s from SSW; 6.2 degC **Last six sections show increased noise** Recover P-Cable and try to fix the noise and leakage problems.
T	01.07.2012	17:45 -	7747 - 8236		Test run prior to line 6 Full 14 streamer array Disabled CH: 64
6	01.07.2012	18:33 – 20:42	8237 - 9785	8280 - 9767	West; 3.9 kn; wind 8.5 m/s from SSW; 8 degC Other seismic signals on the data
105	01.07.2012	21:09 – 22:10	9786 - 10512	9798 - 10510	Repeating part of line 5 East; 4.3 kn; wind 8.8 m/s from SW; 7.5 degC
104	01.07.2012	22:27 – 23:33	10513 - 11312	10535 – 11299	Repeating part of line 4 West; 4.1 kn, wind 8.0 m/s from SW; 7.6 degC
7	02.07.2012	00:38 – 02:46	11313 - 12842	11373 - 12813	East; 4.1 kn; wind 5 m/s from E; 7.1 degC Finishing Line w/o any Noise from Polar duke. After line's end heading further E w 3.5 kn to let Polar Duke armada pass. Recording the seismic noise during pass-by in project *monitor_PDuke*. ETA Line8_start at 6:15. 05:45 Channel 71 and 79 occasionally show low

					freq. noise
8	02.07.2012	06:11 – 08:14	12843 - 14313	12860 - 14295	West; 4.3 kn; wind 3.5 m/s from N; 7.3 degC Note: Polar Duke noise is weak **Deactivated ch 79 due to high noise** **06:20 - Deactivated ch 53** **Spiky Channels: 71, 80, 88** Serial String not detected: 12965,
12	02.07.2012	08:46 – 10:48	14314 – 15779	14332 - 15761	**Note: Shooting line 12 in opposite direction and in a different order so that we finish the inner lines before the bad weather sets in** East; 4.0 kn; wind 5.0 m/s from N; 7.2 degC At about 15290-15380 gun not firing, Gun occasionally shows bad deltaT **Spiky Channels: 71, 80, 88**
10	02.07.2012	11:19 – 13:16	15780 - 17187	15798 - 17171	West; 4.1 kn; wind 6.0 m/s from NE; 7.3 degC Gun occasionally shows bad deltaT **Spiky Channels: 71, 80, 88**
9	02.07.12	13:38 – 15:45	17188 - 18719	17241 - 18683	East; 4.4kn; wind 8.8m/s from NE; 7.1degC Gun occasionally shows firing delay around 1ms. Line No. not changed in Geoeel. Recorded in Line 10. **Spiky Channels: 71, 80, 88**
14	02.07.12	16:02 – 18:04	18720 - 20195	18787 - 20179	West; 4.6kn; wind 9m/s from NE; 7.4degC Gun occasionally shows firing delay around 1ms **Spiky Channels: 71, 80, 88**
11	02.07.2012	18:25 – 20:26	20196 - 21652	20235 - 21635	East; 4.0 kn; wind 12.9m/s from NE; 6.9 degC **Spiky Channels: 71, 80, 88** **Note: off line by over 70 m due to problem with GPS at ~5.8 km into line**
16	02.07.12 – 03.07.12	21:55 – 0:06	21653 - 23225	21724 - 23214	West; 4.3 kn; wind 11.4m/s from NE; 7.1degC **Note: beginning shots used to test gun** **Note: Large offset in beginning of path due to error with nav system**
S					Restarted after 36 h bad-weather lay-off. A/D can on first streamer not responding.

					Reconfigured without streamer 1: **GEOMETRY CHANGED!!** **Disabled CH: 42, 45** The coherent noise signals are back on all channels, though weak at this point. We go ahead and see how the noise develops. Weak signals on last channels of streamer 9 and 10.
13	04.07.12	12:05 – 14:12	23985 - 25505	24108 - 25471	East; 4.2 kn; wind 10.1m/s from NW; 6.1degC

18	04.07.12	14:32 – 16:32	25506 - 26949	25559 - 26943	West; 4.1 kn; wind 9 m/s from NW; 5.5 degC **16:07 Deactivated Channel 72 - low S/N** **Serial string not detected: 25558, 25903, 26047, 26394, 26453, 26599, 26615, 26807, 26809, 26841** **Note: Check file sizes, every not detected serial string goes along with several incomplete files**
15	04.07.12	16:54 – 18:54	26950 - 28439	26972 - 28420	East; 4.2 kn; wind 6 m/s from NNW; 6.2 degC **Serial string not detected: 26951, 26961, 27007, 27459, 27524, 27671, 27765, 27877, 27910+/-10 (many in a row), 27958, 28137, 28259-28262, 29366-28368, 28427-28429** **Note: Check file sizes, every not detected serial string goes along with several incomplete files**
20	04.07.12	19:18 – 21:13	28440 - 29891	28464 - 29880	West; 4.5 kn; wind 8.5 m/s from N; 6.1 degC **Serial string not detected: 28450, 28451, 28479, 28515, 28517, 28569, 28623, 28695, 28697, 28752, 28766, 28767, 28819, 28821, 28832, 28904, 28953-28968, 28991-29000, 29035, 29037, 29117-29120, 29138-29141, 29154, 29177, 29182, 29184, 29195, 29198, 29213, 29214, 29239-29242, 29255-29260, 29296, 29297, 29352, 29354, 29459, 29481, 29512, 29519, 29605, 29619, 29637, 29641-29670, 29731, 29735, 29737-29743, 29748, 29758, 29763, 29765, 297981-29786, 29788-29792, 29839, 29860, 29871** **Note: Check file sizes, every not detected serial**

					string goes along with several incomplete files **Note: Polar Duke started shooting at shot ~29100 and obscured our signal.**
			29892 - 29938		After line 20, the P-cable was recovered to check malfunctioning digitizers. Digitizers 1 had a bent pin that was fixed. Digitizer 3 that had slow responses and late incoming data was replaced. System working fine with 14 streamers now. **GEOMETRY CHANGED!!**
17	05.07.12	00:02 – 02:53	29939 - 31709	30048 –31704 Read note!	East; 4.5 kn; wind 4.0 m/s from SW; 5.9 degC **Deactivated Channels:** **Serial string not detected: 30079, 30128, 30152, 30205, 30207, 30221, 30232, 30237, 30287, 30294, 30320, 30353, 30396, 30403, 30405, 30412, 30436, 30438, 30440** **00:45 – system crashed due to the number of serial string errors, SPSU and Geoeel PC rebooted. We take a turn and go back on line where we lost it. Serial string errors are likely related to streamer 3, which we thus disable (switch 6033), and reconfigure.** **GEOMETRY CHANGED!! (no streamer on 3)** **Test shots: a30248 – 30463 –** **01:29 Back on track file no. 30704, 2.05 nm from the beginning of line 17** **Approx. Overlap:** - **part 1. 30048 – 30380** - **part 2. 30704 - 31704**
22	05.07.12	03:21 – 05:17	31710 -33099	31728 - 33067	West; 4.2 kn; wind 2 m/s from NW; 5.7 degC Missed three shots
19	05.07.12	05:38 – 07:43	33100 - 34610	33161 - 34586	East; 4.5 kn; wind 5.3 m/s from W; 5.8 degC
24	05.07.12	08:13 – 10:10	34611 - 36013	34638 - 35996	West; 4.5 kn; wind 6.5 m/s from WNW; 6.7 degC
21	05.07.12	10:40 – 12:45	36014 - 37506	36028 - 37467	East; 4.0 kn; wind 10.8 m/s from E; 6.6 degC

26	05.07.12		37507 -		West; xx kn; wind xx m/s from xx; xx degC Line-Offset is up to 30 m
23	05.07.12				East; xx kn; wind xx m/s from xx; xx degC
28					West; xx kn; wind xx m/s from xx; xx degC
25					East; xx kn; wind xx m/s from xx; xx degC
30					West; xx kn; wind xx m/s from xx; xx degC
27					East; xx kn; wind xx m/s from xx; xx degC

Ship's speed: 4 kn ± 0,3 kn
Gun system: mini-GI (15/15 in^3)
Shooting pressure: ~170-180 bar
Shooting interval: 4 sec
Recording window: 3 sec
Recording delay: 0 sec

Measured depth offset on deck after survey:

6011	6030	6033	6034	6025	6026	6012	6028	6013	6014	6031	6016	6017	6018
0,95	0,17	-0,34	-0,43	0,38	0,5	0,45	0,39	0,45	0,22	0,54	0,33	0,20	0,43